Proceedings of the ASPE

2023 Summer Topical Meeting

Precision Bearings and Spindles
University of North Carolina-Charlotte
Charlotte, North Carolina
Wednesday-Thursday, July 19-20, 2023

Byron R. Knapp, Professional Instruments Company
Eric R. Marsh, KLA
Don L. Martin, Martin-Mason LLC
Jimmie A. Miller, University of North Carolina-Charlotte

The American Society for Precision Engineering (ASPE) is a multidisciplinary professional and technical society concerned with research and development, design, manufacture and measurement of high accuracy components and systems. ASPE activities encompass relevant aspects of mechanical, electronic, optical and production engineering, physics, chemistry, and computer and materials science. Membership is open to anyone interested in any aspect of precision engineering.

Founded in 1986, ASPE provides focus for a diverse but important community. Other professional organizations have covered aspects of precision engineering, always as a sideline to their principal goals. ASPE is based on the core of generic concepts necessary to achieve precision in any application; independent of discipline, ASPE intends to be the focus for precision technology, and to represent all facets from research to application.

American Society for Precision Engineering
3434 Edwards Mill Road | Suite 112-325 | Raleigh, NC 27612 | 984-268-9756

Preface

This book comprises the proceedings of the ASPE Summer Topical Meeting entitled **Precision Bearings and Spindles**. The contributions reflect the authors' opinions and are published as presented to ASPE without change. Their inclusion in this publication does not necessarily constitute endorsement by the ASPE or its editorial staff.

Individual readers of this book and nonprofit libraries acting for them are permitted to make fair use of the material contained in this book to be used in teaching or research; provided they copy said paper in total, as written by the author. Permission is granted to quote excerpts from the scientific or technical works in this book with proper acknowledgment of the source to include: The author's name, the book name, and the ASPE tag line. Reproduction of figures and tables is likewise permitted from the contents of this book, provided that the same acknowledgment of the same source and content is permitted.

Any other type reproduction, systematic copying or multiple reproduction of any material in this book is expressly prohibited except with the written permission of the ASPE editorial staff, addressed to the Society's headquarters.

Volume 80

ISBN 978-1-887706-58-2

2023

American Society for Precision Engineering
3434 Edwards Mill Road, Suite 112-325
Raleigh, NC 27612

Printed in the United States of America

In Memory of

Henry Duangoupa Arneson

After being diagnosed with and treated for brain cancer at Mayo Clinic, Henry Duangoupa Arneson passed away at the age of 31 years old on Tuesday, July 11, 2023. He was a passionate engineer and a beloved husband, son, brother, and friend. As a young man, he began working with his father and two uncles at Professional Instruments Company before leaving to earn his Bachelor's degree in Mechanical Engineering at the University of Minnesota.

Henry continued his education at The Pennsylvania State University under Professor Eric Marsh, earning his Master of Science degree. As the Dr. John H. Bruning Fellow, Henry focused on "Force Characterization of Micro Grinding in Zirconia." He returned to work at Professional Instruments as an engineer where he excelled in innovative process development. Some of his conquests included 3D printing, laser engraving, optical inspection, complex programming of CNC machines, and attending technical and industrial conferences. Henry also explored numerous personal interests including playing competitive handball, meditation, coming up with clever puns, introducing you to the newest card game or board game, longboarding, and ice-climbing—but most of all was his passion for healthy food and spending time with friends and family.

Henry is survived by his loving wife Rigzin, his parents Dave and Srisuda, his sister Charlotte and his brother Christopher. His dog, Koda, will also miss him dearly.

Table of Contents

Preface.....i

In Memory.....ii

Contents.....iii

Meeting Sponsors.....iv

Sustaining Corporate Members..... v-vi

Corporate Members.....vii

Program Schedule & Technical Presentations.....viii-x

Technical Papers.....1-104

Author Index.....105

Meeting Sponsors

Gold Sponsor

Silver Sponsor

3M Company
279 Billerica Rd
Chelmsford, MA 01824
(978) 256-3911
3m.com

Aerotech, Inc.
101 Zeta Drive
Pittsburgh, PA 15238
412-963-7470
Aerotech.com

Alio Industries
5335 Xenon St
Arvada, CO 80002
303-339-7500
alioindustries.com

Ametek Precitech, Inc.
1100 Cassatt Road
Berwyn, PA 19312
610-647-2121
Ametek.com

ASM Pacific Technology Limited
900 Middlesex Turnpike, Building 6
Billerica, MA 01821-3929
978-338-2800
ASMPacific.com

Carl ZEISS Industrial Quality Solutions
6250 Sycamore Lane North
Osseo, Minnesota 55369
763-744-2473
Zeiss.com

Chardon Tool
115 Parker Court
Chardon, Ohio 44024
440- 286-6440
Chardontool.com

Cranfield Precision, Division of Fives Landis Ltd.
Woburn House, 3 Adams Close
Kempston, Bedford MK42 7JE
UNITED KINGDOM
44 1234 312 820
fivesgroup.com

Innolite
Liebigstraße 20
52070 Aachen, Germany
+49 241 4757080
innolite.de

Integrated Dynamics Engineering
68 Mazzeo Drive
Randolph, MA 02368, USA
781-326-5700
www.ideworld.com

Kern Precision, Inc.
1010 W Fullerton Ave, Unit E
Addison, IL 60101
331-979-0938
kern-microtechnik.com

Lawrence Berkeley National Laboratory
1 Cyclotron Road
MS: 46A-1123
Berkeley, CA 94720
510-486-4200
engineering.lbl.gov

Lion Precision
7166 4th Street North
Oakdale, MN 55128
651-484-6544
Lionprecision.com

MI-Partners
Habraken 1199
5507 TB Veldhoven, Netherlands
31-40-291-4920
Mi-Partners.nl

Micro-LAM, Inc.
5960 S. Sprinkle Rd,
Portage, MI 49002
269-288-4100
micro-lam.com

Moore Nanotechnology Systems, LLC
230 Old Homestead Highway
Swanzey, NH 03446
603-352-3030
Nanotechsys.com

New Way Air Bearings
50 McDonald Boulevard
Aston, PA 19014
610-494-6700
Newwayairbearings.com

OAV Air Bearings
1589 Reed Road
Pennington NJ 08534
609-454-5340
oavco.com

Optikos Corporation
107 Audubon Road
Building 3
Wakefield, MA
01880
617-354-7557
www.optikos.com

Physik Instrumente
16 Albert Street
Auburn, MA 01501
508-832-3456
PI-USA.us

Prior Scientific, Inc.
80 Reservoir Park Drive
Rockland, MA. 02370
781-878-8442
prior.com

Raytheon Technologies
870 Winter Street
Waltham, MA 02451
781-522-3000
rtx.com

Specialty Components
14 Village Lane
Wallingford CT 06492
203-284-9112
specialtycomponents.com

CORPORATE MEMBERS

ABTech
126 Route 12 North
Fitzwilliam, NH 03447
603-585-7106
abtechmfg.com

Corning, Inc.
Corning, NY 14831
607-974-3842
www.corning.com

Greenlight Optics
8940 Glendale-Milford Road
Loveland, Ohio 45140
513-247-9777
info@greenlightoptics.com

Heidenhain
333 East State Parkway
Schaumburg, IL 60173
847-490-1191
heidenhain.us

Hummingbird Scientific
Williamette Dr NE
Lacey, WA 98516
360-252-2737
hummingbirdscientific.com

K & Y Diamond
2645 Diab
Laurent, Quebec H4S 1E7, Canada
514-333-5606
www.kydiamond.ca

Meta Reality Labs
9845 Willows Rd. NE
Redmond, WA 98177
facebook.com

MPS USA, Inc.
50 Milk Street
Floor 16
Boston, MA 02109
857-207-9272
mpsag.com

Professional Instruments Co.
7800 Powell Road
Hopkins, MN 55343
952-933-3315
www.airbearings.com

SIOS Meßtechnik GmbH
Am Vogelherd 46
Ilmenau, Thüringen, 98693
Germany
49-3677-6447-30
contact@sios.de

Tru-Stone Technologies
P.O. Box 430
Waite Park, MN 56387
320-251-7171
www.tru-stone.com

UNC-Charlotte
Center for Precision
Metrology
9201 University City Blvd.
Charlotte, NC 28223-0001
704-687-8499
cpm.charlotte.edu

Zygo Corporation
Laurel Brook Road
Middlefield, CT 06455-0448
860-347-8506
Toll-free: (800) ZYGO-NOW
www.zygo.com

Program & Schedule

Wednesday, July 19, 2023

7:00 AM – Registration & Coffee
Grigg Lobby

8:00 AM – 12:00 Noon (Break half-way through tutorial)
Tutorial – Precision Metrology of Rotary Axes
Grigg 132

12:00 Noon – 1:30 PM
Boxed Lunch & Commercial Session
Grigg Lobby & Grigg 132

1:30 PM – 3:00 PM
Technical Session 1 – Precision Manufacturing Processes
Grigg 132

1. Designing, Building and Testing the Spindle for LODTM with Bob Donaldson
   Jeffrey W. Roblee (AMETEK – Precitech, Inc.).....1
2. Bearing Review of the Crystal Mitigation Stations
   Todd Noste (Lawrence Livermore National Laboratory).....3
3. Design and Construction of a Low-Cost Diamond Turning Lathe and Workholding System
   Cyrus M. Lloyd, Nicholas A. Browning (Auburn University).....8
4. Application of Statistical Methods for Optimization of Process Parameters in Ultra-Precision Hole Jig-Grinding
   Sinan J. Badrawy (Moore Nanotechnology Systems, LLC).....16

3:00 PM – 3:30 PM
Break
Grigg Lobby

3:30 PM – 5:15 PM
Technical Session 2 – Spindle and Angle Metrology
Grigg 132

1. ISO Standard on Geometric Accuracy of Axes of Rotation – An Update
   Alkan Donmez (National Institute of Standards and Technology).....23
2. Fully Automated Multi-Probe Spindle Error Analysis (SEA)
   Ralf Dupont (Levicron GmbH).....24
3. Development of a New High-Accuracy Angle Generator
   Christian F. Guertin (Vermont Photonics Technologies Corporation).....32

4. Super-Accurate Angular Encoder System with Multi-Detecting Heads Using VEDA Method
   Nobuyuki Ishii (Magnescale Co. Ltd.).....34
5. Comparison of an Encoder System and Autocollimator for Use in Si-Traceable Torque Measurements
   Zane Comden, John Draganov, Stephan Schlamminger, David Newell, Leon Chao (National Institute of Standards and Technology); Frank Seifert (University of Maryland).....39

5:15 PM – 6:45 PM
Reception, Lab Tours & Demonstrations
Duke Centennial Hall (next to the Grigg Building)

Dinner-on-your-own

Thursday, July 20, 2023

7:00 AM – Registration & Coffee
Grigg Lobby

8:15 AM – 9:45 AM
Technical Session 3 – Hydrostatic Bearings
Grigg 132

1. Bearing Design Choices Have Consequences: A Case Study
   Todd Noste, Laura E. Hopper, Jimmie A. Miller, **Christopher J. Evans** (University of North Carolina – Charlotte).....43
2. Potential Influence of Linear Hydrostatic Bearing Preload Method upon Carriage Averaging
   Mark A. Stocker (Cranfield Precision, Division of Fives Landis Ltd.).....49
3. External Pressurized Porous Gas Bearings for CO2 Turbomachinery
   Andrew D. Devitt, **Jeremy W. Rainey** (New Way Air Bearings).....51
4. Effect of Recess Area on the Performance of a Precision Hydrostatic Spindle with Mid-Thrust Bearing
   Chenggang Fang (Nanjing Tech University);
   Dehong Huo (Newcastle University).....52

9:30 AM – 10:00 AM
Break
Grigg Lobby

10:15 AM – 12:00 Noon

Technical Session 4 – Thermal and Vibration

Grigg 132

1. How to Control Temperature: It's Not That Hard
   Dan E. Luttrell (Kriterion, LLC).....58
2. Development and Evaluation of Device for Suppressing Spindle Head Vibration Caused by Bearing Cage
   Shotaro Tanaka, Ryoji Kondo,
   Hayato Koyama (Yasada Precision Tool KK).....63
3. Using X Axis Error to Balance a Part on a Spindle
   Lauren Micklow, Stephen J. Furst (Smart Material Solutions, Inc.).....67
4. Displacement Driven Balancing of a Machine Flycutter
   Stephen T. Hayes (Lawrence Livermore National Laboratory).....72

12:00 Noon – 1:30 PM

Boxed Lunch & Digital Presentations

Grigg Lobby & Grigg 132

1:30 PM – 3:30 PM

Technical Session 5 – Instruments and Applications

Grigg 132

1. Magnetic Preloaded Air Bearings for Precision Applications
   Andrew D. Devitt, **Jeremy W. Rainey** (New Way Air Bearings).....77
2. Revolutionizing Precision: Innovative Applications of Air Bearings in High-Performance Spindles
   Murat Erturk (OAV Air Bearings).....78
3. Levcube: A Six-Degree-of-Freedom Magnetically Levitated Nanopositioning Stage with Centimeter Range XYZ Motion
   Ian Heyman, **Lei Zhou** (The University of Texas at Austin).....84
4. A New Full-Field Imaging Projection Microscope for the APS Upgrade at 32-ID
   Alberto Mittone, Viktor V. Nikitin, Sunil Bean, Alex Deriy,
   Kamel Fezzaa, Janusz Matus, Curt A. Preissner, Deming Shu,
   Francesco DeCarlo (Argonne National Laboratory);
   Vincent De Andrade (KLA Corporation).....90
5. Development of the Transmission X-Ray Microscope for Sub-10 nm Resolution Imaging
   Viktor V. Nikitin, Alberto Mittone, Alex Deriy, Sunil Bean,
   Michael Wojcik, Kamel Fezza, Francesco De Carlo (Argonne National Laboratory); Vincent De Andrade (KLA Corporation).....95

Appendix

1. Machine Spindle Thermal Error Measurement Using a Photo Microsensor Array
   Vinu J. Pannackal, Thomas Furness, Simon Fletcher,
   Andrew P. Longstaff (University of Huddersfield).....100

Designing, Building and Testing the Spindle for LODTM with Bob Donaldson

Jeffrey W. Roblee (AMETEK – Precitech, Inc.)

Short Abstract

Many people consider the spind e to be the most critical component of the Large Optics Diamond Turning Machine (LODTM). This machine was designed and built during the period of 1979 to 1983 at LLNL under the direction of Bob Donaldson. He insisted that that the spindle have a vertical axis to minimize the action of gravity while machining 1.65 m diameter parts with weights up to 1400 Kg. This was the first time a vertical axis spindle would be used on a diamond turning machine, and it was a subject of much discussion at the time. This decision drove the machine to be effectively designed around a very custom spindle. Many concepts were considered to meet the unique design requirements of the spindle. As a member of the original design team, I want to share some of our experiences during the design, construction, and testing of this spindle.

To achieve the 25 nm rms accuracy requirement in the work zone of 1.65m x 0.5 m, thermal stability and low rotational error motions were essential. This drove the spindle rotor construction to be made of Super Invar. Zerodur was considered, but ultimately it was ruled out as impractical. Air bearings were also considered and tested for the axial bearing and different bearing geometries were studied. Both the bearings eventually ended up being oil bearings that used a light Velocite 3 oil to reduce heating from shear in the oil film. The design of these bearings drew significantly from Bob's PhD work at Columbia in the early 1960's. An overriding concern of ours was how to deal with the internal heat generation in the oil film. A wide range of cooling concepts were modeled before we selected one that proved to be very effective. The effects of gravity loading and centrifugal forces were also modeled and considered in the design of the rotor, and I will share Bob's comments on what he would do differently, if he had the chance to do it again. The mounting of the axial stator was also quite unique. It had three kinematic mounts with a controllable pressure chamber in between them to offset the loads on the hard points.

To meet the unique torque and speed requirements with minimal torque ripple, a custom motor was designed and built under the direction of the LODTM team. To minimize the heat and vibration from the motor, it was hard mounted to the floor of the "pit" below the machine. A special drive shaft and coupling were designed to apply a pure torque to the spindle while allowing the whole machine to float on pneumatic isolators. This drive shaft became part of the vibration isolation system for the whole machine.

With a diameter over one meter, the fabrication of the annular axial bearing, both rotor and stator, provided some unique challenges that required some very creative solutions. This was actually done twice because the initial axial bearing failed three times and required a total re-design and re-build. We knew that there was no way to achieve 25 nm error motions with a spindle this size. As a consequence, the error motions were measured in real time by means of

two pairs of custom-made capacitan e gages. Running in two grooves on opposite edges of the rotor, they measured axial and radial motions on both sides of the rotor. Of course, the grooves had their own errors that had to calibrated out. With the aid of metrology designed and operated by NIST (formerly NBS), the actual spindle errors were measured, using a method that has come to be known as the Donaldson Reversal Method on a master sphere. This allowed us to calibrate the errors in the cap gage grooves. Then we could use these measurements to correct for actual spindle errors in real time. This is what drove the need for a high-performance Fast Tool Servo. To our surprise, the FTS was ultimately not required to meet 25 nm rms accuracy requirements of the machine.

Bearing Review of the Crystal Mitigation Stations

Todd Noste
National Ignition Facility
Lawrence Livermore National Laboratory
Livermore, CA, USA

INTRODUCTION

The National Ignition Facility (NIF) at Lawrence Livermore National Laboratory (LLNL) uses potassium dihydrogen phosphate (KDP) crystals for frequency conversion of laser light. These crystals are used to reduce the wavelength of laser light from the fundamental wavelength (1ω) at 1053 nm generated by the neodymium doped amplifier glass to the second harmonic (2ω) at 527 nm and finally to the third harmonic (3ω) at 351 nm [1]. The NIF inertial confinement fusion (ICF) targets perform more efficiently when driven by the 351 nm light [1]. As the NIF looks to the future and seeks to increase the fluence on each beam line, eliminating the propagation of laser induced damage is increasingly important. The third harmonic generator (THG) crystals are particularly susceptible to laser damage due to their position in the laser system. Laser damage mitigation was developed for KDP crystal optics and glass optics.

CRYSTAL DAMAGE MITIGATION

Specialized diamond micro-milling machines (crystal mitigation stations, or CMSs) were developed at LLNL for crystal damage mitigation. A process was developed to machine a 1 mm diameter, 100 µm deep cone into the exit surface of the crystals using a single crystal diamond ball end mill with a 100 µm radius to remove laser damage [2, 3, 4, 5]. The cone stops damage propagation and disperses light passing through to areas of beamline that won't cause damage to the laser system. The CMSs and the mitigation process enable the NIF to operate at higher fluence and reduce the number of spot blockers that would be needed if damage mitigation was not possible [6]. This increases the amount of time a crystal optic can stay on NIF and reduces the need for re-finishing.

Crystal Mitigation Station

The mitigation stations use a collection of air bearing spindles, flexures, and porous graphite air bearings to position the crystal being mitigated and to machine the mitigation cone. The machine has three systems that work together to mitigate crystal damage. The first is a positioning stage to maneuver the crystal to find damage sites and fiducials, position the crystal over the diamond tool, and move the crystal to the load/unload position.

The second system has two cameras, one to image the damage sites and fiducials before moving the crystal over the diamond tool and one used to "touch off" the surface and monitor the mitigation process. The third system is the mitigation cartridge that machines the mitigation cone and evacuates chips. A crystal mitigation stations is shown in Figure 1.

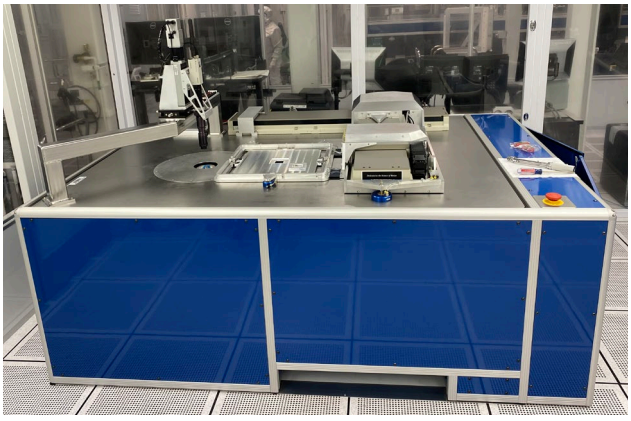

FIGURE 1. Crystal mitigation station at Lawrence Livermore National Laboratory.

The crystal mitigation stations are housed in a class 100 clean room as cleanliness is important to the success of the NIF. Material selection and part cleaning is a significant part of the design, manufacture, assembly and operation of optics processing equipment for the NIF. The KDP crystals are also sensitive to temperature and humidity. Crystal optics are stored under a nitrogen purge to protect them during storage.

MACHINE CHARACTERISTICS

The mitigation cartridge uses a cylindrical coordinate system shown in Figure 2. The R-axis positions the high-speed tool spindle in the radial direction, the C-axis rotates the tool about the Z-direction and the Z-axis moves the tool toward the crystal being mitigated.

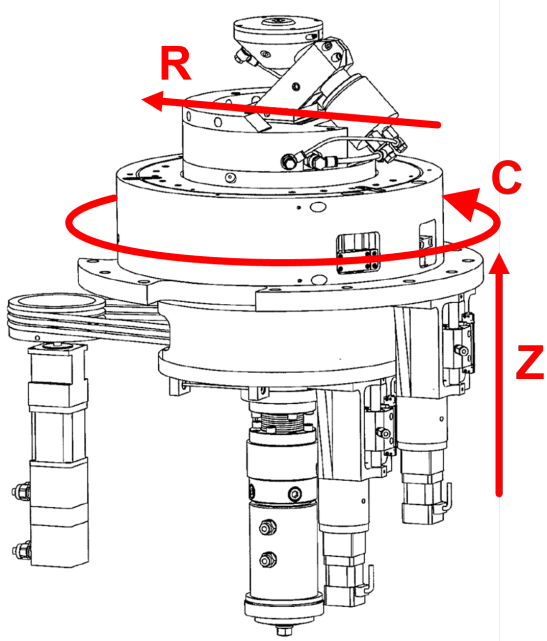

FIGURE 2. Coordinate system of the mitigation cartridge on the crystal mitigation stations.

The Z-axis and R-axis are actuated by nearly identical motor assemblies that use stepper motors, ball screws, limit switches and air bearings riding on a precision ground shaft. The motor assemblies connect to the moving stages with a flexure shaft allowing for lateral motion while staying rigid in the Z-direction to keep them from being over-constrained as the stages move up and down.

The crystal is supported by porous graphite air bearings that are designed for vacuum preload. Rather than using the vacuum preload, the machine switches between compressed air and vacuum in these bearings to provide a brake during machining. The brake can be activated using the control panel or with an M-code.

Air Bearing Spindles

The mitigation stations use air bearing spindles for supporting the mitigation cartridge, as a clever way to keep the motor assemblies separate from the rotating portion of the machine. The high-speed tool spindle also uses an air bearing spindle. Air bearing spindles offer a low friction, stiff, low maintenance and relatively simple interface.

High Speed Tool Spindle

The pneumatic air bearing and turbine on the tool spindle allow for rotational parts of the mitigation cartridge to be free from electrical connections and complicated interfaces. The compressed air supply for the tool spindle comes through the center of the mitigation cartridge and is fed through a rotary coupling with a bellows flexure that allows for the vertical motion of the Z-axis while maintaining rigidity in the C-axis rotation.

The tool spindle rotates at 80,000 RPM using the pneumatic turbine. The turbine is controlled using a solenoid that turns the spindle on/off and regulator that sets the air pressure supplied. The tool spindle uses an air bearing for smooth and nearly frictionless motion. The tool is held using a precision ER collet which keeps the tool centered.

Mitigation Cartridge Spindles

The mitigation cartridge is supported by two Professional Instruments (PI) air bearing spindles that allow for the C-axis rotation. The C-axis is driven by a pulley system and slotless brushless servomotor. The main air bearing spindle is a PI 10-inch (10R) while another 4-inch PI air bearing spindle (4R) is used to allow for the vertical motion that drives the pivot flexure in the R-axis while keeping the R-axis motor assembly stationary.

The R-axis motor assembly pushes on the stator of the 4R air bearing spindle which does not rotate with the C-axis. The rotor of the 4R air bearing is connected to the pivot flexure that actuates the R-axis and is supported by six rod flexures. The PI air bearing spindles are connected to a backup nitrogen supply to protect the bearings in case of a failure in the compressed air supply to the machines. The compressed air system also uses a system of regulators, filters, tanks and air dryers to provide damping in the system and to protect the air bearings from moisture and foreign debris. A dew point monitoring system measures the moisture in the compressed air before and after the air dryer to check the effectiveness of the dryer and to alert of failure in the system.

Flexure Bearings

The mitigation cartridge uses rod flexures (sometimes called spoke flexures) to support the two PI air bearing spindles while allowing motion in the R-axis and Z-axis stages. There are 13 rod flexures with 6 supporting each air bearing spindle and one used for stability. The rod flexures consist of the rod and two spools (one on each end) held into place with a set screw then brazed. See Figure 3.

FIGURE 3. One of the rod (spoke) flexures used to support the Z-axis and R-axis stages.

The rod flexure assembly is captured within the stages using set screws and friction. The rod flexures are in a triangular arrangement so that any parasitic motion in the flexures is in the rotational direction which isn't a sensitive direction for the system. Figure 4 shows the rod flexures (highlighted in green) for the R-axis.

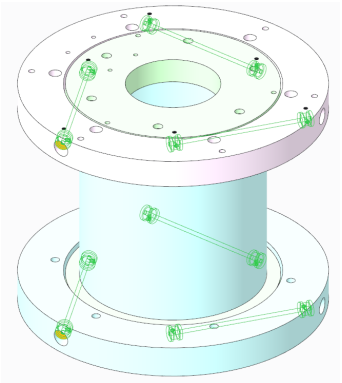

FIGURE 4. Showing the layout for the rod flexures that support the R-axis with the center spool moving relative to the outer flanges. The rod flexures are highlighted in green.

Six of the rod flexures are used for each of the axes to limit the degrees of freedom to the vertical direction while supporting the weight of stage. The travel of the stages are limited to the clearance of the rod in the slots for the rod flexures, for this application that is sufficient clearance.

The Z-axis and R-axis motor assemblies are off-center and use a series of blade and pivot flexures to drive the vertical motion from the center line of the PI air bearing spindles. The R-axis uses a double compound linear translation flexure, rod flexures and a pivot flexure for motion [5]. These flexures provide smooth, repeatable motion to achieve the translations of the R-axis and Z-axis [7]. The mitigation stations operate at relatively low feeds and speeds with exception of the high-speed tool spindle.

R-axis Pivot Flexure

A pivot flexure is used to transform the vertical motion of the R-axis motor assembly to the horizontal motion of the R-axis and high-speed tool spindle. The range of motion is ~2 mm. The ratio of vertical motion to horizontal motion is close to 1:1. The flexure arrangement is half of a cartwheel flexure. See Figure 5 for a diagram of how motion is achieved in the R-axis pivot flexure.

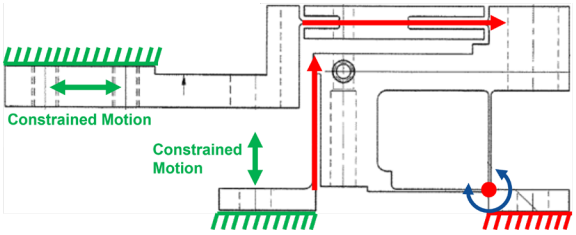

FIGURE 5. Pivot flexure for the R-axis.

The R-axis pivot flexure is attached (shown in red) to the Z-axis stage so that the Z-axis can move without affecting the R-axis motion. The vertical motion is actuated by the R-axis motor assembly and constrained by the rod flexures shown in Figure 4. The horizontal motion is constrained by the double compound linear flexure shown in Figure 6 and discussed below.

Double Compound Linear Flexure

The high-speed tool spindle is supported by a double compound linear flexure that allows motion of the spindle in the radial direction (R-axis). The flexure is limited to a travel of 2 mm by the control software and R-axis motor assembly limit switches. Figure 6 shows the axis of rotation and high-speed tool spindle stage motion.

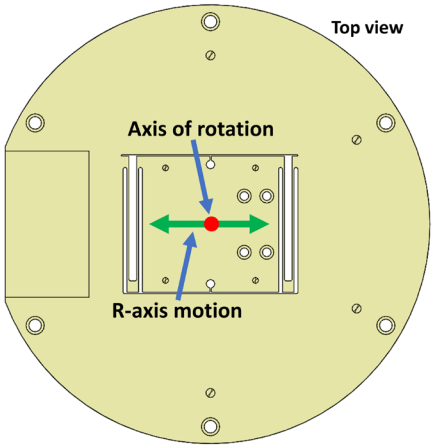

FIGURE 6. Double compound linear flexure that supports the high-speed tool spindle and allows for translation in the radial direction.

Motion of the R-axis and High-Speed Spindle

The double compound linear flexure and R-axis pivot flexure work together to move the high-speed tool spindle in the radial direction. When properly aligned, the diamond tool will rotate around the axis of rotation at R=0. The lateral alignment is set using a flexure-based post that supports the spindle. Shown in Figure 7 in gray.

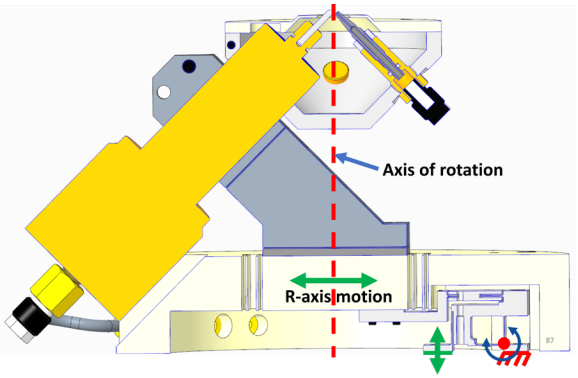

FIGURE 7. Motion in the radial direction using the pivot flexure and double compound linear flexure.

Alignment is checked with a reversal by 'touching off' on the surface of the crystal and rotating the C-axis 180-degrees and 'touching off' on the surface of the crystal a second time. With a proper alignment the two 'touch off' points will overlap. Touching off is the process of finding the surface with the diamond tool and machining a very small semi-sphere about 1-2 µm deep.

R-axis and Z-axis Flexures

A variety of additional flexures keep the system from being over constrained and are used in a pivot system to drive the Z-axis and R-axis assemblies from the center while the motor assemblies are mounted on the side. Figure 8 shows a pivot flexure used in the mitigation stations.

FIGURE 8. Free-flex cantilevered (single ended) pivot [8].

The cantilevered pivot flexures are compact and provide stable, smooth motion. They are used in the pivot assemblies for actuating the R-axis and Z-axis stages. They keep the system from being over constrained while allowing for the rotation (pivot) to lift and lower the stages. The Z-axis drive assembly is shown in Figure 9.

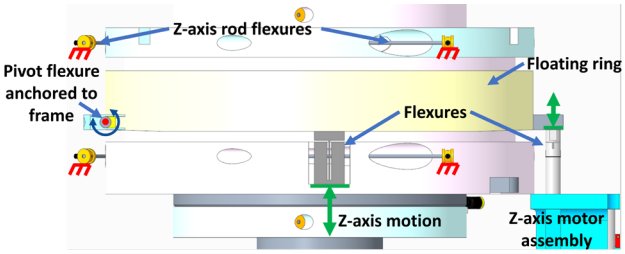

FIGURE 9. Flexure system for actuating the Z-axis stage.

Notice, the Z-axis stage is driven from the center while the motor assembly is on the right side and the pivot is on the left. This is achieved by using a floating ring around the stage that is attached using flexures. The rod flexures that support the Z-axis stage are also shown in Figure 9.

The R-axis uses a similar scheme but achieves motion with a series of flexures that support the 4R air bearing spindle. The R-axis also uses four of the cantilevered pivot flexures on the left-hand side of Figure 10.

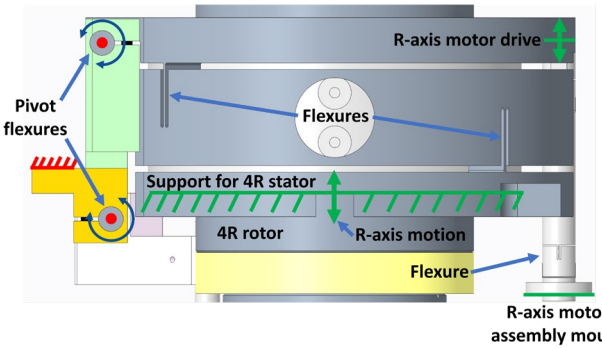

FIGURE 10. R-axis air bearing spindle mount that uses a flexure system with blade flexures and pivot flexures for actuating the R-axis stage.

The R-axis stage is driven through the center of the air bearing spindle to reduce any tilt induced by driving the stage off-center. The motor assembly is mounted to the flexure post shown on the right-hand side of Figure 10 and is attached to the R-axis air bearing spindle mount flexure assembly on the upper right. The pivot flexure assembly (left side of Figure 10) is attached to the Z-axis stage and to the R-axis air bearing spindle mount with clamps.

Bellows Flexure

The compressed air and nitrogen lines that run to the high-speed tool spindle and debris jet, respectively, pass through the rotary union (see Figure 11, shown in blue and gray) with the bottom portion that is stationary and the top portion that rotates about the C-axis.

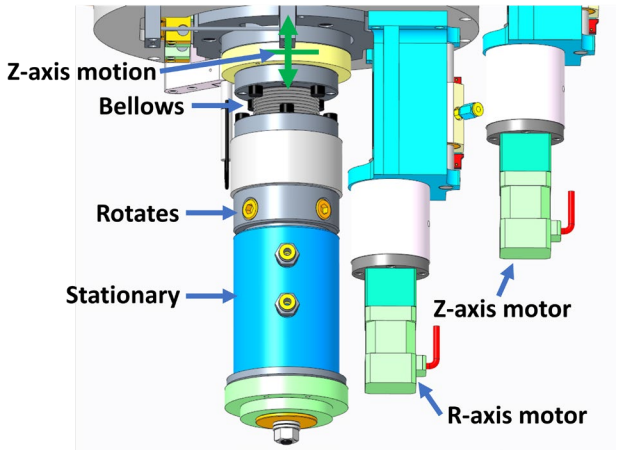

FIGURE 11. A bellows flexure is used to allow for vertical motion while staying rigid in the rotational direction about the C-axis.

A bellows flexure is used to allow for the vertical motion of the Z-axis stage while staying rigid in the rotation about the center of the air bearing spindles (C-axis). The rotary union and bellows work together to decouple the rotating part of the mitigation cartridge from the stationary part while supplying compressed air and nitrogen and allowing for the vertical movement of the Z-axis stage in a low friction, smooth manner.

CONCLUSIONS

The crystal mitigation stations use many of the precision engineering principles and dig deep into a precision engineer's toolbox to help fulfil the mission of the NIF. The use of air bearings and flexures in the design of the mitigation stations shows their effectiveness in achieving precise motion. Machines like the mitigation stations are vital to the success of the NIF and enable the scientific achievements we celebrate as a community.

ACKNOWLEDGMENTS

Paul Geraghty developed the crystal mitigation stations from conceptual designs through commissioning crystal damage mitigation on the NIF. Many thanks to Paul and the people that worked on the crystal mitigation stations, it has been a pleasure learning about them and stewarding them for the NIF.

REFERENCES

[2] L. Hrubesh, J. Adams, M. Feit, W. Sell, J. Stanley, E. Miller, S. Thompson, P. Whitman, R. Hackel, "Surface Damage Growth Mitigation on KDP/DKDP Optics Using Single-Crystal Diamond Micro-Machining", Laser-Induced Damage in Optical Materials, 2002, SPIE Vol. 5273, 273-279 (2004).

[3] P. Geraghty, W. Carr, V. Draggoo, R. Hackel, C. Mailhiot, and M. Norton, "Surface damage growth mitigation on KDP/DKDP optics using single-crystal diamond micro-machining ball end mill contouring", Proc. SPIE 6403, Laser-Induced Damage in Optical Materials: 2006, 64030Q (15 January 2007); https://doi.org/10.1117/12.696076

[4] J.S. Taylor, K. Carlisle, J.L. Klingmann, P. Geraghty, T.T. Saito, R.C. Montesanti. Precision Engineering within the National Ignition Campaign. Proceedings of the euspen International Conference, June 2010.

[5] P. Geraghty, R. Thigpen, "Surface Damage Growth Mitigation on KDP/DKDP Optics Using Single-Crystal Diamond Micro-Machining Ball End Mill Contouring", Proc. ASPE 27th Annual Meeting, 2012

[6] C.J. Stolz, S.R. Qiu, R.A. Negres, I.L. Bass, P.E. Miller, D.A. Cross, J.A. Davis, S. Sommer, C.C. Widmayer, B.J. MacGowan, P.K. Whitman, P.J. Wegner, "Transport mirror laser damage mitigation technologies on the National Ignition Facility," Proc. SPIE 10691, Advances in Optical Thin Films VI, 106910W (5 June 2018); https://doi.org/10.1117/12.2323284

[7] S.T. Smith, (2000). Flexures: Elements of Elastic Mechanisms (1st ed.). CRC Press. https://doi.org/10.1201/9781482282962

[8] Free-Flex Pivots – Cantilevered (single ended) flexures. https://www.flexpivots.com/cantilevered-single-ended-pivot-bearings/

DESIGN AND CONSTRUCTION OF A LOW-COST DIAMOND TURNING LATHE AND WORKHOLDING SYSTEM

Cyrus M. Lloyd[1], Nicholas A. Browning [1]
[1]Samuel Ginn College of Engineering
Auburn University
Auburn, AL, USA

INTRODUCTION

The state of the art in the field of ultraprecision manufacturing is represented by diamond turning machines. However, limitations in their affordability and work-holding methods limit productivity and accessibility. Common slow manual part mounting and alignment methods make high production difficult on such machines. The goal of this work was to develop a low-cost diamond turning lathe that includes a novel work-holding solution to address the two identified weaknesses. Goals include the ability to produce 6-inch diameter parts with sub-micrometer form accuracy and sub-10 nanometer R_a surface finish. The entire lathe was designed, machined, assembled, and tested in-house. At present, the best form and finish achieved is 1.5 µm and ~10 nm R_a, respectively. The finished machine, seen in Figure 1, could be manufactured for ~$75k and expands Auburn University's manufacturing capability with an increase in precision on the order of 10x.

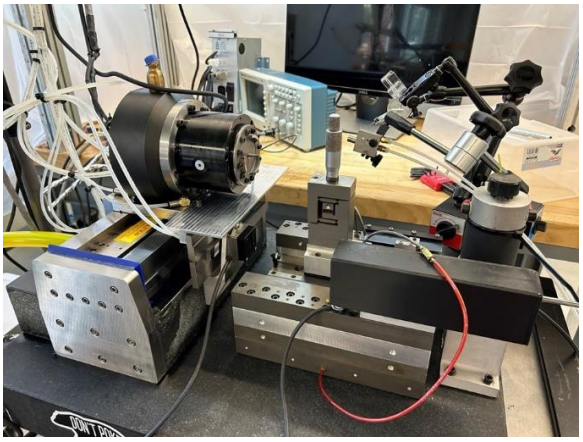

FIGURE 1. The finished machine ready for use.

While still cutting edge, diamond turning is a relatively well matured technology within the scope of precision engineering, with its origins going back some 60 to 70 years. Its unique deterministic cutting nature enables the production of optical components that could not be produced by other means, and thus it remains not just relevant, but of great importance. Despite their maturation, diamond turning machines remain an expensive technology that require a large amount of operator skill to set up and use. Here lies the motivations behind this project. Designing and building a research diamond turning machine (DTM) from scratch serves not only as an exercise in precision engineering, but also allows for purposeful design to keep costs low. Alongside this, a work holding system that requires minimal operator skill and is quick to use can also be designed to complement the machine. The resulting machine provides a bare bones, low cost, easy to use solution for small scale production or research use. The scope of this paper is to document the entire development of the machine, including its design, construction, and testing. The development of each of the subsystems is detailed, along with some notes on the machining of key elements and the testing of the machine done thus far.

DESIGN PHILOSOPHY AND CONCEPT

Just as Maudslay inquired, "what business has it to be there?" was asked throughout the initial design process [1]. An inspiration in such design is seen in Bryan's thesis on the same topic [2]. In order to be cost effective, the concept of a diamond turning machine was distilled down to its simplest critical components and the efforts focused only on making those as efficiently as possible. These elements were the two linear axes (X and Z), the spindle and workholding, and the feedback and controls. These make up the simplest form of DTM possible, a two-axis lathe that produces exclusively axis symmetric parts (not slow tool servo capable). The design of the machine was then carried out using principles of precision machine design laid out by Moore, Slocum, Smith, and others [1,3,4]. The machine uses a "T-base" design wherein the spindle rides on the X axis while the tool is held on the Z axis. Both axes are mounted on a granite surface plate which acts as a machine base, and the base sits on a pneumatically supported vibration isolation table. Another overarching consideration of such a design is its thermal characteristics. The general procedure followed was to firstly keep the amount of produced heat to a minimum, isolate any heat sources when possible, and finally design in a manner that makes things insensitive

to any heating that may occur [5]. Specific examples regarding thermal considerations will be mentioned in each of the sections where they are relevant.

DESIGN OF MACHINE ELEMENTS

Z Axis

Bearings and Layout

The Z axis was constructed from a surplus aerostatic stage built by Seagate but provided by Professional Instruments Company (PICo). It features a unique bearing arrangement, seen in Figure 2, and is constructed mainly of hard anodized aluminum while the bearing pads are an alumina ceramic. The air bearings themselves are orifice compensated with no grooves or pockets. This was later discovered to cause problematic oscillations, discussed in the "Positional Accuracy" section. No drive or feedback system was built into the stage, so these were engineered from scratch. The stage has a travel of approximately 4 inches.

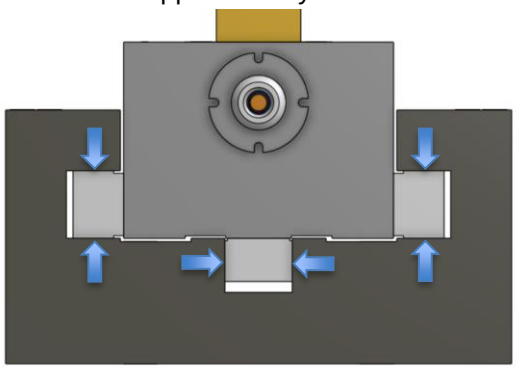

FIGURE 2. End view of the Z axis stage showing the air bearing arrangement. Arrows highlight the bearing faces.

Friction Drive Bar System

A non-influencing friction drive was developed for the Z axis. Friction, traction, or capstan drives have been proven to be highly precise on machines such as LLNL's DTM-3, LODTM, and others [6]. For this machine, the drive is based off of a piece of case-hardened linear shafting which is driven by pinching it between a female "V" drive roller and a flat idler roller, both of which are also hardened. The flat roller is on a flexure pivot and pinches the drive bar using a spring-loaded preload bolt. This configuration is seen in Figure 3. While this system can provide ultra-smooth, low hysteresis motion, there was a concern that it could couple error motion from the motor and rollers into the stage itself. If the drive bar were rigidly fixed to the stage, axial and radial error motion from the rollers would put moment loads on the stage causing it to pitch and yaw. The synchronous and asynchronous error motion profiles of the rollers' bearings would effectively be "unwrapped" onto the stages motion, negating one of the main benefits of air bearings.

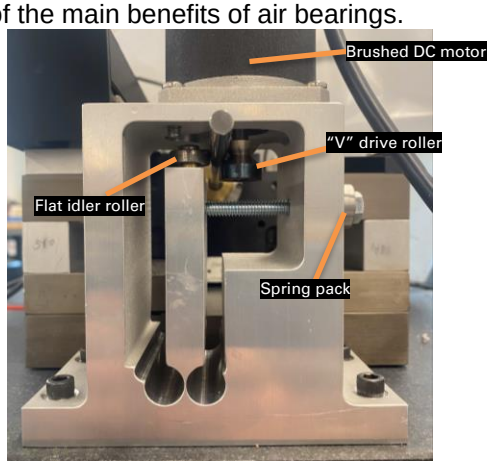

FIGURE 3. The V and flat pinch roller system.

To address this, the drive bar was interfaced with the stage using a "wobble pin" design, seen in Figure 4. A 3/16" silicon nitride ball bearing sits in between two hardened tool steel conical seats. The whole package is preloaded together by using a nut (shown in light gray) to compress an O-ring onto the stack up. This allows the bar to have a high compliance in the Θ_x and Θ_y directions while still being highly stiff in Z. There is little concern of the ball unseating when the bar is pulled on due to the preload present (~15 lbf). In order to unseat the ball, the bar would need to be pulled on with a force exceeding the preload force. Because of the low dynamics and low cutting forces the machine will experience, this force will not be produced in normal operation.

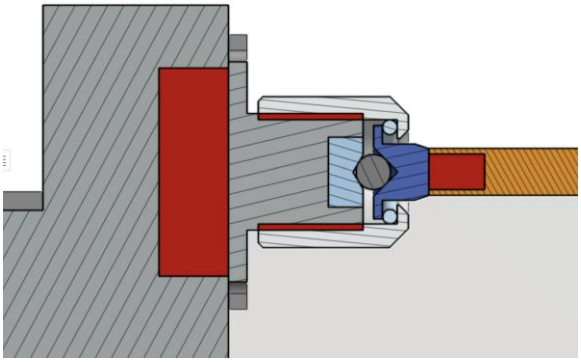

FIGURE 4. Wobble pin section view.

The friction drive also has distinct advantages with regards to thermal considerations. The only heat source, the motor, is on a separate structure,

mounted away from the stage. Because the only mechanical connection between the two is point contacts, the only reasonable way for the stage to experience heating during use is via radiation. A simple piece of insulation around the motor isolates it from the stage entirely, leaving it influenced only by the surrounding atmosphere.

Toolpost

The toolpost, shown in Figure 5, is a simple four-bar notch type flexure stage and a micrometer adjustment. The micrometer screw has a "floating" spindle that does not rotate while being adjusted. This was chosen so that the spindle could be rigidly fixed to the base of the toolpost and allow the micrometer to both push and pull to utilize the whole range of motion of the flexure stage (whereas a spherical tipped rotating screw can only push "up"). The challenge this introduced was now having to ensure the spindle and body of the micrometer remain perfectly co-axial, lest it bind up and cease to turn.

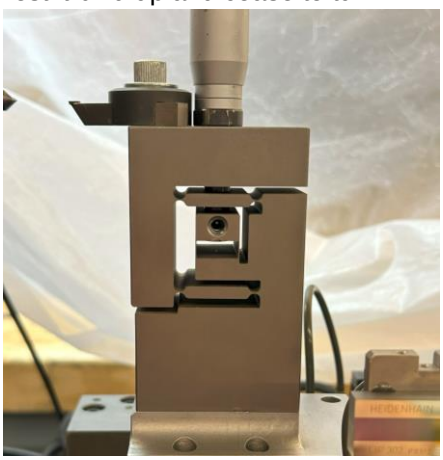

FIGURE 5. Flexure based toolpost.

The main flexure stage has a maximum travel of 0.05" in both directions. The parasitic error motion of the stage in Z can then be calculated and is found to be 0.0014", which would serve to try and shear the micrometer across its axis. To allow for this parasitic motion, the point where the micrometer spindle is fixed to the base was also made to be the moving stage of an even smaller four bar leaf flexure. The shearing force on the micrometer is now only the stiffness of that secondary stage times the parasitic error motion. Using equations from Slocum [3], the stiffness of each stage was calculated. The shearing force experienced by a .02" adjustment of tool height was found to be 0.18 lbf. The micrometer still spins freely under this load and the moment only serves to remove backlash.

X Axis

Bearings and Layout

The X axis for the machine was decided to utilize a custom hydrostatic box way design. Its bearing layout can be seen in Figure 6. This was chosen because of the symmetry of the design and ease of manufacturing. The guide way was made from 1018 mild steel, for ease of machining, cost, and because rust would not be a concern. The bearing plates that make up the carriage were made from 304 stainless steel, both for cost and since they would not necessarily always be coated in oil. The unfortunate consequence of this material mismatch is a differential thermal expansion that necessitates tighter environmental controls to keep the bearing gap constant.

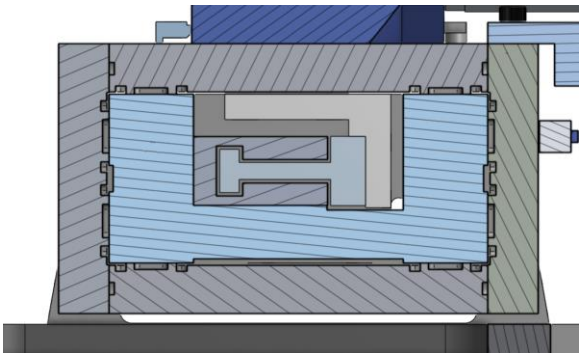

FIGURE 6. Section view of X axis showing bearing pads and linear motor.

Each of the four sides has four bearing pads in each corner for a total of 16. The stage is driven a Parker I-Force ironless slot type linear motor, mounted in the center of the U-shaped guide way, placed as close as possible to the center of the stage. The fact that the guide way was suspended like a gantry raised concerns about gravity sag of the axis, but FEA predicted a sag of no more than 6 microinches. The direction of sag, Y, is not a highly sensitive direction to begin with. Figure 7 shows a small 4 bar flexure built into the left side plate. This serves to accommodate small length mismatches in length between the granite base and the steel guide way. If both side plates were left solid, enormous forces would be produced by even a tiny difference in length between the steel and granite, be it from manufacturing or a change in temperature, and the guide way would likely bow. Unlike the Z axis, some warming of the X axis in operation is inevitable without removal of the linear motor from inside of it and significant investment in cooling the hydraulic system. Its symmetry ensures no geometric distortions

besides a uniform expansion should occur when warmed. Thus, the philosophy of use for this axis is simply to let it warm up until it achieves an equilibrium and stops growing. Testing showed a plateau after around 45 minutes.

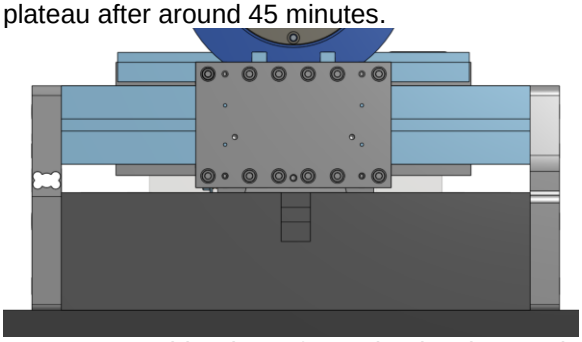

FIGURE 7. Side view of X axis showing strain relief flexure in side plate

Design of the Hydrostatic Bearing System

The design of the hydrostatic bearings themselves was carried out according to procedures laid out by Rowe [7]. With an idea of the geometry and size constraints of the axis, a first guess was made at the size of the pads. On the advice of Rowe, a supply pressure of 300 PSI, a fly height of 0.001”, and a β, or pressure drop across the restrictor, of 50% was selected. Orifice compensation was also chosen due to cost and manufacturing reasons. A MATLAB® code was created to take the pad geometry, supply pressure, β, and oil properties as an input, and output all properties of the resulting 16 pad box way arrangement, including the required orifice diameter. This allowed for rapid feedback on bearing performance as the pad geometry was iterated to fit within the preexisting constraints.

In future work, active compensation, such as a constant flow diaphragm valve, may be implemented due to orifices sensitivity to contaminates and manufacturing tolerances. This could also yield stiffnesses up to 4 times as high as passively compensated systems with the same geometry [8].

Spindle

Work Spindle and Mount

The work spindle is a 4-inch diameter, opposed cone (“biconic”) air bearing spindle, generously provided by PICo. It is of a hard anodized aluminum construction and boasts sub-microinch error motion in all directions. The spindle did not have any motorization or feedback elements so these were integrated in using spare parts from other scrapped products. Motorization was accomplished with a frameless permanent magnet AC motor, the magnet rotor of which was affixed to the spindle via a custom shaft. The stator then bolts on the back of the spindle mounting flange and a Heidenhain 1024-line count incremental encoder mounts on the outside of that. The housing that the flange bolts to is affixed to the X axis with dovetail clamps that allow adjustment of the spindle alignment by pushing on either side of the spindle axis. The entire spindle assembly can be seen in Figure 8. Spindles are often the largest source of heat in a machine tool, but the combination of a relatively small bearing and an efficient synchronous motor yields a favorable thermal situation. When idling at 2000 RPM, the spindle draws only 0.9 watts. Cutting force calculations estimate a sample finishing cut in brass to only draw another 0.3 watts (75mm diameter, 2 µm depth of cut (DOC), 2 µm feed per rev (FPR)).

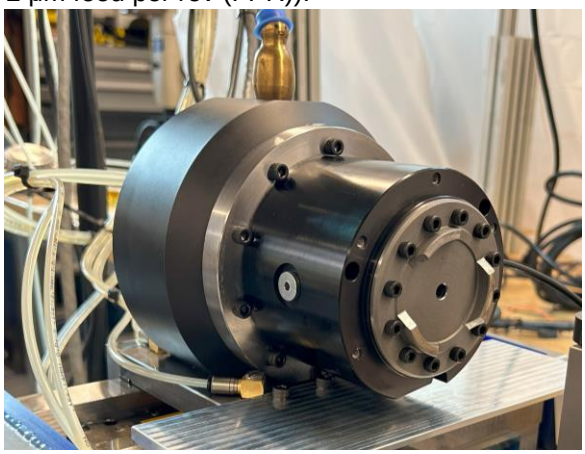

FIGURE 8. Complete mounted spindle assembly.

Workholding System

The goal of the workholding system was to create a standard zero-point pallet system similar to an Erowa™ chuck, that would allow rapid transfer of parts on and off of and between machines with exceptional repeatability. This would allow parts to be transferred from a roughing machine to the DTM with zero need for time hungry manual alignment. Similarly, such a system tightly closes the metrology loop, allowing parts to be quickly taken off, inspected, and then remounted and further corrected without losing alignment. The design took inspiration from Hale’s patent on three toothed kinematic couplings but was modified to better fit the application [9]. Hale’s concept had one half of the coupling using flat contact faces and the other half using rounded ones, yielding line contact when they are mated. The design used for this application used two identical halves with flat faces, trading some kinematic ideality for stiffness. The teeth were

also made thinner to aid in elastic averaging. One half of the coupling is seen in Figure 9. In practice, this half mounts to the spindle nose and the other can either serve as a chuck or fixture to mount the part to, or the coupling geometry can easily be machined directly into the part itself. A draw bar going through the spindle threads into the removable part, firmly mating the two halves together.

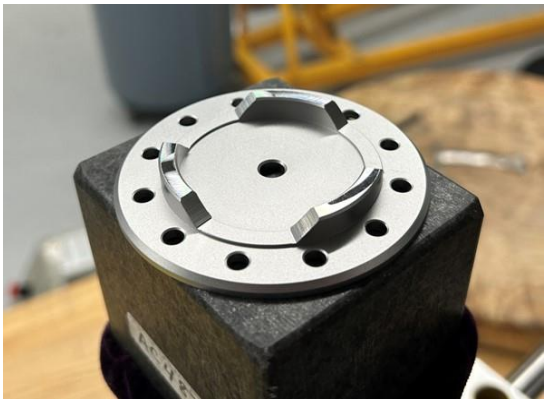

FIGURE 9. Quasi-kinematic coupling used as a standard workholding system across machines.

Feedback, Controls, and Electronics

Positional Feedback

Both axes use Heidenhain LIP-382 linear encoders for position feedback. The scales are made on a Zerodur™ substrate and have a signal pitch of 128 nm. This analog quadrature signal is interpolated by the servo drives to give a position resolution of 2 nm. This could be interpolated further, but 2 nm was selected to keep signal frequencies manageable for the rest of the hardware. Due to design constraints, the readheads are fixed to the machine base and the scales move with the axes. This layout causes a "dynamic" Abbe offset that changes throughout the travel of the axes and is non-ideal for linear performance. This will be addressed in future work.

Servo Drives and Control Software

The servo drives selected for this machine were Granite Devices IONI-PRO's; chosen for cost, versatility, and capability. They can drive any kind of motor, have 3 modes with independent control loops based on the application, and accept a wide range of control inputs. The brushed DC motor and ironless linear motor for the Z and X axes run off a 6-gain parameter position control loop, while the synchronous brushless spindle motor runs on a velocity control loop for ultra-consistent speeds and no cogging.

The control software is still in development but will likely run on a LinuxCNC based system. This will be responsible for providing a step/direction pulse train to the drives. The control loop computation is then handled by the drives rather than the control. There is also another software under our development that utilizes the drives' SimpleMotion communication protocol. This communicates with all the drives via an addressed bus system, very similar to EtherCAT. This allows for a shared master clock and more advanced command modes enabling a higher degree of synchronization.

SELECTED NOTES ON FABRICATION

As previously mentioned, the DTM was developed completely in-house, including the machining of all of the necessary components. Some elements presented unique challenges in precision machining and the techniques used and lessons learned will be briefly discussed below.

Precision Grinding of the X axis Guideway

The grinding of the X axis guideway was critical to the performance of the hydrostatic bearings and the maximum attainable part accuracy. It was made from mild steel and is 12 inches long. Across this entire length it was ground flat, parallel, and square to within 1 µm. In order to achieve this, the Harig 618 Automatic surface grinder used was allowed to warm up for a minimum of 6 hours before finish grinding. It is the belief of the authors, influenced by the work of PICo, that traditional surface grinding to this level could not have been accomplished with magnetic workholding. The workholding for finish grinding consisted of setting the meticulously cleaned and stoned part onto a freshly ground and stoned magnetic chuck, but not turning the magnet on. Three drops of Loctite 382 toughened instant adhesive were deposited around the part and allowed to wick around (but not under) the part and create a small fillet. This method of securing the part imparts zero influence on the material but extreme caution and light cuts must be taken. Using this method, almost all remaining error in the part geometry is a result of the straightness of the ways of the grinder themselves.

Machining of Granite Frame Elements

Developing a process of machining granite to a high accuracy on our Haas CNC machining center was necessary because the granite machine components would not fit on the Harig surface grinder. Most important was the flatness and parallelism of the X axis mounting faces, as well as their squareness to the lapped bottom face. This was accomplished by using a very small diamond core drill as a facing tool with

<10% diameter stepovers. This serves to copy the machine's XY plane directly on to the part for the flattest possible surface, whereas using a large tool with big stepovers introduces errors from spindle alignment. Similar to the grinder, the machine was allowed to warm up for several hours doing air-cutting passes before the actual finish passes. Squareness was dialed in by adjustment of the vise torque, which would tilt the part due to the vise body deformation.

Rotary Spin Grinding of Spindle Mounting Components

The mounting surfaces that the spindle mates with have critical flatness requirements. If the spindle is bolted to a surface which is not flat, it can distort the spindle housing, inducing error motion and decreasing performance of the spindle. Therefore, the spindle mounting flange was rotary surface ground, or "roto-ground," using an air bearing spindle on the surface grinder, the setup of which is shown in Figure 10. This method of grinding is able to yield parts much flatter than traditional surface grinding since it eliminates one of the linear axes of motion and replaces it with a far more accurate rotary one. Using this method, the spindle flange was ground flat and parallel to better than 0.5 µm.

FIGURE 10. Precision rotary surface grinding with an air bearing spindle.

TESTING AND RESULTS

Positional Accuracy

The true positional accuracy of the machine was not able to be completely characterized due to insufficient metrology capabilities of our lab. The Heidenhain Zerodur™ scales are by far the most accurate and traceable length standard at the entire university so all tests performed with mechanical and electronic indicators ended up revealing calibration errors in the measurement equipment, not the axis. Even when using a laser interferometer, the total uncertainty from atmospheric variability and laser wavelength stability is higher than that of the stages. Metrology routines and equipment for other parameters such as straightness of travel are under development. Repeatability of both axes experienced a similar issue of metrology limitations, wherein no equipment our lab possesses is precise enough to detect any error. The positional stability of the axes was measured by recording following error in the drive tuning software. The X axis following error was stable at +/- 1 encoder count, or 2 nm. The Z axis performed far worse, with a positional noise floor of around 30 nm. Investigation found the air bearings were causing the stage to oscillate in the Θ_y direction, which was showing up as a Z error because of the Abbe offset of the encoder. The open loop positional jitter this caused is shown in Figure 11. The current tune on the servo control loop is not excited to instability by this oscillation, but does not have enough bandwidth to cancel it out. Frequency analysis showed that the predominate frequency of the jitter was around 90 Hz. Further investigation included monitoring this oscillation across supply pressures from 0-90 PSI. Curiously, the oscillation appeared the moment the bearings had enough pressure to lift off, and the frequency spectrum remained nearly constant regardless of the pressure. The only thing that changed with pressure was the amplitude of oscillation, varying nearly linearly.

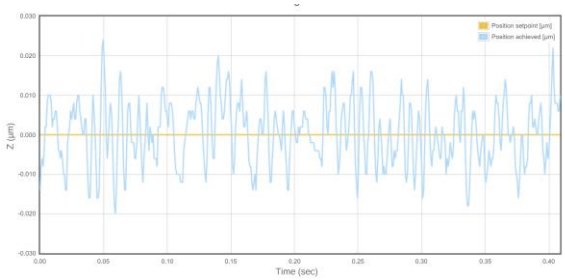

FIGURE 11. Open loop positional jitter of Z axis.

Workholding System

A series of tests was performed to determine the repeatability of the workholding coupling in the radial, axial, and tilt directions. It should be noted that these tests were performed without precise torque control of the drawbar, proving the system's insensitivity to such potential operator variables. 10 cycles of the coupling were performed for each test. The total average deviation from zero is the average reading on the gage across all cycles, having been set to zero

before the first cycle. The mount-to-mount repeatability was defined as the average change from one cycle to the next. This helps remove any thermal or mechanical drift that may affect the total average deviation result. The lack of data for tilt mount-to-mount repeat was due to only having one gage available for testing. In order to subtract out axial repeat from tilt repeat every cycle, one gage must be placed at spindle center and one at a radius. Because only one was available, it was placed at a radius and then the average axial repeat was subtracted from the resulting average combined axial+tilt. This gives a rough estimate of average tilt repeatability over the course of the runs but not a mount-to-mount estimate.

TABLE 1. Repeatability testing results of workholding system.

Sensitive direction	Average total deviation from zero	Average mount-to-mount repeatability
Tilt	7 µrad (1.45 arcseconds)	---
Radial	423 nm (16.7 µ")	345 nm (13.6 µ")
Axial	523 nm (20.6 µ")	142 nm (5.6 µ")

Test Cuts

Test cuts were taken in aluminum, copper and brass to test machine performance. Because of the current control limitations, only planar mirrors were produced via simple facing cuts. Speeds and feeds were developed experimentally. The aluminum parts discussed below were cut at 500 RPM, 2 µm DOC, and 2 µm FPR. This proved to be too slow of a feed and rubbing was experienced. The copper part was finished at 6 µm FPR.

Form Results

The form of the test parts produced were inspected with electronic indicators on a surface plate and with a laser Fizeau interferometer setup using an optical flat. The geometry was shown to be of inferior quality due to spindle alignment issues and was conically concave by about 1.5 µm per 75 mm of diameter. Recently obtained metrology equipment will make the removal of this error trivial and the target is a flatness of better than 0.1 µm on a part of that size.

Finish Results

The surface finish on the aluminum and copper parts obtained was inspected first with close contact atomic force microscopy (AFM). The maximum sampling length on the Pacific Nanotechnology AFM used is 70 µm; not long enough to make accurate global surface finish claims but useful for analysis of higher spatial frequency roughness and tool cutting behavior. This is well shown in Figure 12.

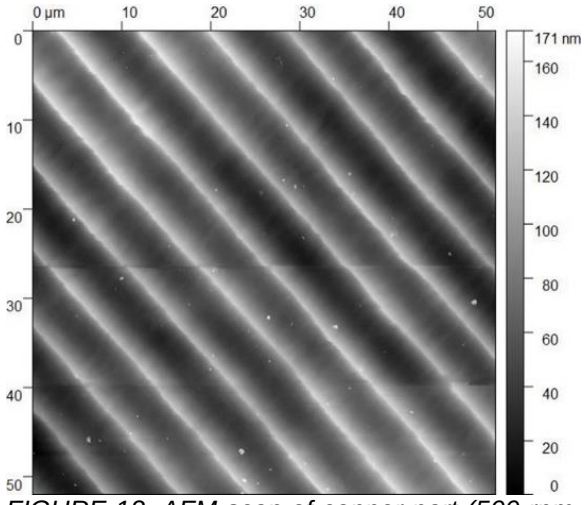

FIGURE 12. AFM scan of copper part (500 rpm, 6 µm FPR).

Inspecting a line profile across the AFM scan of the aluminum part gave an R_a of 14 nm. For a more accurate surface roughness measurement, a KLA Profilm3D® white light interferometer was used to measure over a larger sampling length. The measured results from this machine were an R_a of 8 nm (80 µm cutoff) and a S_a of 18 nm. Reasons for these finish results are suspected to be related to the Z axis jitter.

Cost

Because of kind donations and bespoke components, the total cost that was experienced by our lab is not necessarily representative of what it would cost to produce one of these machines from scratch. The cost experienced by our lab and its members was in the ballpark of $10,000. The practical cost of the machine was estimated by comparison to commercial components, considering raw material and manufacturing costs, and estimating man hours of work necessary. It was concluded that this machine could be manufactured for approximately $75,000. Despite it being a bare bones machine, this price point could be extremely competitive for certain applications.

FURTHER WORK AND CONCLUSIONS

While this paper documents most of the creation of the low-cost DTM, it is by no means a final report on the project. Significant efforts in controls, cutting processes, and machine characterization are still ongoing. Most important is the development of a robust control system that

allows for error compensation in software. This will allow any lingering geometric errors to be effectively removed. Secondly, a renovation of the hydraulic system is necessary to manage heat more efficiently and remove pressure pulsations. The current pump runs at a high speed and generates far too much heat for passive radiation from the hoses to dissipate. An intercooler in line with a larger, slower gear pump will greatly reduce the amount of heat put into the X axis. Finally, as mentioned before, an upgrade of the hydrostatic bearings to an active compensation arrangement will greatly improve stiffness and overall axis performance. In summary, a minimum viable prototype of a low-cost diamond turning lathe was developed and tested but still has room for improvement. The novel workholding system also performed well and makes setups more efficient.

ACKNOWLEDGEMENTS

In lieu of a list of names spanning several pages, the general demographics from which they originate are named. The utmost thanks are extended to:

Professional Instruments Company, for providing spindles, support, internships, and a plethora of wisdom.

Edge Technologies, for providing the diamond tools without which the lathe could never have been tested.

The ASPE and its members, for their truly humbling welcoming, support and willingness to help.

The thriving community of machinists on Instagram and Youtube, whose sum centuries of experience and knowledge guided our education and introduced us to the field.

A portion of this work was performed under the auspices of Auburn University's Undergraduate Research Fellowship program. Their financial support is also duly appreciated.

REFERENCES

[1] Moore WR. Foundations of Mechanical Accuracy. The Moore Special Tool Company; 1970.

[2] Bryan WJ. Construction of a Diamond Turning Machine. Thesis. 1978

[3] Slocum AH. Precision Machine Design. Prentice Hall; 1992.

[4] Smith ST, Chetwynd DG. Foundations of Ultraprecision Mechanism Design. Gordon and Breach Science Publishers; 1992.

[5] Hale LC. Principles and Techniques for Designing Precision Machines. Thesis. 1999

[6] Donaldson RR, Maddux AS, Shaw MC. Design of a high-performance slide and drive system for a small precision machining research lathe. CIRP Annals 1984;33:243–8.

[7] Rowe WB. Hydrostatic and Hybrid Bearing Design. Butterworth & Co; 1983.

[8] PM Controller for Guides. Hyprostatik 2023. https://hyprostatik.de/products-service/pm-controller-for-guides.

[9] Hale LC. Three tooth kinematic coupling, 2000.

APPLICATION OF STATISTICAL METHODS FOR OPTIMIZATION OF PROCESS PARAMETERS IN ULTRA-PRECISION HOLE JIG-GRINDING

Sinan Badrawy
Moore Nanotechnology Systems, LLC
Swanzey, New Hampshire, USA

INTRODUCTION

The growth of visual applications in our daily lives dictates the need for higher image resolutions. While the megapixel of a camera sensor is crucial for its resolution, the quality of the lens assembly in front of the sensor is as important to the final resolution of the image. The majority of these lenses that are implemented in smartphones, automobiles and other cameras are made of injection molded plastic. These lenses require injection mold tooling with high accuracy and consist of front and rear mold pins for forming the lens shape and mold plates. The mold plates insure the alignment between the mold pins to each other. Typical required hole accuracy of such a mold plate is in the order of < 0.5 µm in roundness and cylindrical deviation. Further, aspect ratios of the holes are about 1:5 with major diameters between Ø8 to Ø 10 mm. A typical size and tolerance of such mold plates is shown in FIGURE 1.

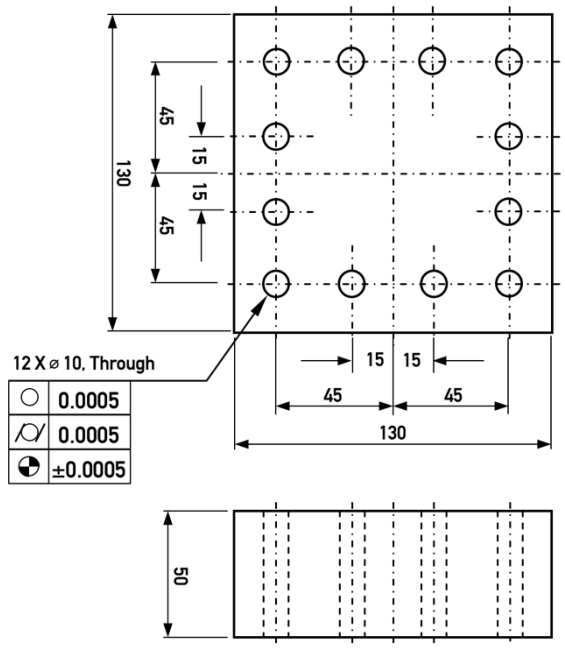

FIGURE 1: Example for dimensions and tolerances of an optical mold plate

In general, the injection mold plates are made of hardened tool steel. In conjunction with the required accuracies, ultra-precision jig-grinding is the predominant applied process for fabricating these holes. The accuracy of these holes is not only influenced by the motion accuracy of the machine tool axes, but also greatly impacted by the process, dressing conditions, and the applied grinding strategy. Determining the optimized parameter configurations for achieving roundness and cylindrical deviation under 0.5 µm, extensive testing is needed to analyze the effects of the parameters on part accuracy. To minimize the overall experimental effort, a Taguchi analysis was carried out based on a L18 orthogonal array.

A series of experimental grind tests, defined by five investigated parameters were performed on a Moore Nanotechnology Systems ultra-precision jig-grinding machine. Overall, 12 grinding trials for each experiment were conducted. The optimum level and the relative effects of various factors were predicted by applying a signal-to-noise ratio analysis. Final conclusions were drawn from this analysis to understand how the different parameters affected the mean and variance of the hole roundness and cylindrical deviation. To verify the optimum predicted parameter settings a final validation experiment was conducted.

TAGUCHI METHOD DESIGN OF EXPERIMENTS

The first step in Taguchi's Method, Design of Experiments (DOE), is to define the process objective, or more specifically, to identify the target criteria for which the performance of the process will be measured [1, 2, 3]. In this study the objective was to minimize the deviation of the ground holes from a cylindrical form. In accordance with ISO 12180-1 [4] (FIGURE 2), the deviation from the cylindrical form can be classified into these components:

- Median line deviation or curvature, which is defined by the center of circular cross sections with constant radii and its deviation from a nominal straight axis.

- Radial deviation or Radii PV which is the deviation in a normal cylindrical workpiece having all cross-sections circular and concentric to a straight axis, but whose diameters vary along the axis. Typical deviations can be conical, barrel or hour-glass shapes.
- Cross-section deviations are cross-sections of the same size and form, but are not round. In other words, it is the deviation from a roundness of the cross-sections.

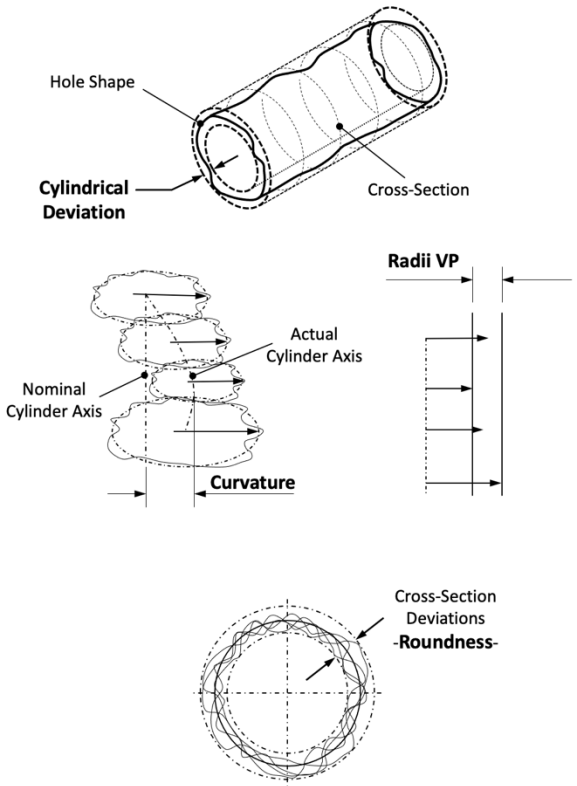

FIGURE 2: Deviation from the cylindrical form and its classifying components

The above highlighted deviations from a cylindrical form are the output parameters of the analyzed processes. Hence, to achieve hole cylindricity < 0.5 µm, the objective was to obtain a small value not only for the cylindrical deviation, but also for the cross sectional roundness, radii PV, and curvature.

After defining the measurable target criteria for evaluating the process performance, the next step was to determine the parameters affecting the process [5]. In the case of jig-grinding holes, typical sources that influence the deviation from a cylinder can result from the *i.) machine*: machine axis geometrical and positional accuracy, axis reversal errors, dynamic and static stiffness, vibrations, etc.; from the *ii.) workpiece*: material conditions, hole aspect ratio, hole wall integrity, workpiece holding etc.; from the *iii.) tooling*: grinding wheel material, tool clamping, grinding wheel aspect ratio, dressing method and parameters, tool wear etc.; and from the *iv.) process*: grinding speed, feedrate, radial and axial depth of cut, reciprocating stroke length, number of spark-outs, etc.

The selection of investigated parameters and the tested variable magnitude is based on the in-depth understanding and the legacy knowledge of the jig-grinding process. To minimize the noise ratio on the experiments, certain parameters were tightly controlled. For example, temperature of the cutting fluid as well as the machine environment during the cutting test was controlled to 20 °C ± 0.02 °C. To avoid any distortions of the test part while holding it on the machine table, a precision workpiece clamping mechanism was implemented. In addition to the clamping function, this mechanism also insured the position repeatability of the test part relative to the machine coordinate system.

The investigated parameters were:

P1- *Axial Depth of Cut (ADOC)*: the jig-grinding method applied is referred to as planetary grinding, in which the grinding wheel is moving in a simultaneous circular and axial oscillating motion (reciprocation motion) (FIGURE 3). Therefore, ADOC is determined by the ratio between the circular and the axial oscillating motion.

P2- *Wheel Protrusion*: is the wheel height which protrudes above and/or below the workpiece surface during the reversal direction of the reciprocation motion (FIGURE 3).

P3- *Number of Spark-Out*: Is the amount of reciprocation strokes that are exercised without increasing the radial depth of cut.

P4- *Grinding Wheel Speed*.

P5- *Radial Depth of Cut during Dressing*: Is the radial advancement of the grinding wheel during a dressing stroke (FIGURE 4).

The investigated parameters and their levels are presented in TABLE 1.

The Taguchi method reduced the variation in a process through a robust DOE. This method investigated how different parameters affect the mean and variance of the process performance characteristics, which defines how well the process is functioning. This involves using an Orthogonal Array to organize the investigated

parameters affecting the process and the levels at which they are varied. Unlike a factorial DOE that tests all the possible parameter combinations and their variance, Taguchi's method only tests pairs of combinations. This allows acquiring the necessary data to determine which parameters have the greatest effect on the process with a minimum amount of testing.

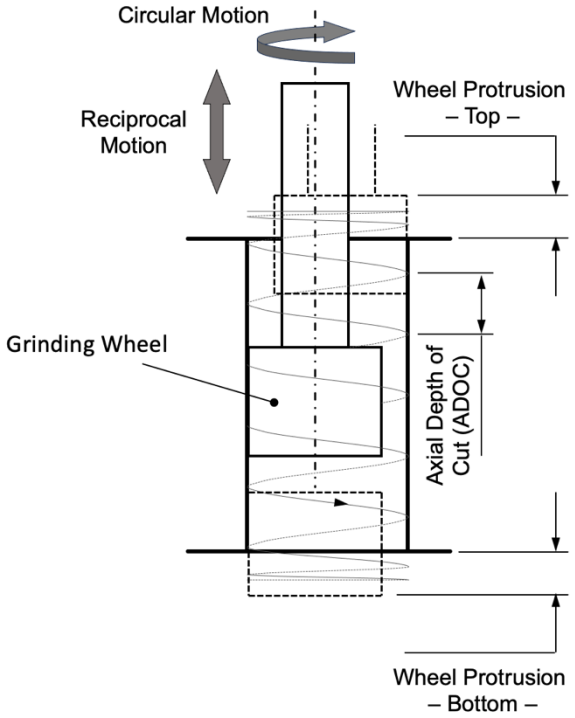

FIGURE 3: Axial depth of cut and wheel protrusion in jig-grinding

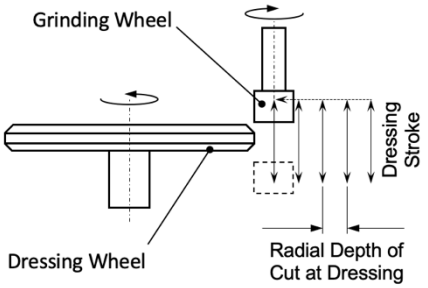

FIGURE 4: Radial depth of cut at dressing

TABLE 1: Input parameter and levels

Parameter	**Level 1**	**Level 2**	**Level 3**
P1 [mm]	1.0	2.5	4.0
P2 [mm]	1.0	2.5	3.5
P3	5	8	18
P4 [m/min]	630	900	1400
P5 [µm]	0.5	1.5	3.0

In accordance to the design catalogue by Taguchi, an L18 Orthogonal Array with the number of Parameters P=5 and Levels L=3 was found suitable for this investigation [2]. The number of experiments were reduced from 243 to 18. TABLE 2 highlights the selected Orthogonal Array and shows the combination of parameters and their levels for each experiment. To achieve validity and accuracy each experiment was repeated 12 times.

TABLE 2: Orthogonal Array L18 shows the investigated parameter and the levels for each experiment

Expt. #	Investigated Parameters				
	P1	**P2**	**P3**	**P4**	**P5**
X_1	1	1	1	1	1
X_2	1	2	2	2	2
X_3	1	3	3	3	3
X_4	2	1	1	2	2
X_5	2	2	2	3	3
X_6	2	3	3	1	1
X_7	3	1	2	1	3
X_8	3	2	3	2	1
X_9	3	3	1	3	2
X_{10}	1	1	3	3	2
X_{11}	1	2	1	1	3
X_{12}	1	3	2	2	1
X_{13}	2	1	2	3	1
X_{14}	2	2	3	1	2
X_{15}	2	3	1	2	3
X_{16}	3	1	3	2	3
X_{17}	3	2	1	3	1
X_{18}	3	3	2	1	2

EXPERIMENT SETUP

The experiments were conducted on the newly developed Moore Nanotechnology System Ultra-Precision M600 jig-grinder. This machine is equipped with four linear axes; X, Y, Z and, W (FIGURE 5). To attain an ultra-precision and error-free reversal motion, the machine axes are designed with friction-free hydrostatic bearings, one nm feedback resolution, and a dual linear motor arrangement. Unlike conventional jig-grinders, the required planetary tool motion is generated through a simultaneous X/Y-Axis and a reciprocal W/Z-Axis motion.

The test parts that were used for the experiments geometrically resemble a stacked optical mold plate assembly. These test parts, with the main dimension of (length x width x height) 110 x 110 x 50 mm, consists of 12 equally placed holes along the perimeter, with a nominal diameter of Ø10

mm and a depth of 50 mm (FIGURE 1). The test part material is a D2 type tool-steel with a hardness of 52 - 54 HRC. The MacroNano System-3R, a precision clamping system, was used for holding the test part on the machine table.

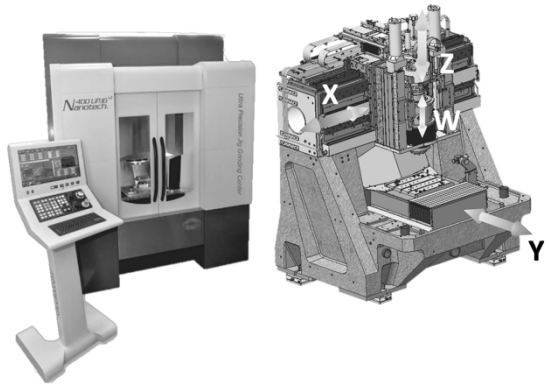

FIGURE 5: Moore Nanotechnology Systems M600 Ultra Precision Jig-Grinder

Vitrified CBN grinding wheels with a grit size of 46 µm and a concentration of 150 were used. The nominal grinding wheel diameter was Ø8.5 mm with a height of 5 mm. To minimize tool deflection during the grinding process, the grinding tool shanks are made of carbide with a diameter of Ø7 mm. Further, these tools are held in the spindle via a clamping flexure based on an HSK-E25 spindle/tool interface. Prior to each grinding experiment, the tools were dressed via a Ø 30 mm rotary diamond dressing disc at a speed ratio of 65% and an overlap ratio of 50%.

To determine the cylindrical deviation, the cross-sectional roundness, radii PV, and the curvature of the ground holes, a Mitutoyo roundness gauge, model RA-H5200, was used. The measurements ware acquired in four equally spaced depth locations inside the holes (FIGURE 6).

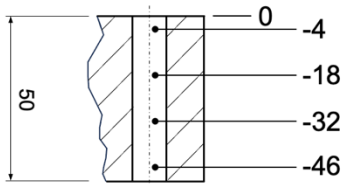

FIGURE 6: Hole measurement locations

ANALYSIS OF THE EXPERIMENTS

Based on the specified L18 Orthogonal Array, each experiment (X_1 to X_{18}) was carried out 12 times, and all the deviations from the cylindrical form as well as its influencing component roundness, radii PV, and curvature are measured. FIGURE 7 illustrates, for example, the measured roundness at the four specified depths of experiment X_{17} for all 12 trials. The average results of the 12 trials for each conducted experiment are listed in TABLE 3 below.

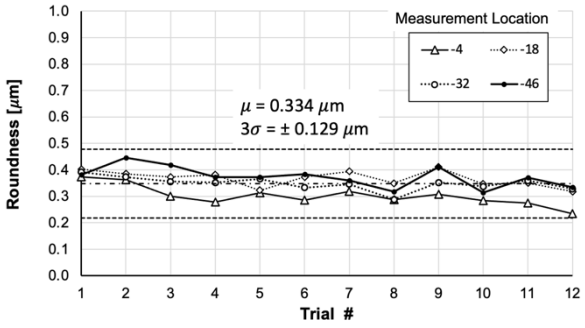

FIGURE 7: Roundness results of experiment X_{17}

TABLE 3: Trial average roundness, radii PV, curvature, and cylindrical deviation for the 18 experiments

Expt. #	Round. [µm]	Radii PV [µm]	Curve. [µm]	Cyl. [µm]
X_1	0.626	0.420	0.081	1.475
X_2	0.434	0.289	0.046	0.978
X_3	0.389	0.389	0.021	0.784
X_4	0.458	0.356	0.033	0.762
X_5	0.473	0.179	0.072	0.801
X_6	0.421	0.785	0.036	1.395
X_7	0.498	0.289	0.067	0.894
X_8	0.389	0.501	0.077	0.942
X_9	0.521	0.634	0.058	0.878
X_{10}	0.287	0.189	0.024	0.501
X_{11}	0.501	0.601	0.092	1.376
X_{12}	0.441	0.589	0.088	0.926
X_{13}	0.399	0.189	0.073	0.632
X_{14}	0.402	0.498	0.068	0.964
X_{15}	0.421	0.147	0.084	0.621
X_{16}	0.272	0.258	0.054	0.534
X_{17}	0.334	0.473	0.073	0.891
X_{18}	0.435	0.631	0.069	1.029

Initial observations indicates that the investigated parameters have an insignificant influence on the curvature. Further, increasing the grinding wheel speed not only improves the roundness but also the radii PV, and the overall cylindricity. The average results for each level of the investigated parameters are summarized as Margin Means plots in FIGURE 8.

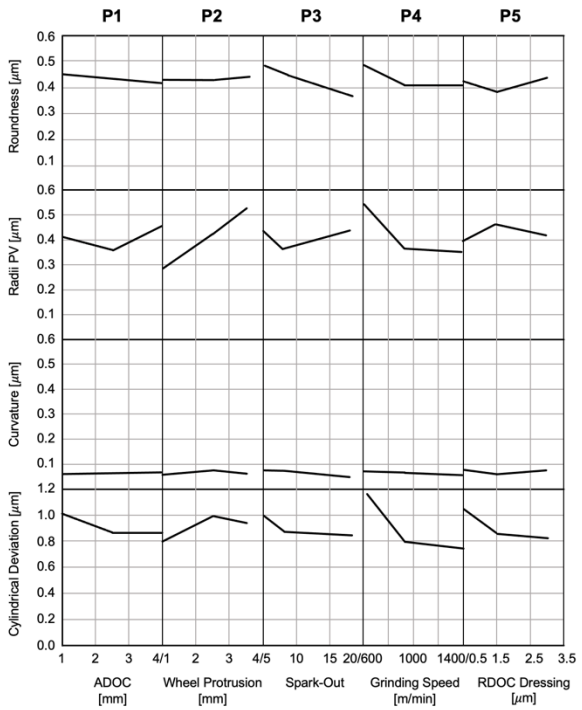

FIGURE 8: Margin Means plot of the curvature, radii PV, roundness, and cylindrical deviation

To determine the effect of each parameter on the result output, the signal-to-noise ratio (SN-ratio) needs to be calculated for each experiment. The SN-ratio is a simple quality indictor describing the effect of changing a particular process parameter on the outcome. In other words, a better signal is obtained when the noise is smaller so that the S/N ratio is larger [2].

Since the objective of this investigation was to minimize the deviation from the cylindrical form as well as its components, the SN-ratio is calculated as:

$$SN_i = -10 \log \sum_{T=i}^{N_i} \frac{y_T^2}{i}$$

The abbreviation *i* represents the experiment number, *T*, the trial number, and N_i, the number of trials for experiment *i*.

The calculated SN-ratios for each experiment are shown in TABLE 4 for roundness, radii PV, curvature and cylindrical deviation, respectively.

After determining the SN-Ratio for each experiment, the average SN_{AVR}-Ratio for each parameter level was calculated and tabulated, and then the range of the average SN_{AVR}-Ratio for each parameter was obtained. The larger the range, the larger the effect a particular parameter had on the process. This is because a same change in signal causes a large effect on the process output. This method was applied to all the investigated criteria: roundness, radii PV, curvature and cylindrical deviation (*TABLE 5)*.

TABLE 4: SN-Ratios for roundness, radii PV, curvature and cylindrical deviation for experiment $X_1 – X_{18}$

Expt. #	SN-Ratio			
	Round.	Radii PV	Curve.	Cyl.
X_1	4.054	7.484	21.396	-3.381
X_2	7.224	10.756	26.536	0.187
X_3	8.198	8.146	33.267	2.098
X_4	6.653	8.945	29.506	2.287
X_5	6.485	14.896	22.794	1.876
X_6	7.534	2.057	28.811	-2.801
X_7	5.967	10.585	23.409	0.943
X_8	8.178	5.957	22.255	0.499
X_9	5.657	3.901	24.464	1.048
X_{10}	10.832	14.420	31.960	5.899
X_{11}	5.978	4.389	20.252	-2.876
X_{12}	7.045	4.513	20.983	0.645
X_{13}	7.925	13.978	22.721	3.943
X_{14}	7.878	5.954	23.295	0.287
X_{15}	7.467	16.589	21.182	4.109
X_{16}	11.289	11.702	25.185	5.437
X_{17}	9.478	6.474	22.740	0.987
X_{18}	7.197	3.824	23.168	-0.343

As seen in the above table, the parameter with the largest effect on the hole roundness is the number of spark-outs (P3) that were exercised after the finishing cut. In conjunction with level testing results, as highlighted in FIGURE 8, an increasing number of spark-outs could result in smaller roundness values.

In regard to the radii PV, the first effecting parameter is the wheel protrusion (P2) during the direction reversal of the reciprocating motion. This could contribute to the deflection of the grinding wheel caused by the cutting forces when in contact with the workpiece. These cutting forces are proportional to the grinding wheel width-engagement with the workpiece. The less the grinding wheel width is in contact with the workpiece, the lower the cutting and lesser tool deflection is expected. Hence, when reversing the reciprocating motion at the top and bottom of the hole, the amount of the wheel deflection changes. The further the griding wheel is exposed from the hole, the lower is the deflection,

resulting in an increase of local diameters at the top and bottom of the hole.

TABLE 5: Parameter ranking for the investigated criteria

Criteria: ***Roundness***					
Level	Parameter				
	P1	**P2**	**P3**	**P4**	**P5**
1	7.222	7.787		6.435	7.369
2	7.324	7.537	6.974	7.976	7.546
3	7.961	7.183	8.985	8.096	7.592
Max-Min	0.739	0.604	2.437	1.661	0.223
Rank	***3***	***2***	***5***	***4***	***1***

Criteria: ***Radii PV***					
Level	Parameter				
	P1	**P2**	**P3**	**P4**	**P5**
1	8.285	11.186	7.964	5.716	6.744
2	10.403	8.0710	9.759	9.744	8.959
3	7.074	6.505	8.039	10.303	10.059
Max-Min	3.329	4.681	1.795	4.587	3.316
Rank	***3***	***5***	***1***	***4***	***2***

Criteria: ***Curvature***					
Level	Parameter				
	P1	**P2**	**P3**	**P4**	**P5**
1	-13.12	-15.04	-12.61	-11.58	-12.60
2	-14.51	-13.24	-13.82	-14.26	-13.45
3	-12.75	-12.10	-12.98	-14.54	-14.32
Max-Min	1.761	2.943	1.206	2.959	1.720
Rank	***3***	***5***	***1***	***4***	***2***

Criteria: ***Cylindrical Deviation***					
Level	Parameter				
	P1	**P2**	**P3**	**P4**	**P5**
1	0.429	2.521	0.362	-1.362	-0.018
2	1.617	0.160	1.209	2.194	1.492
3	1.429	0.793	0.270	2.642	2.000
Max-Min	1.188	2.361	0.938	4.004	2.018
Rank	***2***	***4***	***1***	***5***	***3***

The second dominant effect on the radii PV is the wheel speed (P4). Many studies have shown that an increase of the wheel speed reduces the cutting forces, and with it, the overall tool deflection. Therefore, an overall lower tool deflection results in a lower diametrical variation of the hole or its radii PV.

Concerning the curvature, the most dominant effecting parameters are wheel protrusion (P2) and grinding wheel speed (P4). However, since the actual deviations of the curvature are much smaller than the roundness and the radii PV, it can be anticipated that the curvature will have a minor effect on the cylindrical deviation.

In summary, the length of wheel protrusion, wheel speed, and the number of spark-outs have the greatest influence for achieving hole roundness and cylindrical deviation < 0.5 µm. In conjunction with the Marginal Mean plots, a set of optimized process parameters were defined and tested. The following were the selected parameters:

P1 (axial depth of cut) = 2.5 mm
P2 (wheel protrusion) = 1 mm
P3 (number of spark-out) = 18 mm
P4 (grinding speed) = 1400 m/min
P5 (radial depth of cut during dressing) = 3 µm

VALIDATION EXPERIMENT

Based on the established optimized parameters, a validation experiment was conducted to verify whether the selected parameters could render roundness and cylindrical deviation < 0.5 µm. Further, it also determines process stability over an extended trial testing. With the exception of the above listed parameters, all the experimental conditions and setups are kept the same as the previously conducted experiments. In all, 60 consecutive grinding trials were undertaken without any intermediate dressing. The purpose for this was to observe if a tool wear could affect the process stability through displaying any trend conditions in roundness and cylindrical deviation. FIGURE 9 illustrates the results of the validation test.

The conducted testing showed that the combination of the established parameters enabled meeting the objective to achieve a roundness and cylindrical deviation < 0.5 µm. The average roundness of 60 holes, measured at the previously defined 4 depth location, is 0.270 µm with a standard deviation of $3\sigma = \pm 0.171$ µm. The average cylindrical deviation is 0.469 µm with a standard deviation of $3\sigma = \pm 0.171$ µm. Although, no particular trend of the cylindrical deviation was observed, the roundness data for the first 30 trials shows a variation in roundness throughout each hole of about 0.12 µm. This variation becomes smaller with increasing grinding trials. In contrast, the radii PV shows an upward trend with the number of trials starting below the average of 0.173 µm and increasing, after 60 trails, to about 0.26 µm. It is believed that these trends are a result of moderate tool wear. While a sharper grinding wheel cuts better form accuracy, a worn wheel exhibits higher cutting forces that cause

higher tool deflection, which causes an increase in the radii deviation throughout the hole.

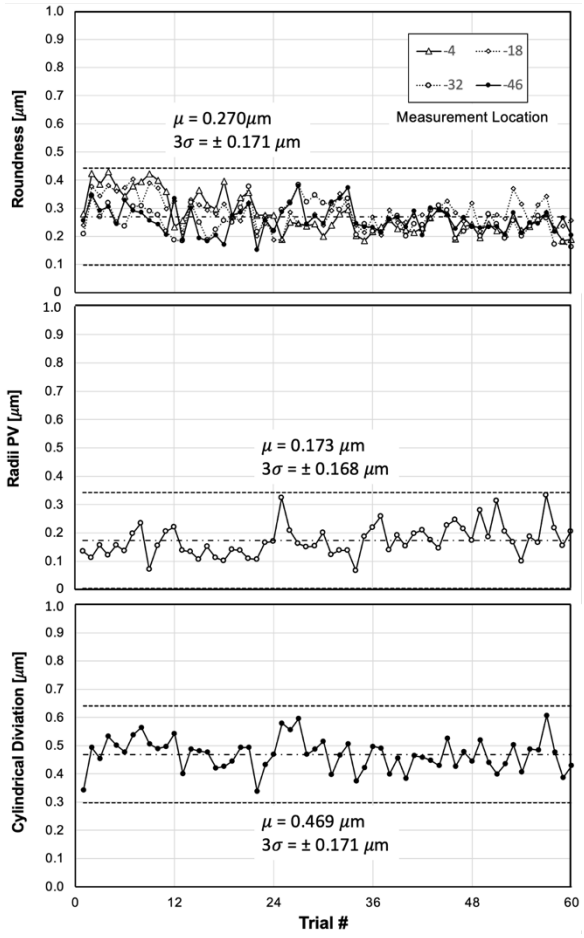

FIGURE 9: Validation results of roundness, radii PV, and cylindrical deviation

CONCLUSION

The objective of the presented work was to establish optimal process parameters by applying the Taguchi method, enabling to ultra-precision jig-grind cylindrical holes with an accuracy of cylindrical deviation and roundness under 0.5 μm. The output parameters for this analysis were defined by the classifying components of the cylindrical deviation; curvature, radii PV, and cross-section roundness deviations. Further, the use of signal-to-noise ratio helped to determine the effect and influence of the process parameters axial depth of cut, wheel protrusion height during the reversal of the reciprocating motion, number of spark-outs, grinding wheel speed, and the radial depth of cut during the rotary dressing process. The analysis showed that the grinding wheel speed and the wheel protrusion during the reversal of the reciprocating motion are the most dominant parameters influencing the output response of the hole radii PV. In contrast, the cross-sectional roundness deviation is mostly influenced by the number of spark-outs. Validation testing with the established optimum parameter set confirmed roundness and cylindrical deviation < 0.5 μm.

REFERENCES

[1] Fowlkes W., Creveling C., Engineering Methods for Robust Product Design; Addison-Wesley: 1995.

[2] Cimbala J., Taguchi Orthogonal Arrays; Penn State University, September 2014.

[3] Sudheesh P.K., Govindan P., A Review of Literature on Analysis of Jig Grinding Process, i-manager's Journal on Mechanical Engineering, Vol.6, May-July 2016.

[4] Geometrical product specifications (GPS) – Cylindricity, Part 1: Vocabulary and parameters of cylindrical form. ISO 12180-: 2016.

[5] Sudheesh P.K., Govindan P., Experimental Investigation and Optimization of Jig Grinding Process, International Journal of Research in Engineering & Technology, Vol. 1, August 2013.

ISO Standard on geometric accuracy of axes of rotation – An update

Alkan Donmez
Engineering Laboratory
National Institute of Standards and Technology
Gaithersburg, MD USA

ABSTRACT
First ISO standard on geometric accuracy of axes of rotation (ISO 230-7), which was published in 2006, was based on the culmination of knowledge and experience starting with the original paper, *Spindle Accuracy* by J. Bryan and his colleagues, published in American Machinist magazine in 1967, *CIRP Unification Document on Axes of Rotation* published in 1976, and *ASME B89.3.4 Standard on Axes of Rotation* published in 1986. It introduced the concepts of axis average line, fixed and rotating sensitive directions, synchronous and asynchronous error motions in axial, radial, face, and tilt directions among others. The original paper and the other documents followed considered mainly turning and boring machine spindles with structural symmetry, creating simplification for dealing with fundamental error motion. Application of this standard to rotary tables and other spindles with potential structural asymmetry created the need for reconsideration of those simplifications resulting in the revision of the standard, which was published in 2015. In the updated version of the standard, fundamental error motion, structural asymmetry, and consequences of axis of rotation error motions are clearly described. This presentation will summarize the historical perspective on axis of rotation standardization efforts and the latest version of this international standard with some examples.

Fully automated Multi-Probe Spindle Error Analysis (SEA)

Ralf Dupont
Levicron GmbH
Kaiserslautern, Germany

ABSTRACT

In this paper a fully automated multi-probe system using more than two sensors for a radial Spindle Error Analysis (SEA) to separate the current target shape error from the spindle synchronous errors and to detect the actual angles between these sensors is introduced. The axial SEA is done simultaneously with the radial SEA, and four sensors in total are used. To allow a reliable and consistent spindle qualification in production it is designed and programmed to set up the drive, run the spindle at different speeds and to read running properties like motor current, air flow or power losses to abort a measurement whenever any value is outside a given range. The spindle data and thresholds are stored in a static system data base and allows even non-expert personnel to perform a spindle SEA after the sensors have been set. The measurement, the evaluation and the assessment of the results are then done by the software, and all reports and raw data are stored under a folder of the spindle serial number on a network or local drive as well as in a dynamic products database for an AI-assessment.

PREFACE

Spindles used for ultra-precision machining require their rotation errors to be in the range of only a few nanometers to create optical components. However, a Spindle Error Analysis (SEA) comes with several difficulties. Because of electrical noise, vibrations and elastic deformations caused by centrifugal and thermal loads, reliable and repeatable results with nanometer resolution and at spindle speeds of several 10,000 rpm require very sophisticated evaluation, hard and software methods. Also, if only two sensors are used to measure radial spindle errors, any shape error of the target you measure against would be identified as spindle synchronous error. As the shape of the target itself changes with speed and thus temperature, this shape error is not consistent. If only one sensor is used for a radial SEA, the very time-consuming and error-prone “Donaldson Reversal” method has to be used.

NOMENCLATURE

- k - Sensor number
- $m_F(\phi)$ - Donaldson Reversal, 1st measurement
- $m_R(\phi)$ - Donaldson Reversal, 2nd measurement
- n - Fourier coefficient order
- r_0 - nominal artifact radius
- $r_n(\phi)$ - artifact shape error of the n^{th} harmonic at shaft angular position ϕ
- $s_k(\phi)$ - distance information of sensor k at shaft angular position ϕ
- $s_{kn}(\phi)$ - n^{th} complex Fourier-coefficient of the k^{th} sensor data
- x - complex spindle sync. and artifact shape error vector
- $x_n(\phi)$ - spindle synchronous error of the n^{th} harmonic in x-direction at shaft angular position ϕ
- $y_n(\phi)$ - spindle synchronous error of the n^{th} harmonic in y-direction at shaft angular position ϕ
- ϕ - angular shaft position
- ϕ_k - static sensor k angular position

SPINDLE ERROR ANALYSIS (ISO230-7 EXT) – traditional single-sensor vs. modern multi-sensor solutions

The deviation of the actual rotation axis of a spinning spindle shaft from a virtual and ideal one is called “shaft error in motion”. This error can be separated into synchronous errors, which repeat every shaft rotation at the same angular position of the shaft, and asynchronous errors, which are non-repeatable. Synchronous motion errors of spindle shafts can be caused by shape errors of parts involved in the rotation, asynchronous by natural frequencies, external disturbances or simply turbulences. Although run-out (fundamental) is a synchronous error you could reduce it to zero by tapping the tool/artifact into the center of rotation. Thus run-out is not a spindle, but a tool alignment error.

(1)

$$Error\ Motion = \sum SyncErrors - Fund\ (run\ out) + \sum AsyncErrors$$

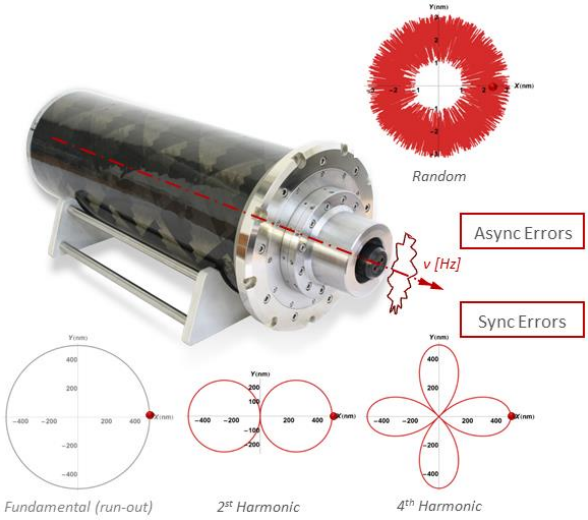

Figure 1: Repeatable (sync.) and non-repeatable (async.) spindle errors

By comparing errors over several rotations synchronous errors can be separated from asynchronous errors. However, as measurements are taken against a tool or artifact mounted onto the spindle shaft or the shaft itself, shape errors of this object would repeat and be identified as synchronous errors. Thus, these shape errors need to be separated from the real spindle synchronous errors. With the Donaldson Reversal Method an initial measurement $m_F\ (\phi)$ is carried out. After stopping the spindle, the sensor axis needs to be aligned 180° from its original position around the artifact, and the artifact itself 180° from its original position against the shaft axis.
After a second measurement $m_R\ (\phi)$ using the modified set-up, the error readings of both measurements are subtracted from each other what then gives the spindle synchronous errors. It is apparent that the particular care required to re-align the sensor and the artifact and the time taken for this prevents this method to be used for non-expert and/or mass production of spindles. However, because of pretty much no heat and centrifugal load involved, the Donaldson Reversal method or a mapped ball/artifact are still excellent methods to determine synchronous errors of slow rotating axes.

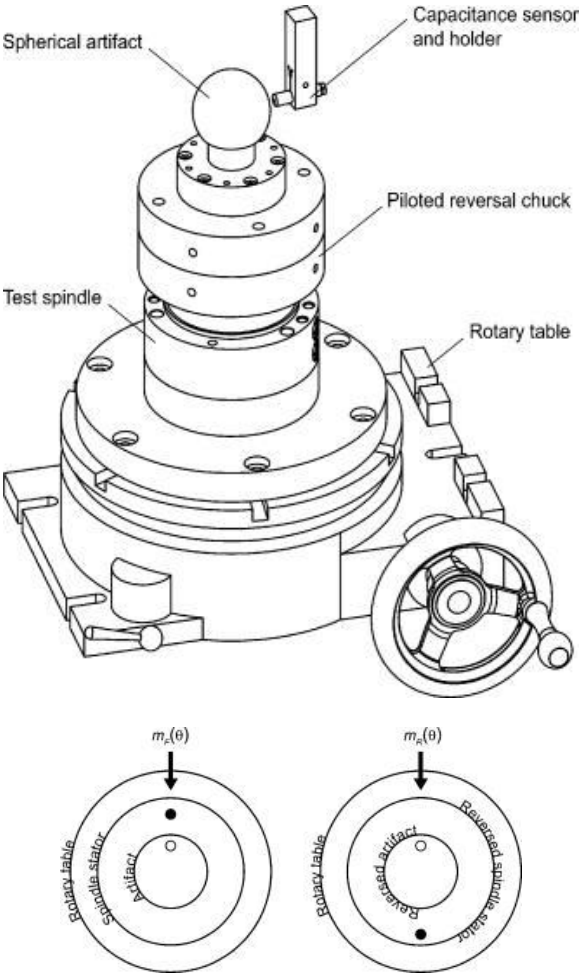

Figure 2: Donaldson Reversal method [1]

Beside the Donaldson Reversal, multi-sensor methods have been developed for radial SEA that can separate the artifact shape errors from the spindle synchronous errors during a measurement and without modifying its set-up. At least three sensors *k* are required from which each one takes several thousand distance measurements $s_k\ (\phi)$ per revolution. The distance information from each sensor over the same rotation are then transformed into the complex frequency domain, followed by calculating the complex Fourier coefficients $s_{kn}\ (\phi)$ for each of the *n* harmonics.

(2) [2]

$$s_k\ (\phi) = x(\phi) \cdot \cos(\phi_k) + y(\phi) \cdot \sin(\phi_k) + r(\phi - \phi_k) = Re\left(\sum_{n=1}^{\infty} s_{kn} \cdot e^{i(n \cdot \phi)}\right)$$

Along with the static angles ϕ_k between the sensors, equation system (3) can be solved to *x* for each harmonic *n*.

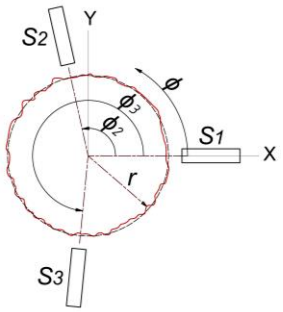

Figure 3: Coordinate systems and sensor angles

(3) [2]

$$\begin{bmatrix} s_{1n} \\ s_{2n} \\ \vdots \\ s_{4n} \\ \vdots \end{bmatrix} = \begin{bmatrix} \cos(\phi_1) & \sin(\phi_1) & e^{-i(n\cdot\phi_1)} \\ \cos(\phi_2) & \sin(\phi_2) & e^{-i(n\cdot\phi_2)} \\ & \vdots \; \vdots \; \vdots & \\ 0 \quad 0 & -i\frac{n}{r_0}\cdot e^{-i(n\cdot\phi_4)} & \\ & \vdots \; \vdots \; \vdots & \end{bmatrix} \cdot \begin{bmatrix} x_n \\ y_n \\ r_n \end{bmatrix}$$

$$= \boldsymbol{H} * \boldsymbol{x}$$

Its solution gives the spindle radial error in the two directions $x_n(\phi)$ and $y_n(\phi)$ for each harmonic and the artifact shape error $r_n(\phi)$ with the shaft angular position ϕ. The synchronous errors then can be summed up for all harmonics. After transforming the sum of all harmonics back into the time domain, they can be compared to each rotation of the original measurement. The difference corresponds to the asynchronous errors.

The Donaldson-Reversal method requires very sophisticated mechanical set-ups and very skilled personnel. For a multi-sensor system, on the other hand, the exact sensor calibration values and a synchronized measurement of all sensors are key. Although the exact angles between the sensors are required, the determination of these can be put into an algorithm that searches the sensor angles at which the sum of the synchronous and asynchronous errors are at a minimum.

SYSTEM DESCRIPTION

The goal was not only to automate the measurement itself, but also to autonomously control and monitor the spindle and to store raw data and reports in a custom spindle folder on the network without any user interaction.

Two database entities are used. The static system database contains of a user list, calibration tables and all spindle/machine definitions like naming and thresholds for vibrations, temperatures, motor current or power losses. This database is fully customizable with an initial GUI should the software not find a valid system database at start up. The location where all the testing data of a specific spindle are stored depends on these definitions and the spindle serial number.

The dynamic product database, on the other hand, contains of all data like type, history and measurement results and data that have been acquired for a single spindle serial number in the past. Before any testing, the spindle must be loaded and identified by its serial number. With this the system knows the type and thus all thresholds and drive values like kp, tn, max. speed, accelerations etc. This is done using a QR code laser marked on the spindle housing, but before testing the operator has to confirm serial number and type to make sure drive set-up, speeds and ramp times are correct. The capacitive sensors have to be set manually before any measurement. Although a safe working distance is continuously monitored by the software, this still has to be done manually. After starting a measurement, the software controls the spindle drive and monitors values for tool clamp, speed, temperature, motor current, motor voltage, air consumption, vibrations, power losses and sensor working distances. In the case any of these values is outside the range specified in the system database, the software stops the spindle and ends the measurement with an error-description.

As the sensor angles for the radial SEA slightly change between two set-ups, the software does an initial measurement at 50% of the nominal spindle speed, loads the raw data to work with invariant information and detects the current angles autonomously. For a successful measurement and report generation the software then commands a constant speed, let the spindle settle for 120 seconds, takes a radial and/or axial measurement, moves on to the next speed step and repeats this until the nominal speed of the spindle is reached. With each measurement the raw data of all (4) sensors and the trigger is stored in the spindle folder. After all measurements are done, the software generates a report, stores it in the spindle folder and gives the operator an idea of the SEA quality using a statistic module. The statistic module uses all measurements taken for this spindle type in the past and compares the current results with the gauss distribution. Should the SEA quality be outside a +25% range of the gauss distribution the software gives a warning and marks the SEA measurement for the spindle as done, but incomplete.

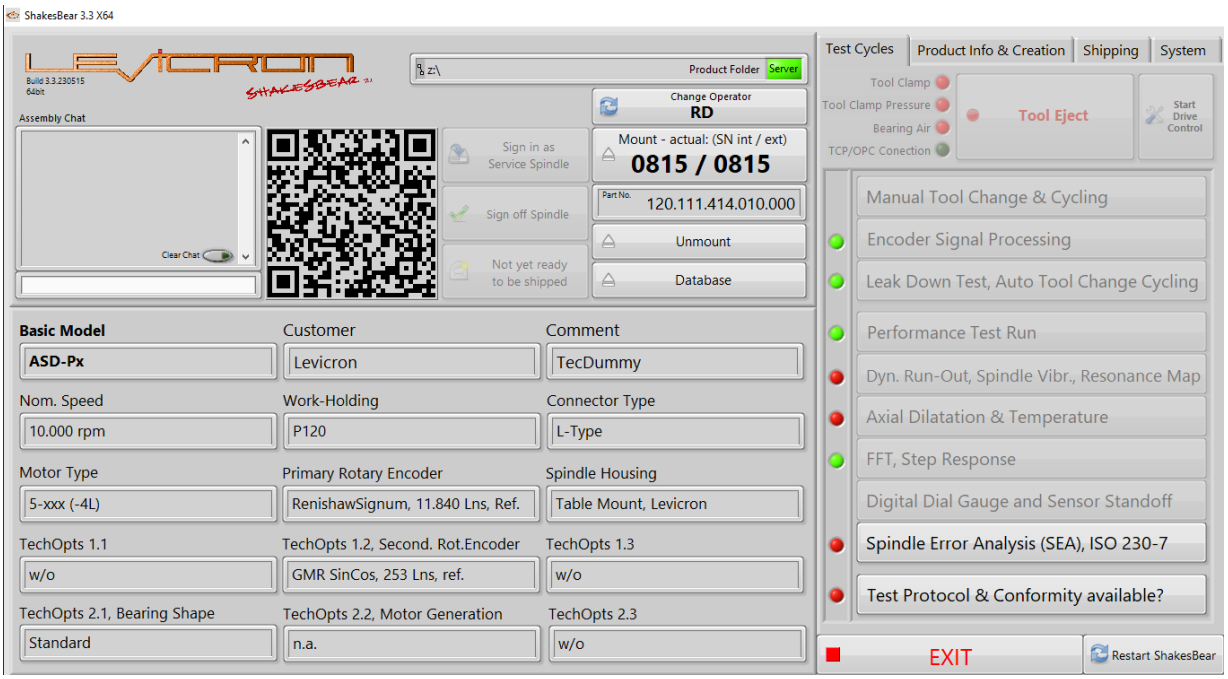

Figure 4: ShakesBear GUI using two database entities – system (static) and serials (dynamic)

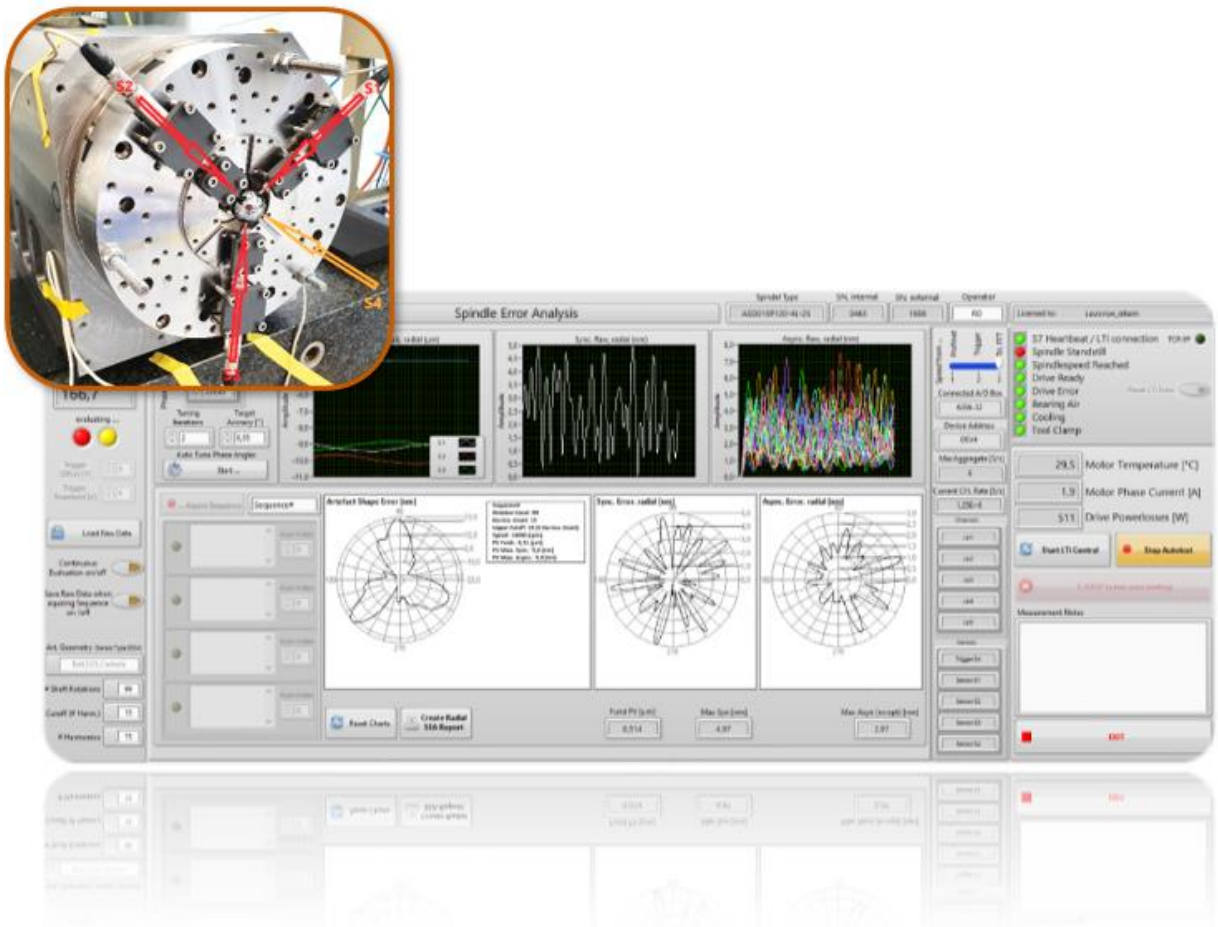

Figure 5: Measurement set up and control/evaluation software

AUOMATION, DRIVE CONTROL AND MONITORING

The communication to control and program the spindle drive and to receive current values of the spindle is done using Profinet protocol. The specific Profinet codes of the drive are received and transmitted from/to a Siemens PLC which also runs a proprietary “Open Platform Communication” (OPC) server. The OPC Server side receives the drive commands like speed changes or start/stop from the software, translates it to the drive-specific Profinet code and sends it to the drive. At the same time, it reads out the current drive values and state, translates it into an OPC code and forwards it to the software for evaluation. By calling a spindle serial number within the software, the system database also provides the drive parameter set number with which the drive loads the correct parameters to run the spindle. Any reading of all four distance sensors is taken simultaneously and at a sample rate of 312.5 kS/s per channel, what makes a bandwidth of 1.25 MS/s. The differential evaluation of each sensor allows a physical resolution of 0.9 nm.

The software evaluation however allows a higher resolution. An averaging over several rotations gives more consistent and more precise results with respect to the synchronous spindle errors. This applies for both, the radial and axial SEA, where for the axial measurement no error separation of the spindle synchronous errors and artifact shape error is needed as long as the axial measurement axis is the same as the rotation axis of the spindle shaft.

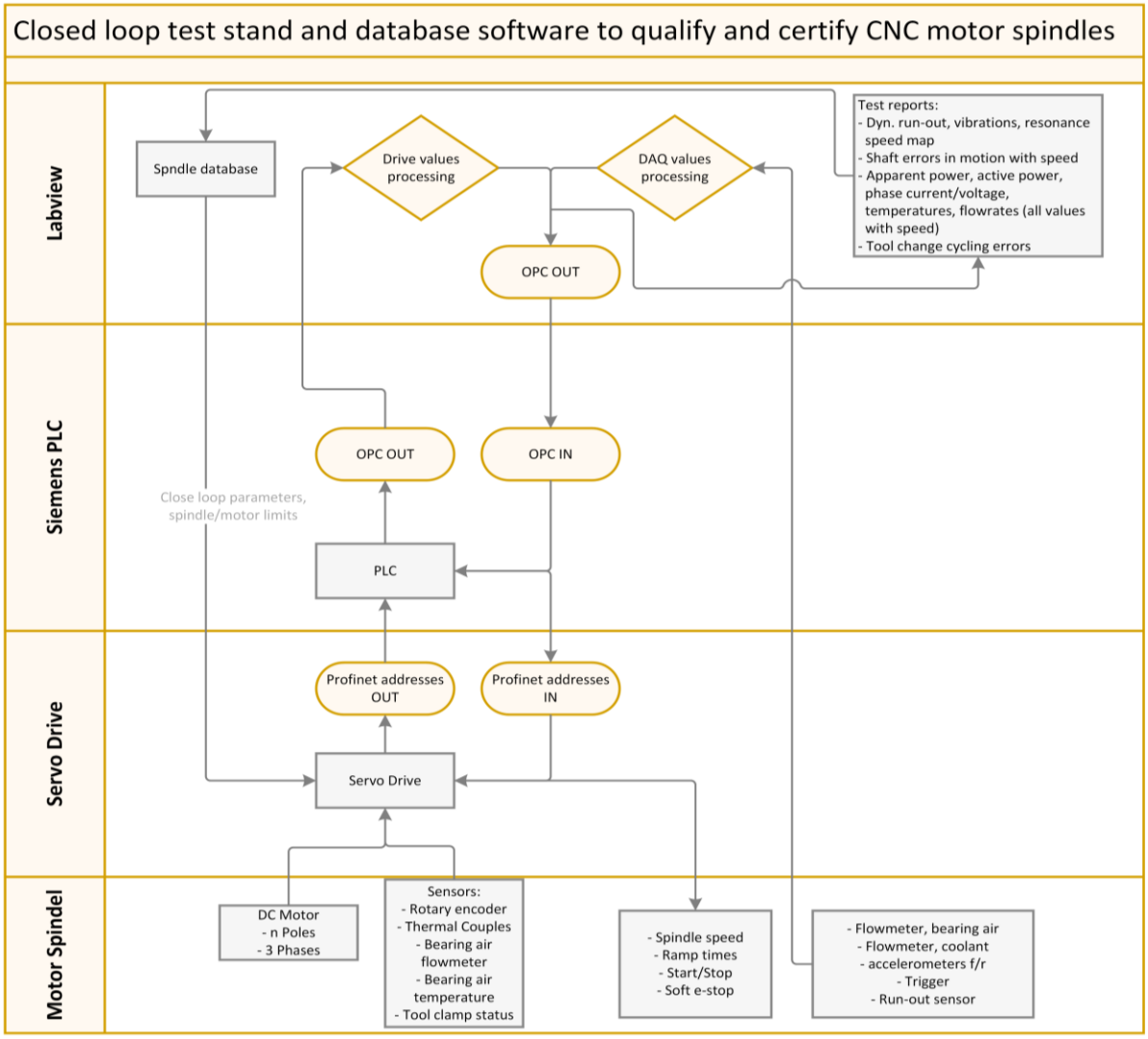

Figure 6: Closed loop control and evaluation/report flow chart

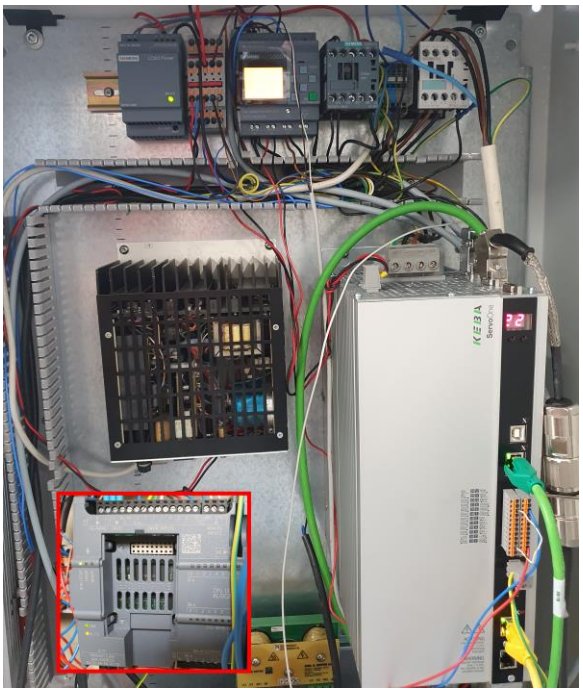

Figure 7: Automation, drive and Profinet/OPC cabinet

DYNAMIC RESULTS INTERPRETATION AND ASSESSMENT (AI)

All measurement results are stored automatically as raw data and reports in the product folder of a spindle serial number. At the same the dynamic product database is updated with key figures of these measurements. All results of a single spindle type within the product database are used to calculate a Gauss-Normal-Distribution that allows an automated and continuous assessment of the spindle that is being tested and compared to all previous measurements. Also, the trend over time can be calculated and allows a manual assessment of the spindle quality over time.

Should the SEA evaluation exceed +25% of the mean value of the Gauss-Distribution during a test, the system gives a warning, at values exceeding +45% it automatically aborts the test. It evaluates if either the synchronous, the asynchronous or both spindle errors are outside the expected range and gives the operator suggestions for counter measures. Should the fundamental show a steep increase, then balancing is likely to be the root cause. Should the second harmonic be larger than expected, the shaft centers for grinding are likely the reason that have generated journal bearings with shape errors during finish grinding. In the case the spindle asynchronous errors are higher than expected, bearing stiffness and/or damping might be insufficient.

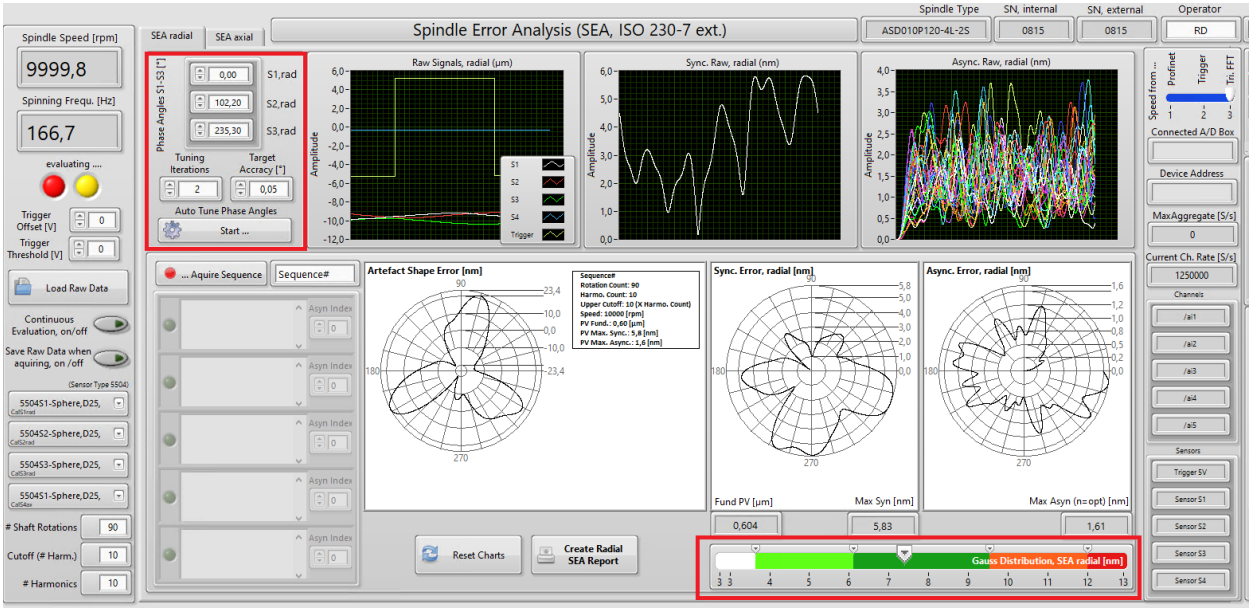

Figure 8: Automated sensor angle evaluation and Gauss-Distribution comparison

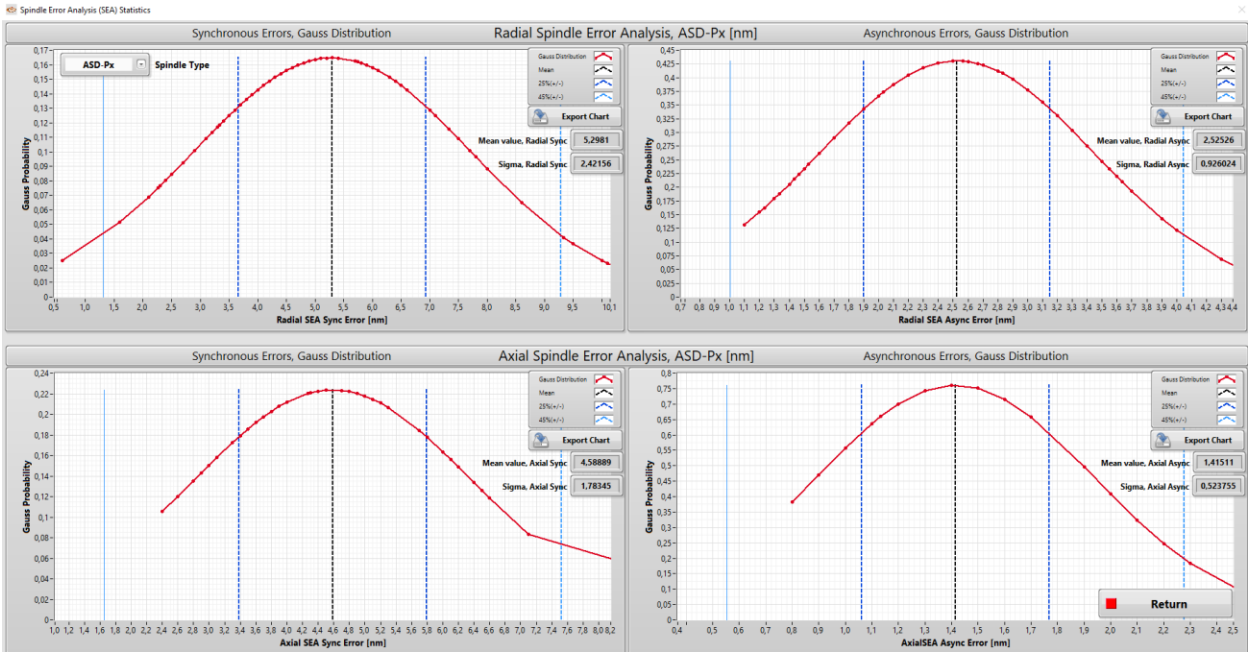

Figure 9: Current Gauss-Distribution of all axial and radial SEAs

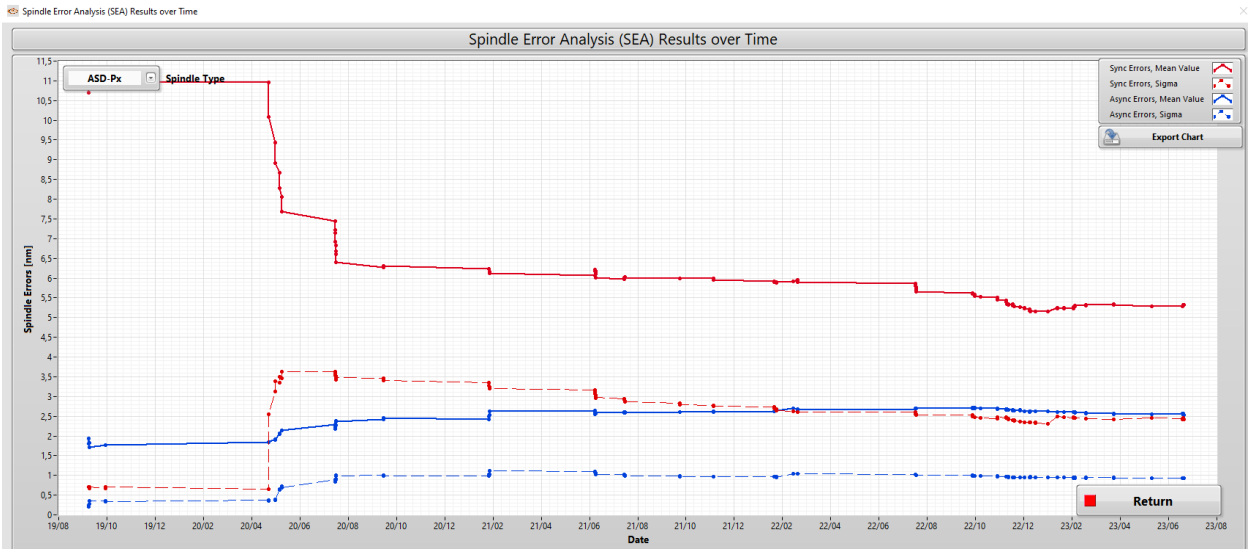

Figure 10: Mean value and standard deviation for synchronous and asynchronous spindle errors over time

AUTOMATED REPORT GENERATION

After a successful SEA, the software generates a report for the end-customer covering artifact shape, synchronous and asynchronous errors at different speeds. The reports are stored along with the raw data in the folder of the spindle serial number. It then marks the SEA section in the main panel (Figure 4) as completed (green). Only after all tests for this spindle type have been completed, it enables the function of the final acceptance, and only after the final acceptance the system reports the spindle to the shipping department to be ready for packing.

Levicron GmbH, Clara-Immerwahr-Str. 2, 67661 Kaiserslautern, Germany, info@levicron.com, +49 6301 66800 0, levicron.com

Spindle Details

Spindle Type	ASD010V200-4L-2S
Serial no., external	2620
Customer	
Inspector	RD
Date	2022-08-15, 12:20

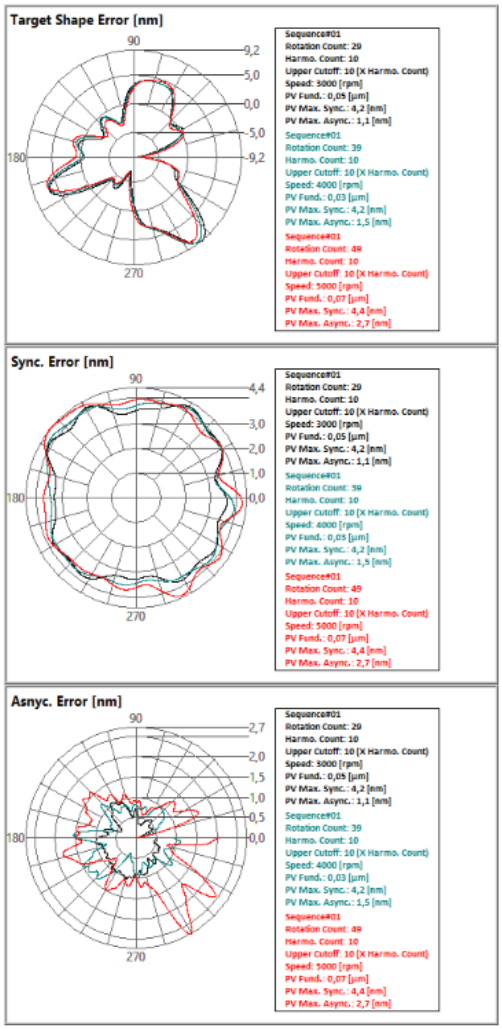

Figure 11: Error-Motion protocol of a fully automated test run

CONCLUSIONS

As a result, the described SEA method and test rig allow fully automated, reliable and repeatable SEA testing and reporting with sub-nanometer resolution at spindle speeds of up to 100.000 rpm. The automation and the spindle data base with all drive parameters and thresholds for the load spindle serial number prevent an unsafe testing or spindle operation as well as automated reporting and raw data recording. An automated assessment of the results based on a Gauss-Distribution of all measurements for this spindle type in the past gives excellent quality control and provides suggestions of likely root causes. A guided testing and result assessment from assembly to final acceptance prevents errors and mistakes at the earliest point possible and ensures a constant or even improving quality over time.

OUTLOOK

As an improvement, a mechanically and electrically automated sensor set-up before the actual measurements is being developed.

REFERENCES

[1] Marsh ER. Precision Spindle Metrology. Destech Pubns Inc, 2nd Edition, 2009

[2] Jansen MJ et al. Advanced Spindle Runout-Roundness Separation Method. Advanced Mathematical and Computational Tools in Metrology V, 212-219, 2001

DEVELOPMENT OF A NEW HIGH-ACCURACY ANGLE GENERATOR

Christian F. Guertin
Vermont Photonics Technologies Corp.
Dummerston, VT, USA

Currently, one of the limiting factors in the quality of x-ray science that can be performed at synchrotron radiation (SR), or Free Electron Laser (FEL) light sources is the metrology of super-polished x-ray mirrors used to focus the x-rays. With the advent of FELs and next-generation, diffraction-limited SR, requirements for the surface figure of these mirrors will become tighter and tighter. State-of-the-art metrology labs at DOE facilities are using a slope-measuring scanning method to measure the surface form of the mirrors. A main source of error, keeping practitioners from reaching the accuracy required for current and next-generation mirrors, is the calibration of the autocollimator or other slope-measuring device [1].

In the early 1990's when electronic autocollimators became commercially available, a novel angle generating system was developed and deployed at the U.S. NIST and at the primary standards lab of the U.S. Air Force. The Advanced Automated Master Angle Calibration System (AAMACS) was based on a three-level stack of indexing tables that were capable of dividing the full circle into 379,080,000 discreet angular positions (i.e. 0.0034 arcsec resolution) [2]. Unfortunately, AAMACS proved too difficult to maintain in operation and neither of the two units that were produced are operable today. Autocollimator users in the x-ray mirror metrology community are currently pushing the angle metrology boundaries to unprecedented levels and doing so has required many to undertake time-consuming work with overseas laboratories.

The objective of this project is to build an angle generator that will fill the gap left in U.S. angle metrology by the demise of AAMACS. Given the demands of the x-ray mirror community, we set out to build a plane angle generator with positioning uncertainty less than 0.01 arcsec (50 nrad) over a 360º range for the calibration of autocollimators and other angular artifacts.

Specifically, we have built an air bearing rotary table capable of full rotation about a vertical axis. See FIGURE 1. The system is fitted with a multi-read head rotary encoder and will undergo a self-calibration procedure to compensate for intrinsic errors of the encoder ring [3].

FIGURE 1. The rotary air bearing and encoder system of the angle generator are set inside a granite table. The top surface of the angle generator is designed to accommodate a variety of potential payloads. The table itself is supported on pneumatic isolation legs.

It is possible to use the self-calibration procedure in multi-read head encoder systems because of two key properties: 1) a complete revolution is exactly 2π radian (i.e. a perfect standard of nature) and 2) the individual read heads are fixed and the angle between any pair of read heads is constant.

One step of the self-calibration process yields a measurement of the rotational errors of the axis on which the encoder is mounted, i.e. we measure the lateral shifting of the rotor at each rotational position. These results will be compared to a standard method for measuring these errors.

Results from preliminary work on a prototype system achieved angle accuracy below 0.1 arcsec. These will be presented along with the status of the full system and any measurement results available.

REFERENCES

[1] Yandayan T, Geckeler R, Siewert F. Pushing the limits – latest developments in angle metrology for the inspection of ultra-precise synchrotron optics. Proc. Of SPIE. 2014; 9206: 1-15.

[2] Estler W, Queen Y, Bryan J. An advanced angle metrology system. Ann. CIRP. 1993; 42: 573-576.

[3] Geckeler R, Link A, Krause M, Elster C. Capabilities and limitations of the self-calibration of angle encoders. Meas. Sci. Technol. 2014; 25:055003.

SUPER-ACCURATE ANGULAR ENCODER SYSTEM WITH MULTI-DETECTING HEADS USING VEDA METHOD

Nobuyuki Ishii
Laserscale Division
Magnescale Co. Ltd.
Isehara City, Kanagawa Prefecture, Japan

INSTRUCTIONS

The importance of precise angular measurement has increased with respect to machine tools and precision measurement equipment. A rotary encoder needs to be developed to ensure high accuracy in such machines.

Machine tools require further improvement regarding the processing accuracy of large, round work pieces. For example, in the energy industry, the machining accuracy of components is assumed to directly affect the energy conversion efficiency and lifetime of the components used in high-speed turbines or large gears of wind power generators [1], [2]. There is strong demand for rotary encoders with better accuracy and resolution to serve as a measurement reference, particularly for measurements of the surface accuracy of optical components or wafers that incorporate auto-collimators. These machine tools or precision measurement equipment use an autocollimator by placing a polyhedron mirror over the machine. This method can measure the number of points equal to the number of mirrors. This is not sufficient to meet further demands for increased accuracy in the future.

A rotary encoder can achieve high accuracy and resolution with high machining repeatability even if it is installed roughly without precise alignment. In response to the above requirements, multiple heads have been applied to the single rotary disc of an existing encoder to compensate for the calibration error. However, this increases the size of the encoder because of the many heads required. Thus, this approach is impractical for implementation in a machine tool system.

Furthermore, even if it can be installed, there is also a problem that when the rotary encoder itself has a rotating shaft, it cannot operate effectively, owing to mechanical interference caused by a mismatch with the rotating shaft of the rotary encoder and that of the spindle in the machine tool.

Therefore, a new principle of self-calibration with multiple detecting heads, which enables detection of the error components of a higher order with few detecting heads, was proposed and named “VEDA Method” [3]. The authors also proposed the optimized placement of six detecting heads based on this new principle of self- calibration. Furthermore, the feasibility and usefulness of the principle was verified through simulations using the measurement data of the angular accuracy on each individual detecting head. For the realization of a high- accuracy encoder based on this principle, a data processing board was developed, which can capture data from six detecting heads at the same clock timing, obtains angular data from each encoder on 360 points per cycle, and calculates the calibration coefficient for each point. Then, the board calculates the average of the angular data from six detecting heads in real time with linear interpolation to obtain the calibration coefficient. By calibrating the rotary encoder in which the scale with the gratings and sensor head for detecting are separated with this self-calibration method, a self-calibrating rotary encoder system with a practical size and attachable to a machine tool was developed. Therefore, the newly developed system achieved an accuracy of ± 0.03 (arcsec) as a rotary encoder with self-calibration in real time.

INTRODUCTION PRINCIPLE OF THE VEDA METHOD

To overcome these difficulties, a new method for self-calibration is proposed in this paper. In general, a sensor head at position θ with respect to the reference position of the detected value $H(\theta)$ of the rotary encoder can be represented as

$$H(\theta) = \theta + \varepsilon(\theta) \quad (1)$$

where θ is the angular position (0 to 2π) and $\varepsilon(\theta)$ is the periodic angle error term of the rotary encoder. The error term of the actual sensor has abroad frequency components. The error term is represented as

$$\varepsilon(\theta) = \sum_{n=1}^{\infty} C_n \sin(n\theta + \alpha_n) \quad (2)$$

where *n* is a positive integer, C_n is the amplitude of the *n*-th Fourier component, and α_n is the phase of the *n*-th Fourier component. If the reference position is at the 0th position of sensor heads positioned with *N* units of equal intervals over one cycle, the detected value $H^{(N,k)}(\theta)$ of the *k*-th head can be represented as follows:

$$H^{(N,k)}(\theta) = H\left(\theta + \frac{2\pi k}{N}\right) - \frac{2\pi k}{N} = \theta + \varepsilon\left(\theta + \frac{2\pi k}{N}\right) \quad (k = 0,1,\cdots,N-1) \tag{3}$$

Consider two sensor heads separated by an angle of $2\pi/N$ rad. The difference between the detected values $\delta^{((N,k))}(\theta)$ of the kth and $(k-1)$th sensor heads can be represented as follows:

$$\begin{aligned}\delta^{(N,k)}(\theta) &= H^{(N,k)}(\theta) - H^{(N,k-1)}(\theta) \\ &= \varepsilon\left(\theta + \frac{2\pi k}{N}\right) - \varepsilon\left(\theta + \frac{2\pi(k-1)}{N}\right) \\ &= \varepsilon\left(\left(\theta + \frac{2\pi}{N}\right) + \frac{2\pi(k-1)}{N}\right) - \varepsilon\left(\left(\theta + \frac{2\pi}{N}\right) + \frac{2\pi(k-2)}{N}\right) \\ &= \delta^{(N,k-1)}\left(\theta + \frac{2\pi}{N}\right)\end{aligned} \tag{4}$$

Accordingly,

$$\begin{aligned}\delta^{(N,k)}(\theta) &= \delta^{(N,k-1)}\left(\theta + \frac{2\pi}{N}\right) \\ &= \delta^{(N,k-2)}\left(\theta + 2\frac{2\pi}{N}\right) \\ &= \delta^{(N,1)}\left(\theta + \frac{2\pi(k-1)}{N}\right)\end{aligned} \tag{5}$$

Therefore

$$H^{(N,k)}(\theta) = \delta^{(N,1)}\left(\theta + \frac{2\pi(k-1)}{N}\right) + H^{(N,k-1)}(\theta) \tag{6}$$

where $\delta^{(N,1)}\left(\theta + \frac{2\pi(k-1)}{N}\right)$ is the phase shift of $\delta^{(N,1)}(\theta)$.

Therefore, the error of the sensor head at $2\pi k/N$ is described by the difference of error curve between 1st and 0th sensor head $\delta^{(N,1)}(\theta)\varepsilon\left(\theta + \frac{2\pi}{N}\right)$ and error curve between 1st sensor head:

$$H^{(N,k)}(\theta) = \sum_{j=1}^{k-1}\delta^{(N,1)}\left(\theta + \frac{2\pi j}{N}\right) + H^{(N,1)}(\theta) \quad (k = 2,3,\ldots,N-1) \tag{7}$$

In this manner, it is possible to calculate the detected value of the *N* sensor heads arranged at equal intervals. The *N*th-order components of the error $\varepsilon_N(\theta)$ can be described by using the principle of EDA method that "For any positive integer *N*, any arbitrary periodic curve generates a total *n* of curves whose angle phase shifts by $2\pi/N$ from the original curve. The averaged curve, from the total of *N* curves, has components that are integral multiples of the *N*-order Fourier components of the original curve." Therefore, the average of the detected values of the *N* equally distributed sensor heads, $\overline{H}^N(\theta)$ is a detection value having an error of only the *N*th order.

$$\overline{H}^N(\theta) = \frac{1}{N}\sum_{k=0}^{N-1}H^{(N,k)}(\theta) = \theta + \sum_{n=1}^{\infty}\varepsilon\left(\theta + \frac{2\pi k}{N}\right) \tag{8}$$

Substituting Eq. (8) into Eq. (9) yields

$$\begin{aligned}\overline{H}^N(\theta) &= \frac{1}{N}\left\{H^{(N,0)}(\theta) + (N-1)H^{(N,1)}(\theta) + \sum_{k=2}^{N-1}\left\{\sum_{j=1}^{k-1}\delta^{(N,1)}\left(\theta + \frac{2\pi j}{N}\right) + \varepsilon\left(\theta + \frac{2\pi}{N}\right)\right\}\right\} \\ &= \frac{1}{N}\left\{H^{(N,0)}(\theta) + (N-1)H^{(N,1)}(\theta) + \sum_{j=1}^{N-2}(N-1-j)\delta^{(N,1,j)}(\theta)\right\}\end{aligned} \tag{9}$$

As in the case of calculating equation (7) using equation (6), the error $\varepsilon(\theta + \frac{2\pi k}{N})$ from the sensor

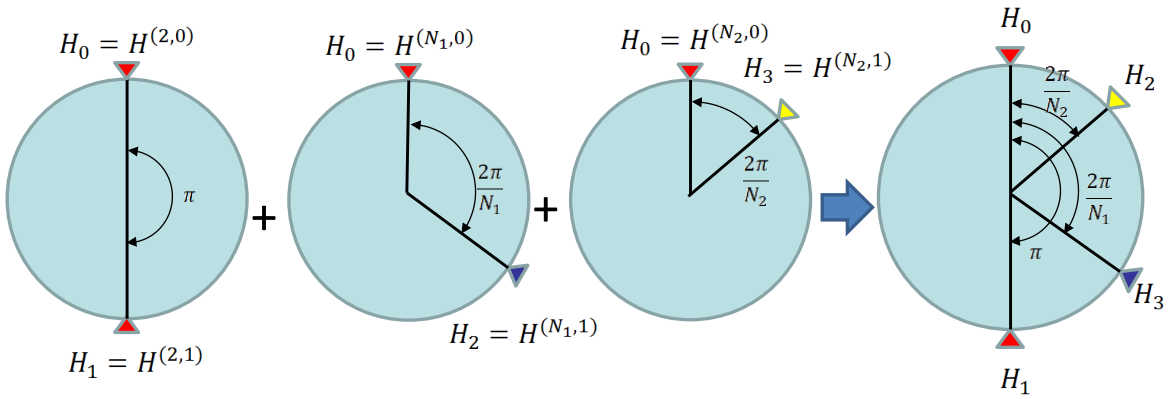

FIGURE 1. Arrangement of sensors required for calibration companioning three pairs with VEDA method.

head positioned at $2\pi k/N$ can be also represented as $\delta^{(N,1)}(\theta), \varepsilon(\theta)$:

$$H^{(N,k)}(\theta) = \sum_{j=0}^{N-k-1} \delta^{(N,1)}\left(\theta + \frac{2\pi(k+j)}{N}\right) + H^{(N,0)}(\theta) \quad (k = 2, \ldots N-1) \tag{10}$$

Substituting Eq. (11) into Eq. (9) yields

$$\overline{H}^N(\theta) = \frac{1}{N}\left\{(N-1)\varepsilon(\theta) + \varepsilon\left(\theta + \frac{2\pi}{N}\right) - \sum_{j=2}^{N-1}(j-1)\delta^{(N,1)}\left(\theta + \frac{2\pi}{N}j\right)\right\} \tag{11}$$

Equations (9) and (11) represent the same thing, so the average can be described as follows:

$$\overline{H}^N(\theta) = \frac{1}{2}\{H^0(\theta) + H^1(\theta)\} + \frac{1}{2N}\left\{\sum_{j=1}^{N-1}(N-2j)\delta^{(N,1)}\left(\theta + \frac{2\pi}{N}j\right)\right\} \tag{12}$$

According to Eq. (12), the two neighboring sensors on a scale can generate calibration values that are the same as the case when the sensor heads are at equal intervals. This method allows for higher-order calibration with fewer sensor heads.

This principle enables calibration against any higher order by using only two sensor heads. However, an angle between two sensor head becomes narrow for calibration of higher order errors therefore the effect increases from an error at the installation of sensor heads at the ideal angle. In addition, the difference of accuracy curve among sensor heads remains small in case of narrower angle between two heads which inherit a slightly different error curve even by the detection over the same rotary encoder. Smaller difference in characteristics of error curve leads larger impacts on the calibration for higher order errors. It is critical to select the appropriate order for the calibration.

Authors have chosen self calibration with 3 pairs/ 6 heads based on VEDA method in consideration with these backgrounds. Each head locates at the position as a combination of three prime numbers of 2nd, 3rd and 5th order as shown in *FIGURE 1*. Errors from different orders are calibrated except multiple of 30th order as the least common value of these prime numbers. Fourier elements of an error from a scale is 0.003 arcsec or less for 25th or higher order as shown in *FIGURE 2.* and *FIGURE 3.*

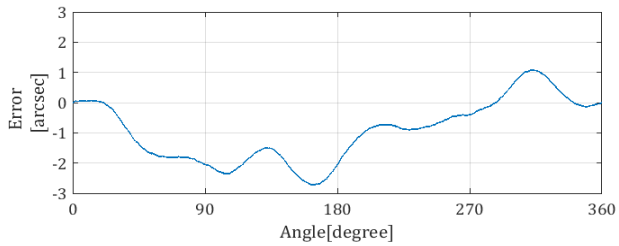

FIGURE 2. Example of error curve by one sensor head on the grating.

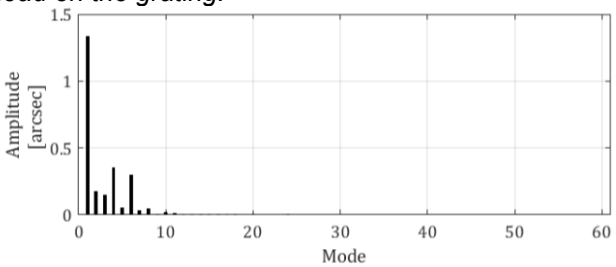

FIGURE 3. Example of Fourier components in error by one sensor head on the grating.

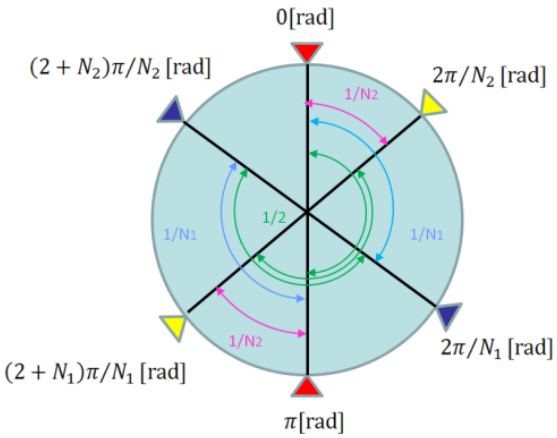

FIGURE 4. Location of three pairs (six units) of sensor heads facing each other.

Calibrated value at the 30th order satisfies target accuracy. Combination of 3 pairs from $N_1 = 2, N_2 = 3, N_3 = 5$ is ideal to keep calibration order N small for the 30th order calibration in order to make the distance between two sensor head wider for VEDA method. A pair of the head faces each other at 180-degree interval for the elimination of eccentricity to the axis direction for self-calibration, as shown in *FIGURE. 4*. Simple arithmetic operations can realize calculation of self-calibration values based on these principles.

CONFIGUREURATION OF SYSTEM

Developed Rotary encoder system consists of a rotary scale with grating, a sensor head unit with multiple sensor heads built inside of the unit to scan grating of a rotary scale, and data processing box containing a circuit to process analog signals from the sensor head unit and apply compensated value real time then output angular data, such as *FIGURE 5*. A rotary scale holds diffraction gratings on the glass disc with outer diameter of 90mm and inner diameter of 70mm. one μm pitch grating contains 2^{18} grating lines per 1 cycle. Sensor head uses grating interferometer method to detect gratings and output sinusoidal signal of 2^{20} per rotation, which is interpolated by 2^{16} through interpolation circuit to make resolution of 2^{36}.

Rotating table only needs to integrate a rotary scale with the weight around 270g so that the effect from the rotary encoder system to the rotation table remains significantly small during measurements. Sensor head unit weighs around 4kg but can be installed independently onto the fixed, non-moving part around a rotary table with flexible mounting options. The data processing box has the function to calculate the self-calibration value described in the previous section and calibrate the measured values in real time. These compact and flexible design for installation enables high accuracy rotation angle measurement on the process machine regardless of the mounting direction.

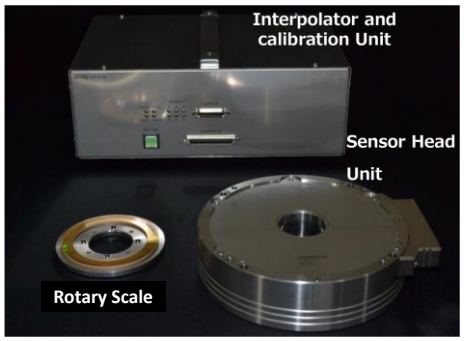

FIGURE 5. Rotary encoder system using VEDA method.

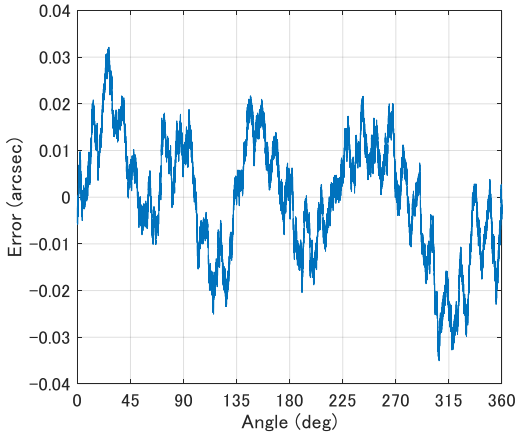

FIGURE 6. Error of the rotary encoder system

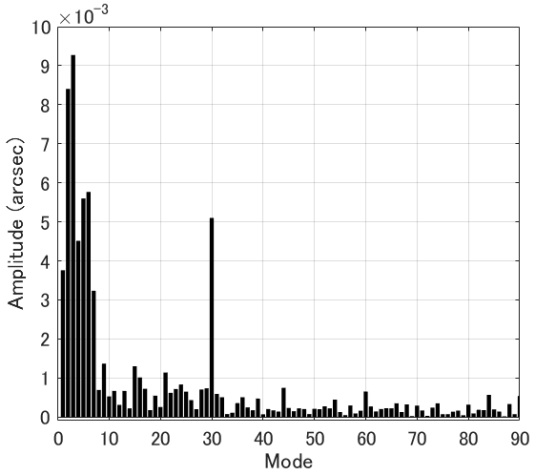

FIGURE 7. Fourier components in error of the rotary encoder system

EVALUATION OF DEVELOPED SYSTEM

The rotary encoder system was installed in a calibration device with traceability as part of the Japan Calibration Service System to the national standard for angles using the equally division average method [4] owned by the National Institute of Advanced Industrial Science and Technology (AIST), and the angle accuracy was verified. *FIGURE* 6 shows the results of accuracy measurements, with the error ± 0.03 arcsec. Large errors at low order, such as 1st 2nd and 4th order should originate from the characteristics of error curve of sensor heads. Errors at the multiple of 30th orders remained small around 0.005 arcsec. Errors from other higher order than 30th existed approximately at 0.01 arcsec.

CONCLUSION

A self-calibrating rotary encoder attached to a machine tool that can measure the positioning angle without contact with high accuracy and high reproducibility was developed. It provided accurate measurements even with a horizontal spindle, wherein it is difficult to guarantee accuracy and reproducibility. Further, as the resolution of the rotary encoder is higher than positioning resolution, even if measurement is performed at any position according to the positioning resolution of the spindle, accuracy can be measured with little influence by the short interval error of the rotary encoder using as a reference caused by the resolution and the interpolation.

REFERENCES

[1] Goch G, Knapp W, Hartig F. Precision Engineering for Wind Energy Systems. Annals of the CIRP. 2012; 61(2): 611-634.

[2] Aurich J C, Linke B, Hauschid M, Carrella M, Kirsch B. Sustainability of abrasive processes. Annals of the CIRP. 2013; 62: 653-672.

[3] Ishii N, Taniguchi K, Yamazaki K, Aoyama H. Super-Accurate Angular Encoder System with Multi-Detecting Heads Using VEDA Method. Journal of the Japan Society for Precision Engineering. 2018; 84: 717-723.

[4] Masuda T, Kajitani M. High accuracy calibration system for angular encoders, JRM, 1993; 5(2): 448-452.

COMPARISON OF AN ENCODER SYSTEM AND AUTOCOLLIMATOR FOR USE IN SI-TRACEABLE TORQUE MEASUREMENTS

Zane Comden[1], John Draganov[1], Stephan Schlamminger[1], Frank Seifert[2], David Newell[1], and Leon Chao[1]

[1]Quantum Measurement Division
National Institute of Standards and Technology
Gaithersburg, MD, USA

[2]Joint Quantum Institute
University of Maryland
College Park, MD, USA

INTRODUCTION

After approximately two and a half years, a team of researchers at the National Institute of Standards and Technology (NIST) in Gaithersburg, Maryland has completed and verfied the performance of an initial prototype torque calibration device utilizing a modification of the Kibble principle [1].

The torque generated by the Electronic NIST Torque Realizer (ENTR) is intended to be a realization of torque from traceable quantum electrical standards defined by the International System of Units (SI). Therefore, each measurement must be traceable to a standard defined by the SI. The four measurements of concern for a traceable torque realization in the desired fashion are voltage, current, and angular velocity (angular position and time). Voltage and current measurements are traceable via the calibrated voltmeter and resistor used in the data acquisition process, but the measurement of angular velocity in the calibration mode of ENTR must also be traceable to length standards defined by the SI. This can be achieved by physical length standard artifacts (such as a butterfly wheel) via comparison to an autocollimator.

While ENTR displays uncertainties within the bounds of the project goal, uncertainties of the encoder scale measurement in [1] are determined from reference documents of the encoder system. Proper alignment of the encoders to the scale was confirmed by utilizing an alignment device provided by the encoder manufacturer. This offers reasonable confidence in the accuracy and certainty of the angular position measurement, however, measurements taken by the encoder system are not calibrated until compared to some other traceable standard such as an autocollimator or an interferometer.

Details of the operational theory of ENTR including the definitions of “spin mode” and “torque mode” are beyond the scope of this paper, but are presented in [1] and [2]. Relevant to the topic at hand is the nature of the central rotor and the rotary encoder system.

This abstract will detail the experimental procedure and results of a comparison between angular measurements made using an autocollimator in conjunction with a 12-sided optical polygon and a dual readhead rotary encoder system in order to define the uncertainty of the encoder system with respect to an SI-traceable measurement.

ENTR’s primary mechanical components are a central rotor constrained by two ceramic bearings with the rotor’s axis of rotation oriented parallel to gravity, a cantilever holding the upper bearing, and a base plate with a recessed hole for location of the lower bearing. Two pieces of high-carbon steel (magnetic yokes) are mounted to the central rotor, and an assembly of NdFeB magnets are mounted upon the yokes. The lower yoke is machined with a mounting surface for a rotary encoder scale. A detailed rendering of the central rotor is shown in Figure 1.

When assembled, the central rotor is able to rotate freely, or be controlled to a desired angular position by driving a current throught the electromagnet constructed from stacked printed circuit boards (PCBs) within the air gap between the permanent magnets. A rendering of the fully assembled ENTR is shown in Figure 2, and we present further details of the construction in [1].

Note: Certain commercial equipment, instruments, and materials are identified in this article in order to specify the experimental procedure adequately. Such identification is not

intended to imply recommendation or endorsement by the NIST, nor is it intended to imply that the materials or equipment identified are necessarily the best available for the purpose

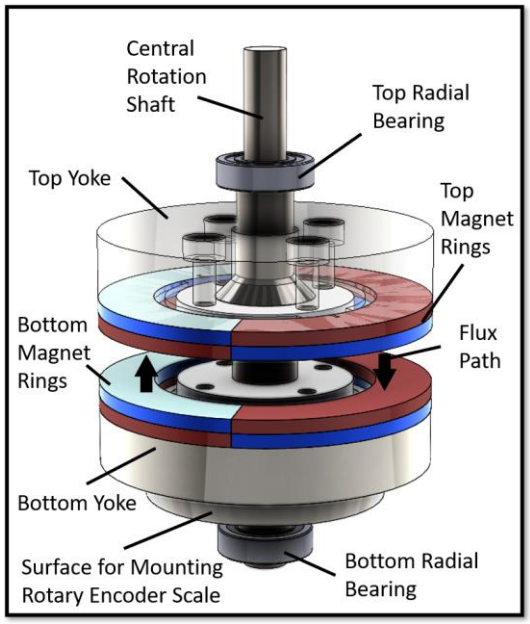

FIGURE 1: Rendering of the assembled central rotor. Magnetic poles of the permanent magnets are colored to indicate flux path direction. Encoder scale not shown, however the surface for mounting the encoder scale is indicated at the bottom of the image.

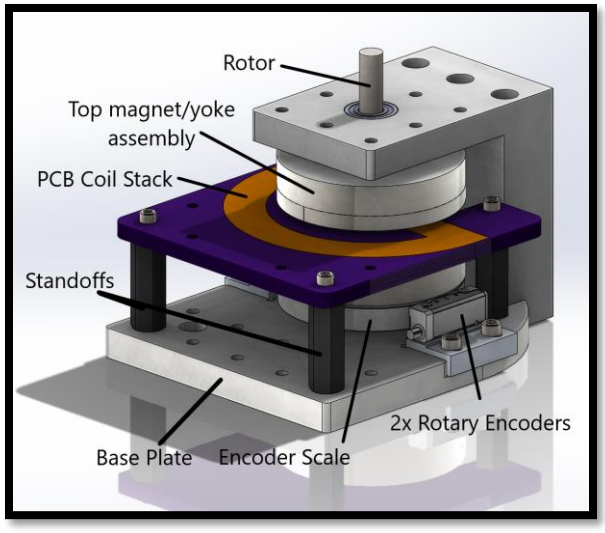

FIGURE 2: Three-Dimensional rendering of ENTR. The location of the encoder scale and rotary encoders can be seen towards the bottom of the image. The optical polygon is mounted at the top of the rotor.

EXPERIMENTAL SETUP

In order to determine the accuracy of the encoder system, we compare measurements between an Elcomat 3000 Autocollimator in combination with a 12-sided optical polygon and the installed Renishaw dual read-head rotary encoder system. The optical polygon is mounted to the top of the central rotor and aligned with the autocollimator such that readings can be acquired about the entire rotation. An effort is made to align the faces of the optical polygon with the encoder scale such that each face will provide a reading to the autocollimator while the encoder reads near an integer multiple of 30°.

ENTR is then set in torque mode, and the position control system is used to hold position at While the control system holds the rotor at the setpoint, measurements of the encoder and autocollimator reading are taken and recorded in tandem. The control system then rotates the shaft by 30° according to the encoder system, and the data collection process repeats. Due to the geometry of ENTR's electromagnet and permanent magnets, two of the 12 faces of the polygon do not have data associated with them. This is because ENTR cannot easily control the rotor in regions near 180° and 0° (360°).

The control system and feedback ensure that the standard deviation of the encoder readings is not more than 1 arc second during the acquisition of the autocollimator readings. Due to the large number of encoder readings taken for each autocollimator measurement, we choose to round the encoder reading values to the chosen set point. Therefore, the readings of the autocollimator represent the difference between the encoder reading and the angle of the rotor as measured by the autocollimator.

The data acquisition process is automated and the autocollimator data will only be recorded once the reported encoder values fall below a certain threshold standard deviation value, ensuring relatively low noise in the autocollimator signal and the encoder values.

One set of measurements (represented by the red crosses in Figure 3) is conducted with the two optical encoder signals combinded with a hardware device provided by the manufacturer. The other set of measurements presented (blue dots in Figure 3) were created by combining measurements from two subsets of measurments, each taken using only one of the

two encoders. The two encoders are defined as encoder A and encoder B. These data sub-sets are then manually combined via averaging to explore whether the hardware-based combining component provided by the manufacturer would perform significantly better than a simple arithmetic mean of the two encoder values from encoders A and B.

RESULTS

Uncertainty

The optical polygon used for the experiment has not been calibrated, but we assign an additional uncertainty to the values gathered by the autocollimator of +/-1 arcsecond, as this is generally a reasonable upper limit of uncertainty in angle between two adjacent faces of a steel-faced optical polygon [3]. The optical polygon used in this experiment is made of fused silica, which should hypothetically have better accuracy of angle between the faces, but we choose 1 arcsecond to be conservative.

This 1 arcsecond uncertainty is taken into account along with the number of autocollimator readings at each encoder position, and the standard deviation of the autocollimator measurements to give uncertainties shown by the error bars in Figure 3.

Results of the comparison experiment

We find that there is a difference between the angular position reported by the encoder system and the values measured by the autocollimator, as expected. This error manifests as a half sinusoid for the data taken by encoders A and B, and a full sinusoid in the autocollimator data as shown in Figure 5. The values reported by the autocollimator agree whether we used the hardware based combinator provided by the encoder manufacturer, or manually averaged the autocollimator values after taking separate data sets with each encoder.

Figure 3 shows data taken with encoder “A” while Figure 4 shows data taken with encoder “B”.

For the two datasets in which both encoder signals were combined (presented in Figure 5), we find that there is a maximum error in the encoder measurement of approximately +/- 20 arcseconds. We can apply this uncertainty to the encoder measurement for spin mode calibration in ENTR's intended operation.

In order to determine the relative error in the encoder measurement, we start by modeling the error detected by the autocollimator data as a sine wave and use the following equation:

$$\varphi_\varepsilon = \delta_\varphi \sin(\varphi + \alpha) \qquad (Eq.1)$$

Where φ_ε represents the error detected by the autocollimator and δ_φ is the maximum error detected. The angle α is a phase to refelct the position of the pattern. Taking the derivative of this equation with respect to time:

$$\dot{\varphi}_\varepsilon = \delta_\varphi \dot{\varphi} \cos(\varphi + \alpha) \qquad (Eq.2)$$

We choose to evaluate this expression at the location of maximum error $(\cos(\varphi + \alpha) = 1)$ so the equation becomes:

$$\dot{\varphi}_\varepsilon = \delta_\varphi \dot{\varphi} \qquad (Eq.3)$$

and rearranging this and subsituting δ_φ with 20 arcsec ~100 μrad yields

This analysis gives a relative uncertainty in the encoder measurement during ENTR’s spin mode of 100 parts in 10^6. For either of the individual encoders, the error is approximately 5 times larger.

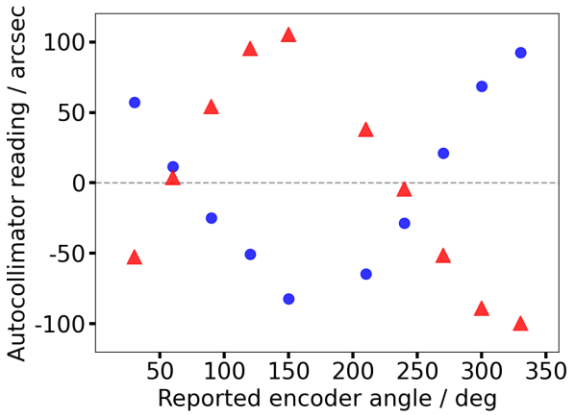

FIGURE 3. Data taken with individual encoders A and B plotted on the same axis. Red triangles represent encoder A while blue circles represent encoder B. The dashed horizontal line at y=0 is present for reference only. The eccentricity in the motion of the encoder scale is visible by the large range of the autocollimator data. Uncertainty bars are not shown. Each point has approximately 2

arcseconds of uncertainty in the autocollimator measurement.

DISCUSSION

The difference in the size of the error bars between the two datasets in Figure 3 is primarily due to the number of measurements taken at each position. The hardware combined dataset (red crosses) contains 48 or 49 autocollimator datapoints per encoder location. Meanwhile, the manually combined dataset (blue dots) only contains approximately 10 datapoints per encoder location.

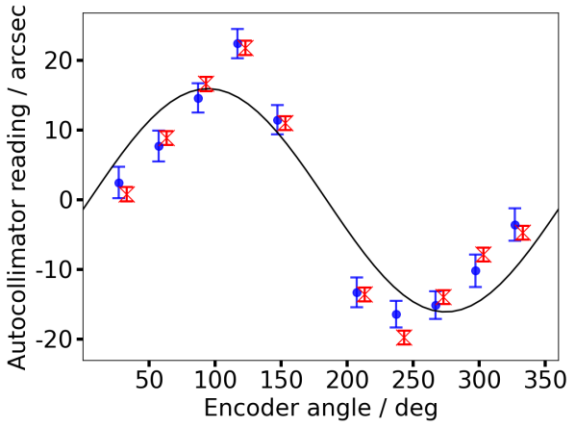

FIGURE 4. Results of the comparison between encoder measurements and autocollimator measurements for both experiments with autocollimator measurements taken every 30 degrees.. Blue circles are points combined manually via weighted analysis after data is taken using each of the two individual encoders, while red crosses represent data taken using the manufacturer-provided component which combines the two encoder signals at the hardware level before recording. A sin wave is fit to the harware combined dataset for comparison. The two sets of points are slightly offset from their true position in the x-axis for clarity. In reality, points were taken at the same x-axis locatons. Points are not present at 0, 180, or 360 degrees due to the construction of ENTR's electromagnet preventing control of the rotor at those angular positions.

Analysis of these results has influenced the design decisions of ENTR's successor device (ENTR_v2), with plans to expand the operational range of the ENTR project to 1 N m (approximately 142 ozf-in) of torque with a design overhaul.

We determine that it is best to continue development with a dual readhead encoder system in order to minimize any effects of scale eccentricity, which is very apparent before combining the datasets from each individual encoder (Fig. 3). The measured error of a single encoder is 5 times greater than the error measured for this combined encoder system. It is also desireable to continue using the encoder signal combination device provided by the manufacturer, primarily due to simplicity of the data acquisition system needing only one set of encoder signal inputs from the combination device, rather than a separate set of inputs from each encoder which will require more computational resources to analyze.

The relative encoder error determined in this…

REFERENCES

[1] Comden Z, et al., "The Design and Performance of an Electronic Torque Standard Directly Traceable to the Revised SI," in *IEEE Transactions on Instrumentation and Measurement*, vol. 72, pp. 1-6, 2023, Art no. 1005506, doi: 10.1109/TIM.2023.3279911

[2] Comden Z, et al. "Refining Measurements of an SI-Traceable Torque Self-Calibrating Electronic Torque Standard", American Society for Precision Engineering Conference Proceedings, 2022

[3] Indian Standards Institution, "Specification for Steel Precision Polygons", 1973, https://law.resource.org/pub/in/bis/S01/is.6987.1973.pdf

BEARING DESIGN CHOICES HAVE CONSEQUENCES: A CASE STUDY

Todd Noste[1], Laura Hopper[1], Jimmie Miller[1], and Chris Evans[1]
[1]Center for Precision Metrology,
University of North Carolina at Charlotte
Charlotte, NC, USA
**Now at Lawrence Livermore National Laboratory, USA*

Introduction

In 2016, UNCC/CPM received from Lawrence Livermore National Laboratory donation of a custom measuring machine based on the design of a commercially available diamond turning machine. Initially we planned to develop this machine as a flexible precision positioning system to support both fundamental precision machining research and, where needed, in-process form metrology including probe testing. Soon thereafter we observed growing activity in freeform optics[1]-[3], the emergence of the Center for Freeform Optics, and a growing naïve belief in process feedback based upon "on machine" measurements, where manufacturing and form metrology measurements potentially have common mode (and hence ignored) systematic errors [4]. Hence, we changed our focus to converting the donated machine into a system capable of providing independent form metrology to close the loop on freeform surface generation, initially targeting a series of three mirror anastigmatic telescopes (TMAs) [5].

The machine and bearing design choices had been made some years before it was delivered to UNCC. This paper discusses the consequences of those choices and our work to ameliorate them for the revised application. We present no "new" physics, but rather an example and validation of a statement made in class by S. Patterson [6]

"If a machine is not performing as expected, the problem is thermal. And once you have convinced yourself that it is not, you are wrong".

Thermal effects can be subtle, and sometimes run counter to conventional wisdom.

Brief description of machine as delivered

The machine was based on a granite "surface plate" supported by a frame with passive vibration isolation. Fig 1 shows the measuring machine, (referred to here as the 100 UMM), carriage orientation and coordinate system. A custom "tool post" is mounted on the B-axis using flexure based collets in kinematic locations enabling probe changes (including chromatic confocal, capacitance, and air bearing LVDT probes) without loss of coordinate systems. The results reported here were acquired using the chromatic confocal probes in a nulling mode to minimize errors due to non-linearity in the probe.

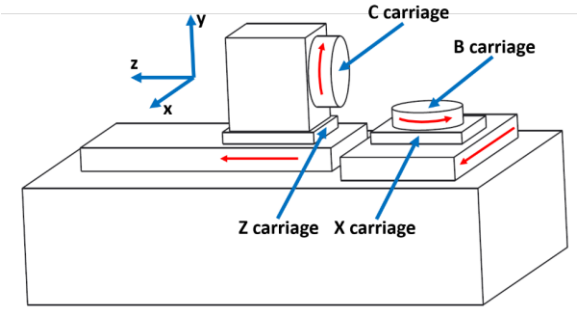

(a)

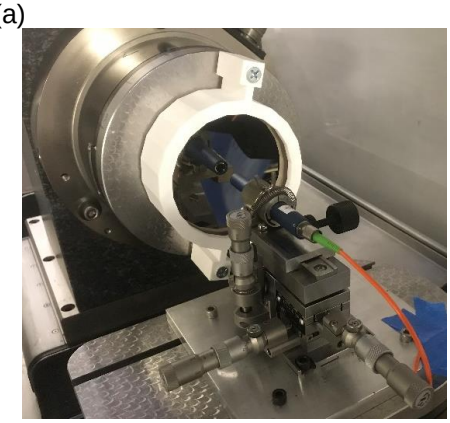

(b)

Figure 1(a) conceptual layout; (b) set-up for measurement of an approximately 90 mm clear aperture freeform mirror with a 3.6 mm sag.

Most of the supporting utilities (oil pump for hydrostatic bearings, etc.) were mounted directly

under the base. A “controls cabinet” is designed to be adjacent to one side of the machine. Under normal operation, the back panel (next to the machine) operates at approximately 35C, based on IR measurements, and couples directly into one side of the granite base. In addition, the control cabinet is asymmetrically located, preferentially coupling to the rear (+Z) of the granite table. These factors cause non-isothermal and non-equilibrium conditions in the machine frame and interwoven metrology loop causing variations in the physical state and resultant model of the machine. Subsequently as the X and Z carriages move in position they encounter and create differing thermal states.

Many of these issues were ameliorated in the enclosure design. A senior design team (7 seniors) was tasked with developing a thermal enclosure to control the machine metrology loop to 20 +/- 0.1C, following the teachings of Jim Bryan [7] wherein a precision machine can be located in a 20C enclosure separated from a “more comfortable” operator environment at greater than 20C. Bryan’s teaching is not wrong, but provides little detail about the isolation required to separate the “machine” from the external environment.

Bryan was a proponent of showering entire precision machines with large quantities of temperature-controlled fluid to minimize thermal errors. DTM3 used 1500 l/min of oil controlled to 0.0025 C [8,9]. Moore Special Tool developed a commercial oil shower system offered as an option on their M-18 Aspheric Generators. Developing such a system for the 100 UMM would have required significantly more effort than is reasonable for a senior design team.

The UMM100, as delivered to UNCC, is limited by a variety of stationary heat sources with time varying heat loads and moving heat sources with different thermal time constants.

The pressurized oil supplied to the hydrostatic bearings (X,Z) from the pump/reservoir located below the granite delivers oil at 2C above reservoir and air ambient. This heating in the hydrostatic pump introduces a temperature gradient in the X and Z ways and hence into granite. This latter effect has a long thermal time constant.

Both linear axes carry encoded rotary tables (C and B axes) based on Professional Instruments “4 inch” air bearings. As described below, the optimized tool path for the target TMA components used low speed rotational scanning of the C axis (1 rpm). Hence the C-axis contributes essentially no heat load from shearing air within the bearing, low power dissipation in the drive, and a constant, slow moving contribution from Joule Thompson cooling at the bearing exhausts.

Thermal contributions from the B axis depend on the part to be measured and the target uncertainty. The chromatic confocal sensor (most commonly used) has a non-linearity as a function of illumination angle. This can be corrected to the limit imposed by the uncertainty in the calibration. The B axis is only used in a stepping mode when required by the part prescription. For the measurement of relatively low slope optics, the B axis contributes slow moving Joule Thompson cooling and a small servo motor load.

Enclosure design

The enclosure design is relatively conventional [10], using a mixture of “solid” expanded polystyrene insulated walls, polycarbonate solid windows, and PVC strip walls. Polycarbonate and PVC strip walls have previously been shown to have a low transmission in the IR, while allowing visual “buddy system” safety protocols. These features reduce, but do not eliminate, IR coupling between the laboratory and the UMM 100.

Recirculating air, with 10% make up, is cooled via a water-to-air heat exchanger to below 20 C, reheated based on thermistor feedback from a location close to the work zone, and fed through an insulated plenum to provide down flow over the machine. Long term air temperature stability is better than +/- 0.1C. Return air is pulled from below the granite, giving a flow at approximately 20C to reduce the effect of heat sources from the utilities.

The machine and enclosure are in a laboratory that holds +/- 1C with a “bang-bang” controller, resulting in a saw tooth room temperature with a cycle time of several hours.

Drift

After commissioning the enclosure, a drift test with the structural loop closed along the z-axis

showed a saw tooth at the same frequency as the lab temperature with a small phase lag. This launched a search for coupling mechanisms.

High pressure air is supplied to the filters and desiccant drier (immediately outside the enclosure) via copper pipe at close to ceiling level. Hot air rises, heating the high pressure air supply. A 15 m coil of fine copper tube was added in the controlled temperature return under the granite between the desiccant tower and the 19 liter tank that provides air damping and mixing.

Metal-coated Mylar was added to reduce IR coupling from the room to the plenum above the machine and elsewhere. Efforts were made to reduce mixing of lab air and enclosure air. Coupling was reduced, but not eliminated (Figure 2) and the dominant sources became those associated with slide motions.

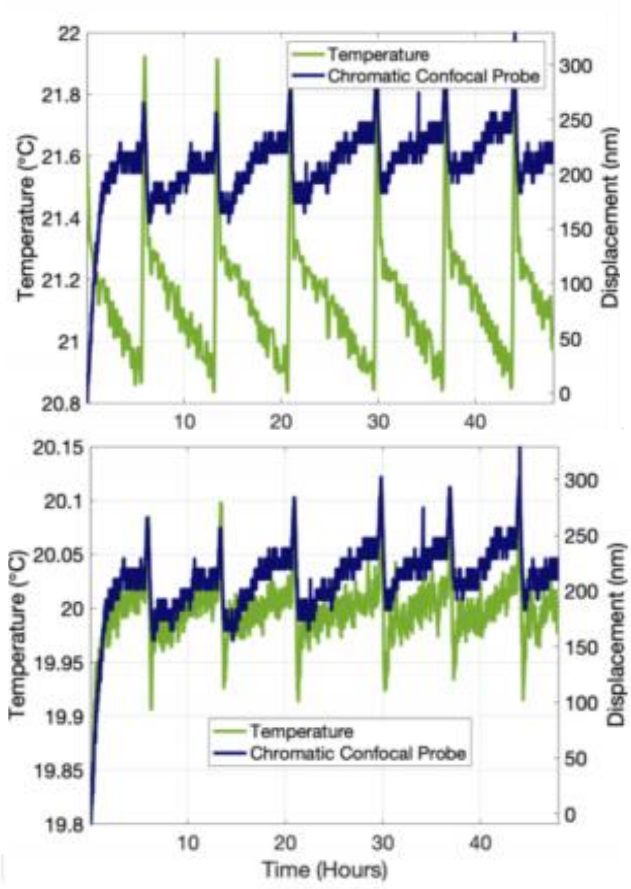

Figure 2: Test results: showing relationship between probe output and laboratory temperature(top) and enclosure temperature (bottom). Note the difference in Y axes [11]

Drift testing used a Precitec chromatic confocal probe measuring from the B carriage to the C carriage while recording the temperature inside and outside of the enclosure (Figure 2). Note that the probe reading and the enclosure temperature are directly correlated, and the relationship between the probe and the lab temperature anti-correlated. The rapid transient in temperatures and drift suggested one amelioration strategy. Note that probe output (+/- 50 nm) correlates with enclosure temperature. Hence if part measurement time is less than the cycle time of the lab temperature controller and the start time appropriately selected, the effect of lab temperature variation can be substantially reduced, and easily compensated.

Further investigation into thermal drift led to the hydrostatic oil system on the 100UMM [12]. When the X carriage was sitting in a position for an extended period, then moved, the carriage would drift, most notably in the pitch error motion. After measuring the oil temperature exiting the gap between the bearing and machine ways, a ~ 1 ^{o}C differential was found. This led to a system to control the temperature of the hydrostatic oil using the chilled water to cool the oil and a resistive heater to re-heat the oil. Like the air temperature in the enclosure, it is easier and faster to heat oil than to cool.

To further characterize heating in the hydrostatic oil, the influence of the oil going from 250 psig to atmospheric pressure was calculated. Following [13], A temperature rise of 1.1 C was found. The outlet temperature of the hydrostatic bearing was set to 20C when stationary. This system also accounted for an increase in oil temperature by hydraulic pump and the proximity of the oil tank to heat sources. These observations suggest that, with sufficient data, probe compensation based on the position histories of the linear axes could reduce the measurement uncertainty.

As noted above, the linear slides compound the effect of the oil supply temperature with the temperature rise of the oil due to viscous shear of the oil, flow rate and pressure drop. Reducing oil outlet temperature from the slides when stationary to 20C changes the local temperature gradient but does not eliminate it. The system can never be considered at steady state, at least during and for some period after slideway motion

Moving the slides results in changing temperature gradients in the metrology loop from constant

Joule Thompson cooling at the air bearing exhausts and power dissipation in all 4 axes. These effects were minimized by reducing the movement of the carriages that had the most thermal drift (X carriage) and maximizing movement in the carriages with the least thermal drift (C carriage). Compensation for these residual drifts is based on optimizing probe paths with redundant data. For short times between repeat visits to nominally the same position, the thermal drifts can be linearized and compensated.

To reduce environmental thermal effects shown above, the overall measurement time was minimized. Using the machine model and several minimization algorithms, for example the travelling salesman problem, the measurement time was reduced significantly. Probe paths were evaluated for total measurement time and movement of machine carriages to find the optimum path. The optimized probe paths were best suited for generating a measurement with equal data spacing in a grid over the surface of the part where the machine would move and stop at each measurement point This approach was driven, mainly by the part specification. Optical design for the target parts is based on, inter alia, a Zernike polynomial expansion to describe the azimuthally varying surface departure from a best fit asphere. Zernikes are orthogonal over a unit circle with uniform data spacing.

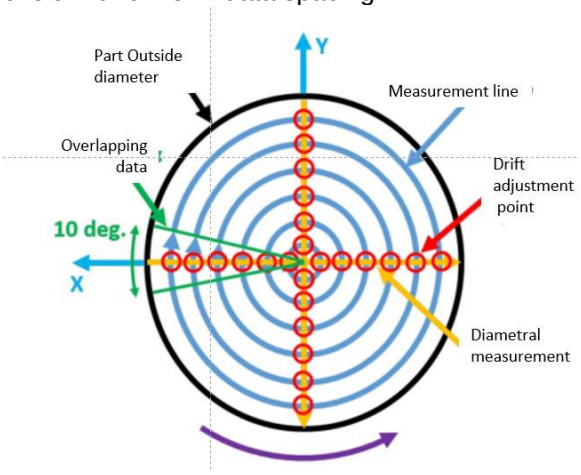

Figure 3: Data acquisition strategy

Converting to scanning data acquisition reduced measurement time significantly and enabled compensation for drift.(Figure 3.), but added an orthogonalization step to the data analysis. Two diametral traces are taken using the x-axis with the c-axis clocking between them. Next a series of azimuthal traces of increasing radius are recorded with the C-axis rotating at 1 rev/min and with a 10 degree region where the start and finish overlap. Drift over 62 seconds can be linearized to match start and finish. Next, each azimuthal trace has 4 common points with the diametral traces, allowing an over constrained solution for 3 rigid body compensations, tip, tilt and piston.

Data age

While a scanning measurement pattern (as opposed to “step and settle” approach) is beneficial for thermal drift compensation, it brings another bias, in the form of data age and another uncertainty contribution from variation in data age[11]. This data age arises from the machine controller architecture which only allows serial reporting of axis position and probe readout; each axis and the probe are interrogated sequentially at a chosen frequency. This means that some lag has occurred between the time the first axis readout occurred and the next, but they are still associated with same time step. Data age in this machine can be evaluated by a simple experiment using a stationary probe and a single moving axis. In one example experiment, the chromatic confocal probe sat stationary in the kinematic tool post while a flat was moved closer to and further away from the probe in Z within the probe’s measurement range. The difference between the recorded Z carriage position and the measured probe position was recorded as shown in Figure 4 at multiple feed rates. We observe a relatively linear increase in data age error with feed rate, as expected.

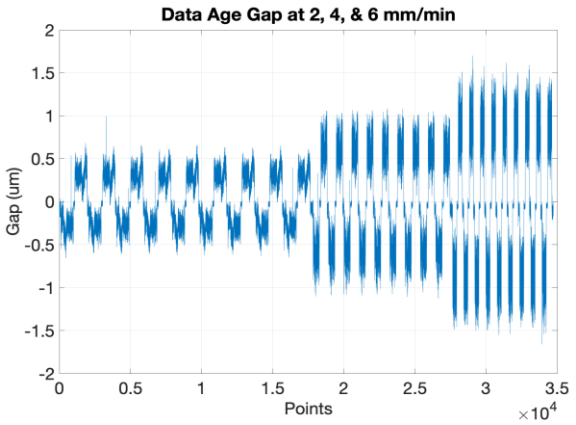

Figure 4: Data age as a function of slide speed

Note that compensation for data age and evaluation of data age uncertainty is relatively straightforward for one moving axis at constant velocity; compensation efforts are complicated by changes in acceleration and multiple moving axes.

used in the machine model for compensation, but the uncertainty arising for different x-travels and different “thermal soak out” procedures is not accounted for. A similar limitation applies to most of the machine tool metrology used.

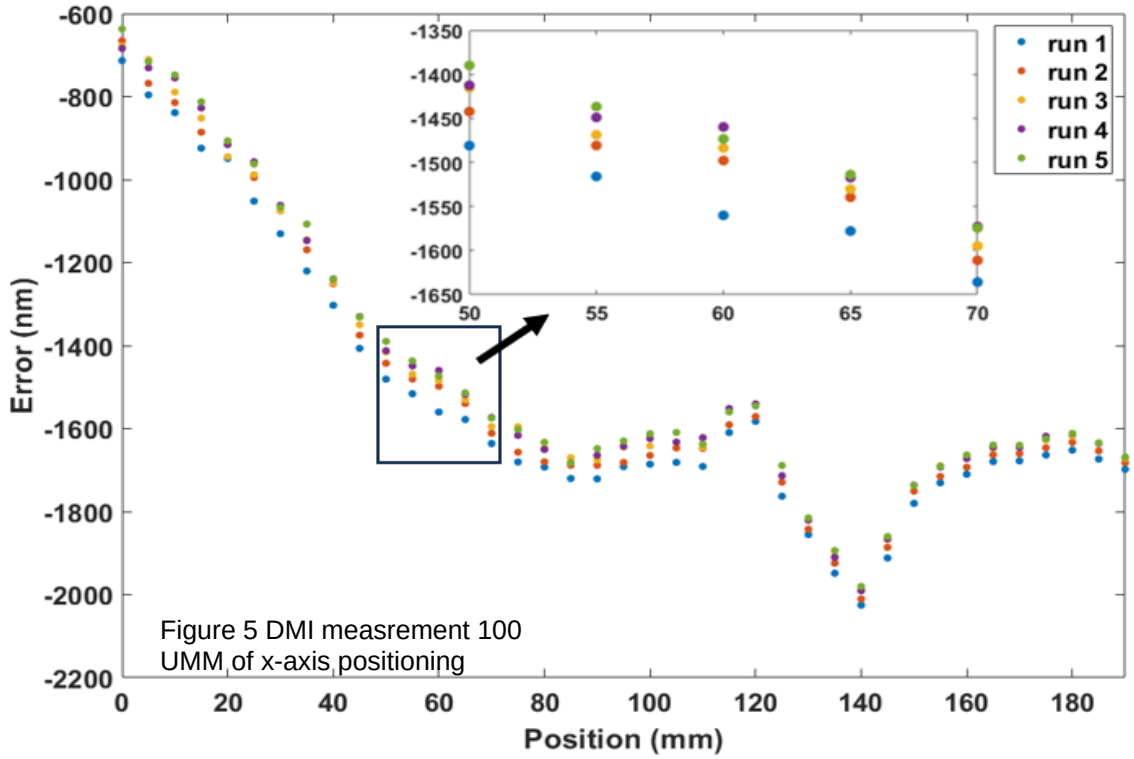

Figure 5 DMI measrement 100 UMM of x-axis positioning

Effects in machine calibration

It should come as no surprise that the influences discussed in the previous sections also affect our ability to generate a machine model that can be relied on to compensate error motions in the machine.

Figure 5 shows the result of serial repeat measurements of X-axis position using a displacement measuring interferometer (DMI) over 190 mm of travel This data is for “return” travel from X= 190 mm to X=0 in 5 mm increments. The UMM was stationary at each point for 8s, taking 3s to move between points. The refractive index of air was corrected using Edlen’s equation.

The difference between consecutive passes decreases suggesting a stabilization of the thermal gradients in the carriage. At the same time, this opens a can of worms. The DMI data is

Concluding remarks

General purpose metrology methods allowing closed loop control of fabrication processes for a variety of freeform optics are evolving but are not yet mature. In this paper we have identified some thermal limitations in repurposing a manufacturing machine for this task.

Bearings and related positioning stages provide axes of motion for mechanical systems. They influence and react to the total system state. Whitehead [14] states that "errors fall into two classes, those that only have to be recognized in order that they may be effectively eliminated and; and those errors that determine the accuracy… some errors can be removed from the second class by skillful design, but never all...”. It has been shown that air and hydrostatic bearings thermally influence and react to the total system thermal state in ways that are not inconsequential and can easily overshadow the

prismatic errors of slideways. Methods of mitigation of those errors have also been described. **To restate the main point the system can never be considered at steady state at least during and for some period after slideway motion".**

Acknowledgements

The authors acknowledge helpful discussions and support provided by Kevin Lawton, Steve Patterson, Ed Morse, Brian Dutterer, Greg Caskey,and Nick Horvath. The Senior Design team (Michael Erickson, Carson Hannah, Adam Mills, Seth Allgood, Justin Tedder, Austin Greeson, Alex Goncharov, and Ryan Margosian) exceed all expections, and did not exceed the project budget, which was expected.

Lawrence Livermore National Laboratory donated the 100 UMM.

This work was partially supported by the National Science Foundation I/UCRC Center for Freeform Optics (IIP- 1338877, IIP-1338898, IIP-1822049 and IIP-1822026), the UNC Charlotte Center for Precision Metrology, and the CPM Industrial Affiliates.

References

[1] Rolland, J. P., Davies, M.A., Suleski, T.A., Evans, C.,Aaron Bauer,A.,Lambropoulos, J.C., and Falaggis, K., "Freeform optics for imaging," Optica 8, 161-176 (2021)

[2] Horvath, N. Concurrent engineering of a next-generation freeform telescope: mechanical design and manufacture. SPIE Defense + Commercial Sensing. Advanced Optics for Imaging Applications: UV through LWIR IV, 2019.

[3] Noste, T. Concurrent engineering of a next-generation freeform telescope: metrology and test. SPIE Defense + Commercial Sensing. Advanced Optics for Imaging Applications: UV through LWIR IV, 2019.

[4]. Venditti, K., Evans C., Falaggis K,. Blum, A Chaudhuri R., J. Goodsell, and J. P. Rolland, “Design for metrology for freeform optics manufacturing,” Procedia CIRP 84, 169–172 (2019).

[5] Horvath, N.W, Barron, .I. W., Owen, J. D. Dutterer, B.S.,Schiesser, E., A. Bauer, A., J. P. Rolland, J.P,Davies, M.A, “Optomechanical design and fabrication of a snap together freeform TMA telescope,” in Proc. ASPE 32nd Annual Meeting (2017), pp. 133–138

[6] Patterson, S. “Precision machine design using LODTM as an example” MEGR 3090-090, Feb 2016.

[7] Bryan, J. International status of thermal error research. (1990) Annals of CIRP, Vol 39-2, pp645-656

[8] Bryan J.B. Design and construction of an 84 inch ultrprecision diamond turning machine. Precision Engineering(1979) **1**,1 pp13-17

[10] Hansen, H. Techniques for precision air temperature control. Proc. SPIE 0433 - Contemporary Methods of Optical Manufacturing and Testing, 1983.

[11] Hopper L., Noste, T., Miller, J. Evans, C. Error sources, compensation, and probe path optimization for on-machine metrology of freeform optics. Proc. SPIE 11487, Optical Manufacturing and Testing XIII, 1148709 (20 August 2020)

[12] Noste T. PhD dissertation ‘Freeform Optical Surface Form Metrology with Serial Data Acquisition’, UNC Charlotte, 2020

[13] Rowe, W. B. Hydrostatic, Aerostatic and Hybrid Bearing Design. Butterworth-Heinemann 2012.

[14] A dictionary of applied. Physics. Vol. III., Meteorology, Metrology and Measuring Apparatus. Edited by Sir Richard Glazebrook, F.R.S. In five volumes. London (Macmillan and Co.), 1983. 8°. Pp. vii + 839. 63s. net

Potential influence of linear hydrostatic bearing preload method upon carriage averaging

Mark A Stocker
Grinding-Ultra Precision division R&D
Cranfield Precision, Division of Fives Landis Ltd
Kempston, Bedfordshire UK

INTRODUCTION

Fluid film bearings have many, well documented advantages over mechanical, rolling element bearings. One of the primary advantages is the ability to provide excellent averaging, improving the moving carriage accuracy relative to the intrinsic accuracy of the bearing rails. However, if bearing averaging is to be maximized, particular attention must be given to the anticipated bearing rail geometric errors and the method of bearing pre-load being deployed. Failure to do so, can lead to error magnification, rather than error reduction by averaging.

BEARING AVERAGING

The principle of bearing averaging is quite simple. Essentially, bearing carriage averaging ranges from single point contact, rigid body motion with no avaraging, to fluid film (effectively infinite points of contact), elastically averaged motion.

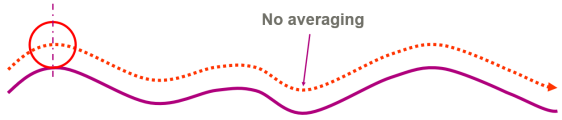

FIGURE 1. Single roller, rigid body, following the form error of the bearing rail: Minimal averaging.

A simple rolling element bearing roller will follow the form error of the bearing rail, providing little or no averaging.

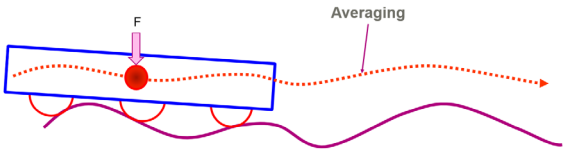

FIGURE 2. Multiple rollers, mounted in rigid carriage: Averaging introduced.

Introducing multiple rollers into a rigid carriage, will provide some averaging, but not all of the rollers will take equal loading and the level of averaging provided is very difficult to predict.

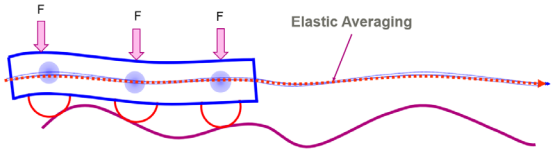

FIGURE 3. Multiple rollers, mounted in elastically deformable carriage: Increased averaging.

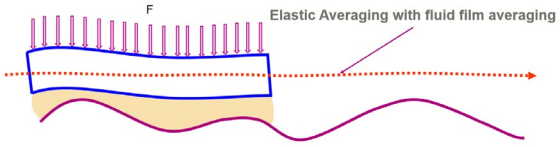

FIGURE 4. Fluid film bearing, elastically deformable carriage: Maximum averaging.

The ultimate bearing averaging is provided by fluid film bearings with elastically deformable carriage.

BEARING PRELOAD

Figures 1 to 4 show very simple configurations where the pre-load is effectively provided by carriage mass alone. Three methods of bearing preload are typically used: 1) Fixed, opposed bearing pads, 2) Floating opposed bearing pads and 3) Magnetic attraction preload. Each of these preload methods will produce different averaging and carriage error motion outcomes. Option 1 is the most difficult to implement and is usually the most costly. Options 2 and 3 are more forgiving of manufacturing errors, particularly in bearing rail parallelism, but must be used with caution.

A recent example of how a fixed preload bearing pads can enable the best possible bearing averaging is a large Off Axis Grinding machine produced at Cranfield Precision.

The machine bed is around 4 m long. The bearing rails are clamped to the machine bed. Bearing rails' straightness is optimized by hand scraping

the interface between the bearing rail and the machine bed. Each time the bearing rail is re-clamped to the bed, the straightness of the top of the bearing rail is re-checked and if necessary the bed re-scraped. This scraping procedure, cannot however, remove the effects of parallelism errors in the bearing rail itself. This is where the choice of bearing pre-load becomes critical.

FIGURE 5. Large grinding machine with 1.5 m long carriage

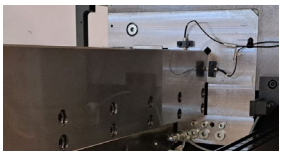

FIGURE 6. Fixed bearing pre-load pad configuration

This bearing configuration with fixed pre-load pads enables a good prediction of carriage error motions resulting from the beneficial effects of averaging.

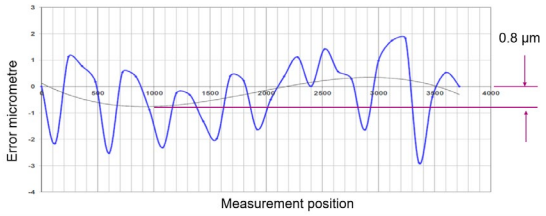

FIGURE 7. Bearing rail (top surface) straightness (blue) and predicted carriage motion with averaging (black)

The bearing rail straightness error was around 5 µm PV. However, drawing a best fit line through the plot, estimates that with optimum averaging, the carriage error motion should be <1 mm, which was indeed the case with this machine.

However, bearing rails with sinusoidal waviness errors can occur commonly when using conventional machining methods. The errors may only be a few µm in amplitude, but can result in significant angular and/or displacement errors in the machine carriage if not fully understood when choosing the bearing preload method.

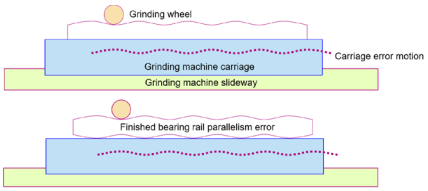

FIGURE 7. Common cause of sinusoidal bearing rail parallelism errors

Rails with this form of error, can still be effectively averaged using fixed pad pre-load pads.

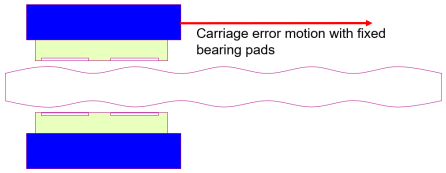

FIGURE 8. Theoretical averaging effect of fixed pre-load pad bearings with sinusoidal rail errors

Fixed pre-load pads offer the best possible averaging over this kind of bearing rail error.

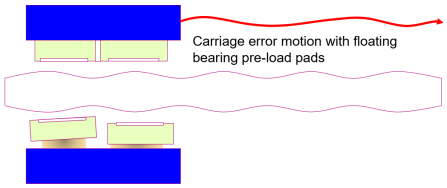

FIGURE 9. Less predictable, averaging errors with floating bearing pre-load pads.

There are other bearing rail form errors that can best be compensated for using floating pads or magnetic pre-load. Once the form of bearing rail geometry error is known, it is possible to select the optimum bed scraping and bearing preload pad combination. For example, scraping the bed/rail interface to ensure the rail top surface is straight, becoming the master surface, enabling the floating preload pads to follow the profile of the underside of the bearing rail, and not contribute to the error motions of the carriage.

Is summary, there are many configurations of bearing, pre-load, and rail alignment strategy. Each has to be thoroughly understood to avoid the possibility of assuming that fluid film bearings provide ‘good averaging’ regardless of how configured. It is a false assumption and can lead to significant issues if not thoroughly appreciated.

Externall Pressurized Porous Gas Bearings for sCO2 Turbomachinery

Andrew D. Devitt[1], Jeremy W. Rainey[1]
[1]Reseach and Development
New Way Air Bearings
Aston, Pennsylvania, USA

Theory, Experimental Description, Results, and Implications for Machine Design

A Turbo Alternator Compressor (TAC) in a supercritical CO2 power loop at Sandia National Laboratories has been retrofit with Externally Pressurized Porous (EPP) gas bearings.

EPP Gas Bearings, a type of aerostatic bearing, are shown to offer the load capacity of oil bearings, the zero friction of magnetic bearings, and the simplicity of foil bearings. The main advantage is spring from the fact that the gas that is being processed is also being used as the bearing fluid. So, there is no need to keep separation. In fact, the high pressure in the bearing gap can be used as a seal dam, for instance to keep low or negative pressure in the PMG cavity to minimize windage losses there.

Because the thrust bearing can also be the seal and the balance piston the rotor length can be dramatically reduced. Because the gas bearings can handle higher surface speed, larger diameter rotors can be used. This combination of shorter more rigid rotors reduces rotor dynamic problems. In this case, because it was a retrofit the same diameter and length rotor was used. But, because of the high load capacity available through the external pressurization, the thrust bearing architecture is reversed 180 degrees, meaning that all the thrust bearing area is at a smaller diameter than the major diameter of the rotor. This reduces the maximum surface speed from the previous design at 399 meters per second to 167 meters per second in our retrofit design, while demonstrating 10 times the axial load capacity of the previous design.

Another advantage is that the EPP bearings have is high temperature capability, the Graphite used in these test bearings can operate at 500c continuously. The next generation of EPP bearings made from CMC have been fired at 850c and are expected to be able to operate at 850c temperature. Being able to put the bearings where the work is being done, that is directly on or very near to the impellers, means that tip clearances, that typically need to be built in between the impeller and the stator because of thermal growth from the thrust bearing or rotor dynamic motions of the cantilevered impeller, can be dramatically reduced. This is a very important efficiency point and becomes ever more important as the impeller size gets smaller, the impeller speed gets faster and the pressures get higher. Yet another efficiency advantage comes from elimination of oil shear losses. If a 100MW system losses 3 percent to sheer loss, oil cooling and pumping, almost 3MW would be saved by EPP gas bearings.

And that's not all, all the required damping for the rotor is done in the gas bearing gap. There is no damper cartridge with flexures, there are no O rings, foils, bumps, or springs supporting the bearings. It is a very simple clean design, and we were able to demonstrate adjustable stiffness and damping by adjusting the input pressure to the bearings.

In summary the authors believe that the testing that has been done in a separate test fixture, and in an actual TAC at the Sandia National laboratory's supercritical CO2 test loop. show that the externally pressurized porous gas bearings tested provide a promising path forward for bearings and seals in future supercritical CO2 power cycles

Effect of recess area on the performance of a precision hydrostatic spindle with mid-thrust bearing

Chenggang Fang[1] and Dehong Huo[2]
[1] School of Mechanical and Power Engineering, Nanjing Tech University
Nanjing, Jiangsu, China
[2] School of Engineering, Newcastle University
Newcastle upon Tyne, UK

ABSTRACT
The paper investigates the effect of recess area on the dynamic and static performance of a precision hydrostatic spindle with mid-thrust bearing. The hydrostatic governing model of the coupled journal and thrust bearings with four recesses is established; the distribution functions of steady and transient pressure fields are solved by the mathematical perturbation method; and the influence of different recess area on bearing capacity, stiffness, and damping is further analyzed. To improve the computational efficiency, a decoupling algorithm based on the linear superposition principle is employed to solve the steady and transient pressure distribution function, and flowrate continuity equations. The simulation results show that the recess area has a significant influence on the dynamic and static performance of the hydrostatic spindle.

INTRODUCTION
A high precision hydrostatic spindle can maintain the floating state no matter in static or rotating state, which has the characteristics of high precision, high stiffness, large damping, wear free, etc., and is usually used in precision turning, milling, and grinding processes. For the multi-recess precision hydrostatic spindle with external oil supply, the dynamic and static characteristics of the spindle can be optimized by adjusting various design parameters, including oil supply pressure, oil film clearance, bearing geometric parameters, recess parameters, etc. [1]. In terms of recess parameters, many scholars have studied the influence of the shape, structure, area, quantity, and depth of recess on the bearing performance.

However, most of the previous researches focused on the influence of oil recess geometric parameters on the temperature rise, stability, and bearing capacity of sliding bearing, while fewer studied on the impact of oil recess area coupled with the operating parameters of the five degree-of-freedom hydrostatic spindle rotor on the dynamic and static characteristics, imbalance response, and stability of the spindle.

THE HYDROSTATIC SPINDLE
The schematic view of the spindle structure studied in this paper is shown in Fig. 1, which is composed of the spindle rotor and bearing housing. The spindle bearings are constituted of a pair of bilateral symmetrical journal bearings and a pair of bilateral thrust bearings, which forms a middle thrust bearing structure and improves the radial stiffness of the spindle end face. The bearing surfaces of the journal and thrust bearing are arranged along the circumferential direction with four uniform rectangular pressure oil recesses, to ensure the spindle has sufficient stiffness and rotary precision no matter in the static or rotating state. All 16 recessess are pressurized with oil externally, and the pressure in recesses are compensated through the orifice restrictor to obtain the best stiffness value.

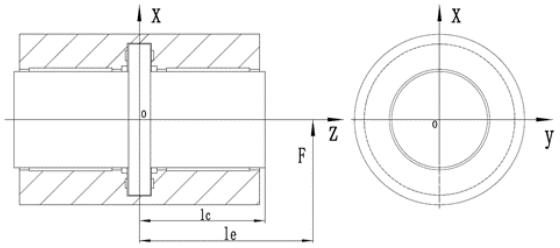

Fig. 1. The schematic view of the hydrostatic spindle with mid-thrust bearing

SIMULATION MODEL
When the spindle rotor is in the state of high-speed rotation, the film land area has a distinct influence on the strength of dynamic pressure because of the wedging and squeezing effect. The pressure distribution function inside the oil film is obtained directly from solving the Reynolds equation to calculate the dynamic and static characteristics of the spindle accurately. The mathematical perturbation method and linear superposition method are employed to solve the transient Reynolds equation to obtain the pressure distribution function of the flow field

under the different combinations of recess area and spindle operating parameters. Finite difference method (FDM) is chosen to solve paritial differential equations due to its simple programming and high calculation accuracy. In this coupled journal and thrust bearing model, oil film thickness and pressure changes are modelled as the function of five degree-of-freedom displacement of the centre of the spindle rotor, i.e. translantional displacements (*Δx, Δy, Δz*) and tilt displacements ($\Delta\theta_x$, $\Delta\theta_y$). Detailed governing equations and oil film pressure distribution solving methods can be found in [2-3].

The parameters of the coupled journal and thrust bearing of the spindle are summarized in Tables 1, 2, and 3, respectively.

Table 1. The specifications of the spindle

Parameter name	Value
Rated speed (rpm)	3000
Max speed (rpm)	4800
Rated cutting force(N)	2000
Max cutting force(N))	4000
Rated power (kW)	3
Mass of rotor (kg)	15
Oil supply pressure (MPa)	4
Viscosity (Pa·s)	0.002
Oil supply temperature (℃)	20

Table 2. Parameters of the journal bearing

Parameter name	Value
Orifice restrictor diameter (mm)	0.2-0.5
Oil film thickness (mm)	0.016
Diameter (mm)	90
Length (mm)	90

Table 3. Parameters of the thrust bearing

Parameter name	Value
Orifice restrictor diameter (mm)	0.4-0.7
Oil film thickness (mm)	0.016
Inner diameter R1 (mm)	37
Outer diameter R4 (mm)	70

For the convenience of calculation, the recess's edges are selected along with the circumferential and axial grids, and the recess area is shown as table 4. Besides, the film land resistance varies as the recess area changes, which will cause the pressure ratio λ_0 to deviate from the optimal value. To maintain constant λ_0 under different recess areas, the diameter of the orifice restrictor is usually corrected using the method introduced in [4].

Table 4. Simulation parameters

Num	Area(mm^2)	Orifice diameter (mm)
1	288 (24x12)	0.2
2	864 (36x24)	0.245
3	1728 (48x36)	0.29
4	2880 (60x48)	0.355
5	4320 (72x60)	0.475

RESULTS AND DISCUSSION

Athough there is a coupling effect between the journal and thrust bearings. The results and the trend for of both bearings are very similar. This section only reports the simulation results for journal bearing.

Static Characteristics Versus Recess Area

Since it is not convenient to describe rotor eccentricity in the five degree-of-freedom space, relative eccentricity ε_e defined as the relative displacement of the center point on the spindle end face:

$$\varepsilon_e = \frac{\sqrt{(\Delta x + l_c \cdot \Delta\theta_y)^2 + (\Delta y - l_c \cdot \Delta\theta_x)^2}}{C_0} \quad (1)$$

where l_c is the distance of the spindle's end face to the center of the rotor (see Fig. 1). Δx, Δy, $\Delta\theta_x$, $\Delta\theta_y$ are the displacement components of the rotor, and C_0 is the nominal oil film thickness.

Fig. 2 shows the relationship between the recess area and relative eccentricity, and flowrate under different loads when the spindle is at the rated speed of 3000 rpm. It can be found from Fig. 2(a) that when the recess area is less than 1800 mm^2, the bearing capacity of the spindle decreases rapidly with the increase of the recess area. When the recess area is higher than in 1800 mm^2, the bearing capacity of the spindle starts to rise slowly. Fig. 2(b) shows that the total flowrate of the spindle increases rapidly with the increase of recess area, and the correlation with external load is weak.

Fig. 3 shows the relationship between the recess area and relative eccentricity ratio, and flowrate, at different rotating speeds when the spindle load is 2000 N. Fig. 3(a) illustrates that when the recess area is less than 1800 mm^2, the bearing capacity of the spindle increases significantly with the increase of spindle speed, which is mainly due to the massive dynamic pressure formed by the spindle rotor when rotating at high speed. When the recess area is higher than 1800 mm^2,

the dynamic pressure formed by the spindle rotation will decrease due to the decrement in the film land field, while the static force acted on the rotor by recess pressure will increase. Therefore, the bearing capacity of the spindle increases slowly with the further increase of the recess area, and the correlation of it with spindle speed is weak. Fig. 3(b) reflects the relationship between the total flowrate of the spindle and the variation of the recess area, which shows that the variation trend is the same as that in Fig. 2(b).

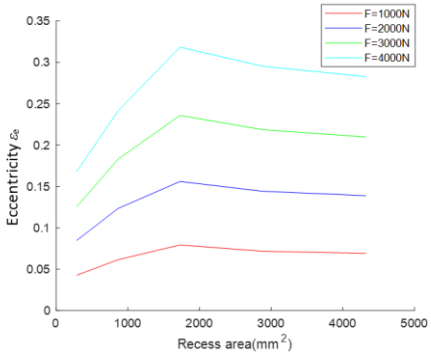

(a)

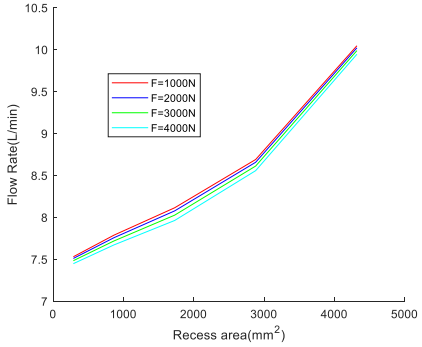

(b)

Fig. 2 Spindle load capacity and flowrate versus recess area under different loads

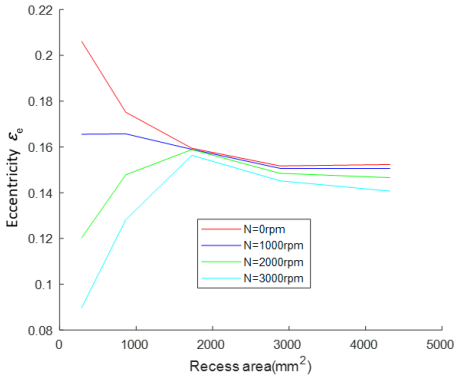

(a)

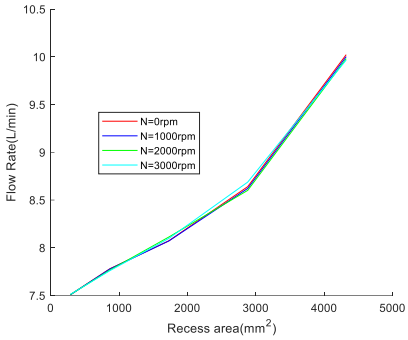

(b)

Fig. 3 Spindle load capacity and flowrate versus recess area at different rotational speeds

Dynamic Characteristics Under Concentric State

For studying the relationship between the recess area and the spindle performance comprehensively, different load and speed combinations are selected; and the relationship between the recess area and the bearing pressure distribution, stiffness, and damping, is obtained through computer simulation to guide the spindle design. The simulation parameters are as follows: external load F = 0, rotor angular frequcncy ω = 50*2π (rad/s), and the spindle rotor is under concentric state.

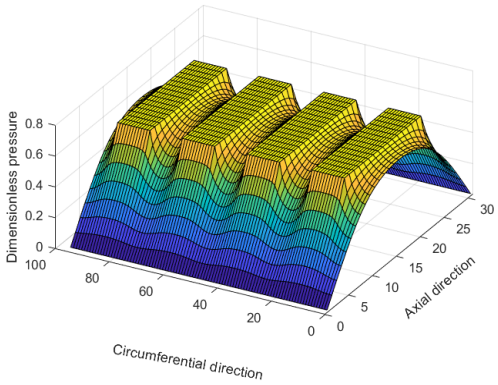

(a)

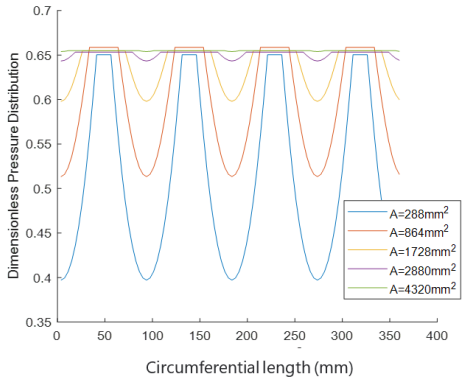

(b)

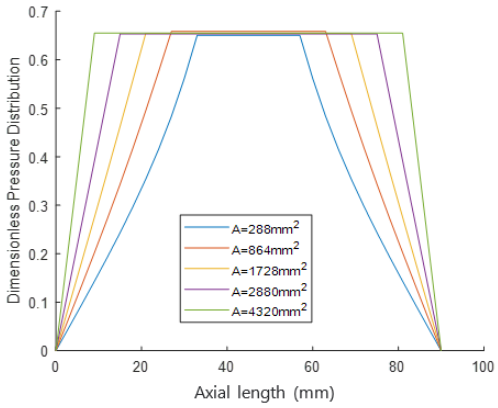

(c)

Fig. 4. Circumferential and longitudinal pressure profile of the journal bearing under concentric state

Fig. 4 shows the pressure distribution of the journal bearing with different recess areas, and that of the thrust bearing is similar. When the rotor is under concentric state, the dimensionless pressure of each recess is shown in Fig. 4(a) of which is equal to the design pressure ratio of 0.65. Fig. 4(b) shows that due to the change of liquid film resistance with the variation of the recess area, the pressure distribution amplitude of film land in the circumferential direction is proportional to the recess area. Fig. 4(c) shows that the pressure distribution gradient of the longitudinal film land is proportional to the recess area.

The details of stiffness and damping coeffcients that are used to decribe the dynamics characteristics can be found in [2]. Figs. 5(a) indicate the relationship between the principal stiffness coefficients K_{xx}, k_{yy}, the cross stiffness coefficients K_{xy}, K_{yx}, and the recess area. The principal stiffness coefficients increase slightly with the rise of the recess area in the beginning, then they almost keep constant after the recess area reaches 2800 mm^2. Besides, the cross stiffness coefficients k_{xy}, K_{yx} vary significantly with the change of recess area. Concretely, the absolute value of cross stiffness coefficients decreases rapidly with the increase of recess area when the recess area is relatively small; while the recess area reaches 2800 mm^2, the above coefficients cross the zero point and increase reversely. Furthermore, the variation of the recess area of journal bearing plays a small role in the stiffness coefficients associated with the z-axis. Other principal stiffness coefficients $K_{\theta_x\theta_x}$, $K_{\theta_y\theta_y}$ and cross stiffness coefficients $K_{\theta_x\theta_y}$, $K_{\theta_y\theta_x}$ follow the same trend.

Figs. 5(b) indicate that the principal damping coefficient C_{xx},C_{yy},decrease 60% by approximate linear rule with the increase of recess area because the damping of film land in the bearing is much higher than that of recess. principal damping coefficient $C_{\theta_x\theta_x}$, $C_{\theta_y\theta_y}$ follow the same relationship. Other cross damping coefficients are not affected obviously by the variation of the recess area.

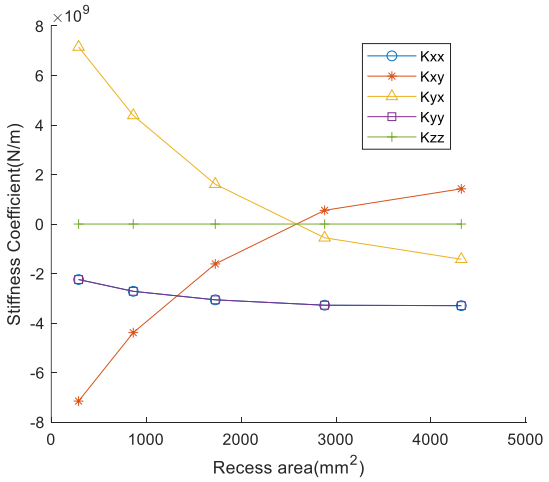

(a)

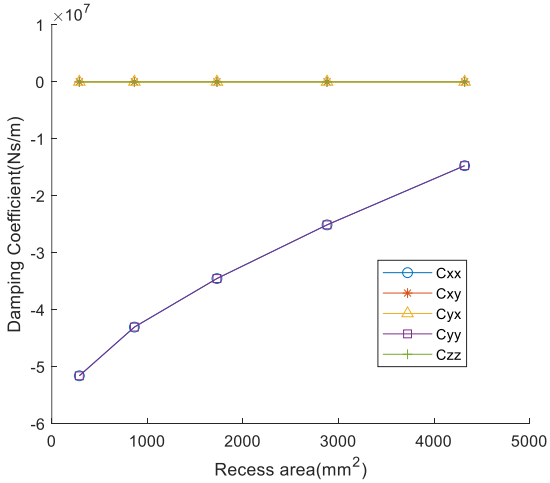

(b)

Fig. 5. Stiffness and damping coefficients versus recess area under concentric state

Dynamic characteristics under eccentric condition

For comprehensively comparing the spindle performance under eccentric condition, the simulation parameters are selected as follows:

rated cutting load is 2000 N; the operating distance of cutting force l_e=250 mm (see Fig. 1), and other simulation parameters are the same as before.

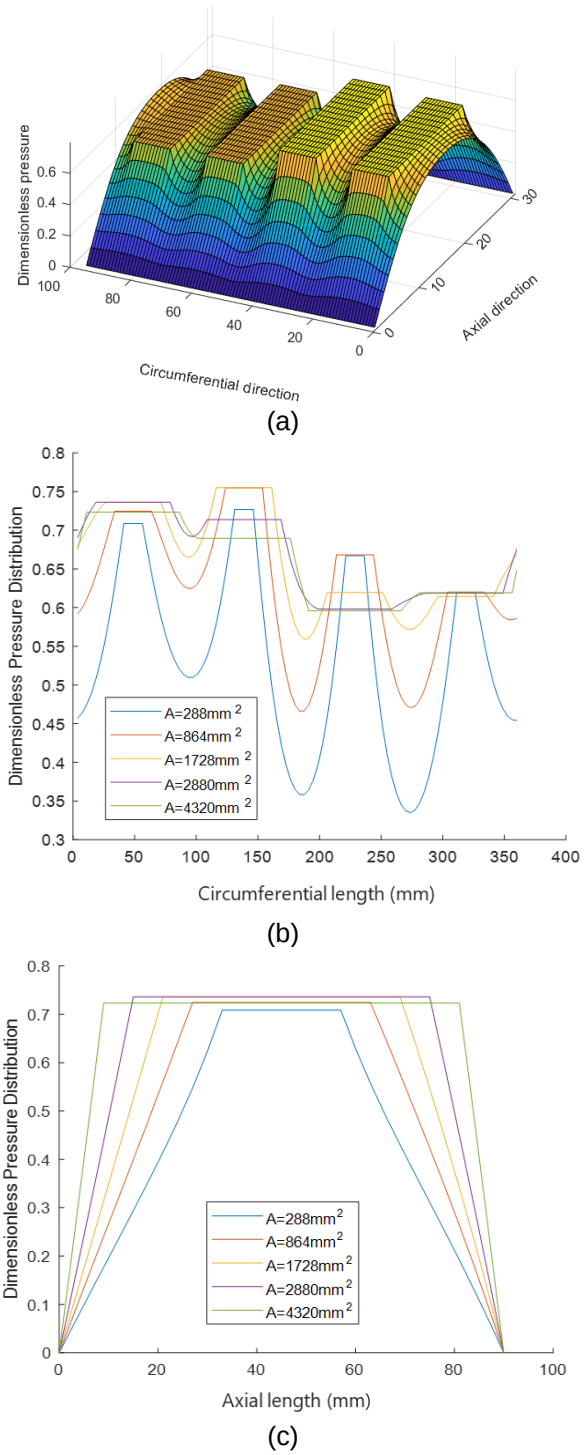

Fig. 6. Circumferential and longitudinal pressure profile of the journal bearing under eccentric condition

Fig. 6(a) depicts the 3D pressure distribution of oil film under the eccentric state, which also reveals that the dimensionless pressure in each recess does not equal the design pressure ratio of 0.65. Specifically, Fig. 6(b) shows that when the spindle rotor is eccentric under rated cutting load, the dimensionless pressure of each recess changes from designed value to form a resultant force against external load, and the pressure distribution value of film land increases with the rise of the recess area. Fig. 6(c) shows that the longitudinal pressure distribution of an eccentric rotor is basically the same as that of a concentric rotor.

Fig. 7 shows the relationship between the dynamic characteristics of the spindle and recess area under eccentric state. It can be found that the variation trend of force stiffness coefficients due to translation (Fig. 7(a)), force damping coefficients due to translation (Fig. 7(b)), is basically the same as that of the corresponding dynamic coefficients in Fig. 5, which illustrates that the effect of recess area on dynamic coefficients is similar under the concentric or eccentric state. Moment stiffness coefficients due to tilt motion and moment damping coefficients due to tilt motion are also obtained, and they also follow the same trend. Therefore the effect of recess area on dynamic coefficients is similar under the concentric or eccentric state.

Figs. 7(c) shows that when the oil recess area is small, the cross stiffness associated with coordinates is not zero. However, with the increase of the oil recess area, the above stiffness coefficient decreases rapidly to around zero, which indicates that when the oil recess area increases to a certain extent, its change has little influence on the cross stiffness coefficient of the spindle. Figs. 7(d) shows that when the oil recess area varies from small to large, various cross damping coefficients change enormously, which depends on the working conditions of the spindle. As the oil recess area further increases, the damping coefficients gradually approaches zero. The above analysis results show that compared with the oil recess area, the area of the film land has a tremendous influence on the spindle characteristics. Therefore, with the increase of the oil recess area, the sensitivity of spindle characteristics with the change of the oil recess area decreases.

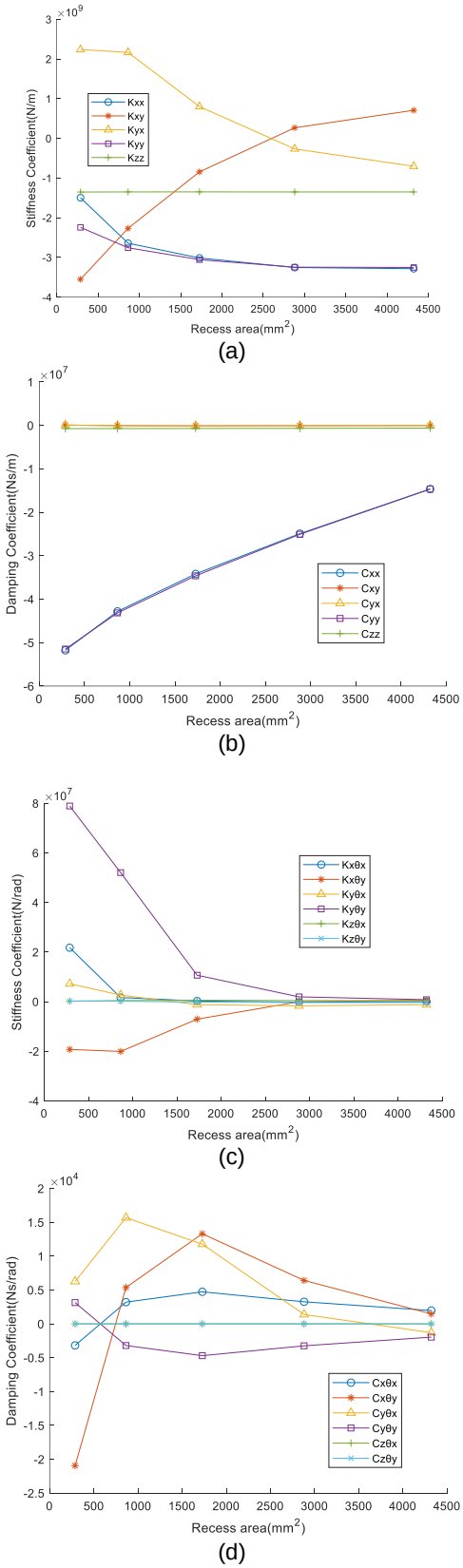

Fig. 7. Stiffness and damping coefficients versus recess area under eccentric condition

CONCLUSIONS

Under different relative eccentricities and rotating speed of the spindle, the smaller recess area has a significant impact on the bearing capacity. When the recess area increases to a certain extent, the bearing capacity is almost independent of the recess area.

When the spindle is within the range of operating load, the stiffness and damping coefficients of the spindle will decrease with the increase of recess area, except the principal stiffness and damping.

When the primary size of the spindle bearing is determined, the recess area can be optimized according to the design requirements of the spindle to obtain the required performance parameters such as stiffness, damping, and rotary accuracy.

The hydrostatic spindles have been prototyped and the experimental validation is on going. More comprehensive analysis will be reported in another publication.

REFERENCES

[1] Z. Liu, *et. al*. A review of hydrostatic bearing system: Researches and applications. Advances in Mechanical Engineering 2017; Vol. 9(10) 1–27.

[2] C. Fang, D. Huo and X. Huang, A comprehensive analysis of factors affecting the accuracy of the precision hydrostatic spindle with mid-thrust bearing layout, International Journal of Advanced Manufacturing Technology, 2021, 114 (3), 949-967

[3] C. Fang, W. You, and D. Huo. Investigations of the static and dynamic characteristics of the precision hydrostatic spindle with mid-thrust bearing under different loads. Proceedings of the Institution of Mechanical Engineers, Part J: Journal of Engineering Tribology. 2022, 236 (4):732-747.

[4] Y. Chen. Principle and design of hydrostatic bearing. National defense industry Press; 1980.p.119.

HOW TO CONTROL TEMPERATURE: IT'S NOT THAT HARD

Dan E. Luttrell
Kriterion, LLC
Milford, Connecticut, USA

ABSTRACT
"Everything, before it is anything else, is a thermometer"[1]. All machines and instruments respond to temperature variations and often in very complex ways over time. Equipment can be designed and controlled to minimize thermal effects. But the simplest and most cost-effective approach is to control temperatures within and around the equipment.

Four basic approaches to address thermal effects will be discussed and critiqued. Static and dynamic effects of temperature variation on precision equipment are described. Control of temperature will be shown with examples of systems and enclosures developed over the last several years. A summary of key experiences will be presented.

WHY CONTROL TEMPERATURE?
Requirements for precision equipment continue to evolve. New capabilities and increased performance of products with precision components have continued to push requirements for precision machines and instruments.

In addition to tighter tolerances, some equipment requirements are driven by processes that have longer time frames. Larger parts with precision tolerances lead to longer process times. The need to make a larger number of a particular component also leads to longer process times.

As these precision requirements continue to evolve, the materials used to construct precision equipment are the same. Therefore, the importance of temperature continues to increase.

DESIGN FOR THERMAL EFFECTS
There are four basic approaches to dealing with thermal effects [2].

1. Choose design concepts less sensitive to thermal change,
2. Use materials insensitive to thermal changes,
3. Measure thermal state and compensate with control system,
4. Control the environment and energy flow to minimize thermal effect.

The first two are design tasks. Examples of the first approach would be athermalization, shielding, symmetry, and smaller structural loops. Application of precision design principles is critical for the success of precision equipment. Choosing materials less sensitive to thermal effects may be required in some designs. Example materials would be Invar, Zerodur, and ULE (Ultra Low Expansion glass). There is an increased cost to using these materials that must be considered, and this often makes them impractical.

The last two approaches are control tasks. Measuring temperatures in and around a machine to determine a compensation position for the axes has been done [3-6]. The complexity has limited its use in practice. However, advances in neural networks and availability of new software tools may enable this approach to become more practical.

Controlling temperatures in and around precision machines and instruments is still the most practical and cost-effective way to manage thermal effects. It directly addresses the root cause of the problem. Typically, air is used to maintain temperature around equipment. Air shower systems can achieve thermal stability of ±0.01°C [7]. Oil has been used when requirements call for tighter thermal stability [8].

Water and oil are often used to maintain temperatures within a system and to remove excess energy. This is a focused use of fluid for energy removal. Examples would be the direct, or focused, cooling of bearings and motors that create excess heat.

THERMAL DYNAMICS CAN BE COMPLEX
The thermal state of a system depends on its thermal history. This includes the thermal history of the surrounding environment and the energy flow in and out of a system. Instruments and machines are comprised of many components of various shapes and sizes and made from a variety of materials. This means components and sub-assemblies respond differently over time to changes in temperature.

It's not enough to only think about thermal expansion of materials in the static sense. It's also important to consider the effects of thermal conductivity (or thermal diffusivity). This time dependent effect leads to what can be called "Thermal Dynamics," which describes displacement changes in a system as a result of its thermal history.

The thermal response of components and subassemblies can be visually characterized using the amplitude portion of a Bode plot as shown in Figure 1.

Starting with 1 Hz on the far right, the time period increases to the left. This plot extends from 1 second (1 Hz) to about 24 hours (~11.6e-6 Hz). A normalized displacement is shown on the vertical axis.

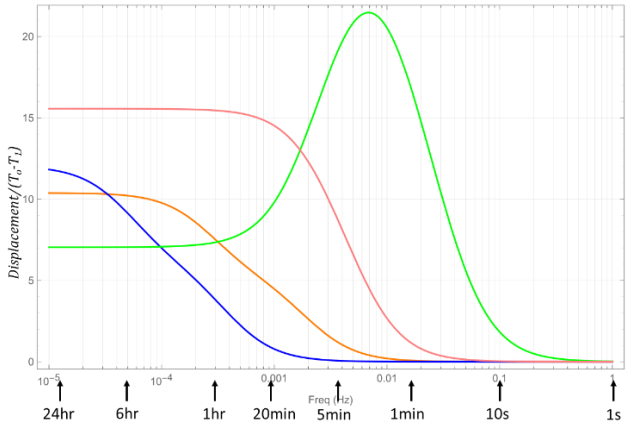

FIGURE 1. Thermal effects in the frequency domain.

The plots shown are examples of typical components to illustrate the basic idea. The slower responding plots represent larger components and components with lower thermal conductivity. This response has been referred to in the past as “Thermal Inertia” [8]. The plots with larger displacement at the left represent parts with higher thermal expansion. It’s important to note that air temperature variation of typical HVAC systems oscillate a few degrees with a period of about 15 – 20 minutes.

The plot showing an initial larger displacement and then a decrease with time represents a subassembly with materials that change size at different rates and perhaps different directions. Figure 2 shows an example of this from tests on an early diamond turning machine. This plot shows axial growth of the spindle with a 1°F step change in temperature of an oil shower that covered the entire machine. After an initial growth of about 2 microns, the displacement decreased, but not all the way back to its starting point. This is still a typical response on modern machines.

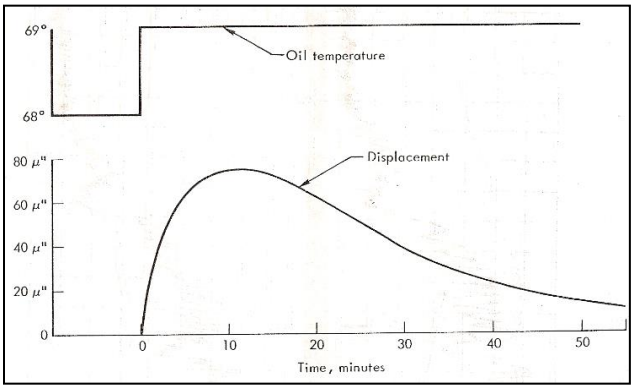

FIGURE 2. Thermal effects as a function of time measured on an early DTM with oil shower [8].

It’s important to realize that, unlike these simplified example plots, real systems have thermal displacements in all three dimensions. Also, thermal displacements often lead to unwanted rotation of components. Then, of course, there could be thermal gradients that further complicate the situation.

The more complex the equipment, the more complex the thermal response, especially if cycling several times per hour. This is why measuring temperatures and compensating displacements is difficult. At this point in time, controlling the environment and energy flow is a much more practical, reliable, and cost-effective approach.

PRECISION TEMPERATURE CONTROL

There are a few things that must be considered for precision temperature control of fluids:

1. High sensitivity, fast response temperature measurement,
2. Fast actuator response time,
3. Cascaded control loops,
4. Manage secondary disturbances.

Thermistors are used for temperature measurement because of their high sensitivity. Also, their small size results in fast response times. Only when temperature change is sensed quickly can a control system command a respond quickly. Thermistors are also reliable and stable over a long period of time [9].

It is important that the way a fluid temperature is changed, or actuated, results in it occuriing quickly when commanded. For example, a damper that mixes air flows of different temperatures can change position within a few seconds and quickly change the resulting temperature. On the other hand, a resistive heater in an airstream may take many 10s of seconds or longer to change the resulting air stream temperature.

A cascaded control loop is one with a secondary loop inside a primary control loop. For example, a primary control loop would measure the final temperature of a fluid before contacting the equipment. The deviation of that temperature would control the set point of a secondary, faster control loop that would be at the source of the temperature-controlled fluid. This would adjust for heat gains or losses in the ducting and air distribution setup. It also allows gains in the secondary loop to be increased since there is less transport delay between the actuator and the sensor.

Typical disturbances come from people, lighting, and room variations. These must be minimized or shielded. If facility chill water is used for system heat removal (which is common for larger systems), the variations in temperature and pressure of the chill water must be managed. This is easiest done by

creating a secondary chill water loop to create a thermal buffer. Experience has shown that facility chill water can vary as much as ±3°C (±5°F) and ±20 psi.

Most precision temperature control systems are set to maintain a temperature of 20°C. This is because the standard reference temperature for geometrical product specification is set at 20°C by the standard ISO 1:2002(E).

SOME BASIC HEAT TRANSFER CONCEPTS

Thermal control system capacities can be estimated starting with basic heat transfer concepts. In terms of heat flow and mass flow,

$$\dot{Q} = \dot{m} c_P \Delta T \quad (1)$$

where $\dot{Q}$ is energy flow (J/s), $\dot{m}$ is mass flow (g/s), c_P is the heat capacity of the material (J/(g-°K)), and ΔT is temperature change (°K). For air flow, the relationship between temperature change and power required, in commonly used units, is:

$$\dot{Q}_{\text{air}}\ (\text{Watt}) = (0.573)\ \{\text{air flow(cfm)}\}\ \Delta T\ (^{\circ}C) \quad (2)$$

One thing to realize is that air is an insulator, which means that it does not absorb energy very well compared to other fluids. This is seen in the heat capacity value. The volumetric heat capacity for air is $C_{p,v}$ = 0.001297 (J/cm^3-°K). For water, $C_{p,v}$ = 4.179 (J/cm^3-°K). This is why water is often used for cooling systems. Air is not an efficient fluid for temperature control, but its ease of use often outweighs the lack of efficiency.

One other heat load to consider, especially for larger rooms, is the heat added to the air by the fan. In terms of air flow (cfm) and back pressure ("w.c.)

$$\dot{Q}_{air,f}(\text{Watts}) = (0.508)[\text{air flow(cfm)}]\Delta P(\text{"w.c.}) \quad (3)$$

The lack of thermal efficiency in air has led to the to the use of liquids for some systems. When requirements dictate thermal stability less than about ±0.02°C, a liquid with higher heat capacity should be considered. For machines this is typically oil. Water is often incompatible with materials in the system. Heat capacity of oil is on the order of $C_{p,v}$ = 1.7 (J/cm^3-°K), which is still several orders of magnitude greater than air.

EXAMPLES OF AIR SUPPLY SYSTEMS

One method of controlling air temperature around a machine is to blow temperature-controlled air into an enclosure that surrounds the machine. Typically, air is drawn in from the surrounding room, cooled or heated as needed, and then blown into the enclosure at the desired temperature. After passing through the enclosure, the air flows back into the room. This is known as a non-recirculating, or open loop, air shower.

This type of system has the advantage that it does not require collecting air from the enclosure and routing it back to the air supply with return ducting. Figures 3 and 4 show examples of this type of system.

FIGURE 3. Non-Recirculating Air Shower on a Freeform Measurement Machine.

Typically, there are three ways to cool the air flow in any type of system. One is to use a standard refrigerant system (evaporative cooling) like that in a standard air conditioner. The second is to use solid-state Thermo-Electric Cooling (TEC) elements. The third way is to use chilled water either from a facility chill water system or a dedicated chiller. All of these have been used successfully. It's important to work with the key precision temperature control principles with any of these systems.

FIGURE 4. Non-Recirculating Air Shower on a Diamond Turning Machine.

A standard refrigerant system can have a much larger cooling capacity than a TEC system. TEC systems, like those shown in Figures 3 and 4, can have up to 1.5 kW of cooling capacity (about 5,000 Btu/h or 0.4 Tons of refrigeration). By comparison, window air conditioners for the home can have more than triple this cooling (up to 18,000 Btu/h).

A rule of thumb for air flow to be most effective through a temperature-controlled enclosure is 1 to 3 air changes per minute. Knowing how much the air temperature needs to be lowered and the volumetric air flow (cfm), eq. (2) can be used to estimate the maximum cooling capacity needed.

Cooling air can be expensive. For example, a TEC system requires about 2 kW of power to achieve 1 kW of cooling. Two things can be done to minimize operating cost. First, insulate the enclosure and ductwork to reduce power loss. This also will reduce temperature variations due to fluctuations in surrounding room temperature. This should always be done. Second, recirculate the air so that ΔT requirement is kept to a minimum. Returning air will likely have less temperature difference to overcome than the surrounding room air.

Figures 5, 6 and 7 show a relatively large recirculating air system [10]. The room houses a large CMM and is 17' x 15' x 14'h (3,570 ft^3). The air supply was set up for 4,000 cfm which is about 1 air change per minute. This was sufficient because the room is very well insulated (4" walls) and all the ductwork was well insulated as seen in Figure 7. This is an example where air is flowing through a room horizontally. As an example of heat added by a fan, with 4,000 cfm and a typical 0.5 "w.c. back pressure, the added heat is about 1 kW.

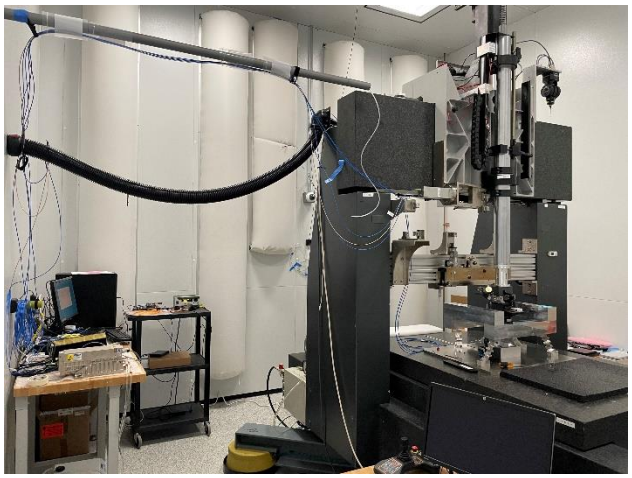

FIGURE 5. Flexible supply ducts for a recirculating air system with horizontal air flow over a large CMM.

The decision of whether air should flow from top-to-bottom, or side-to-side, or even bottom-to-top, depends on what's in the room and how it will be used. In most cases, air flow from top-to-bottom is sufficient. From a practical perspective, it is the simplest design and easiest to build.

FIGURE 6. Return vents for a recirculating air system with horizontal air flow.

FIGURE 7. Insulated return ducts for a recirculating air system with horizontal air flow.

AN OIL SHOWER EXAMPLE

When requirements dictate thermal stability less than about ±0.02°C., an oil shower should be considered. Many have been built over the years and have proven to be very effective. A food grade mineral oil has been used successfully. It is easier to dispose of and doesn't irritate the skin as some machine oils do. The downside is that oil systems require pumps, plumbing, reservoirs, and filtering. These can be very messy systems. That's one trade-off for achieving less thermal variation.

Figure 8 shows one of the first oil shower systems built on a precision machine tool. This was in the late 1960s. It is an early diamond turning machine built on a Moore #3 base with a double hemisphere porous graphite spindle. Thermal stability was <±0.01°F (<±0.0056°C). It was able to hold a static position

stability between the tool and workpiece in the axial direction <5 nm over many hours. This was quite remarkable at the time.

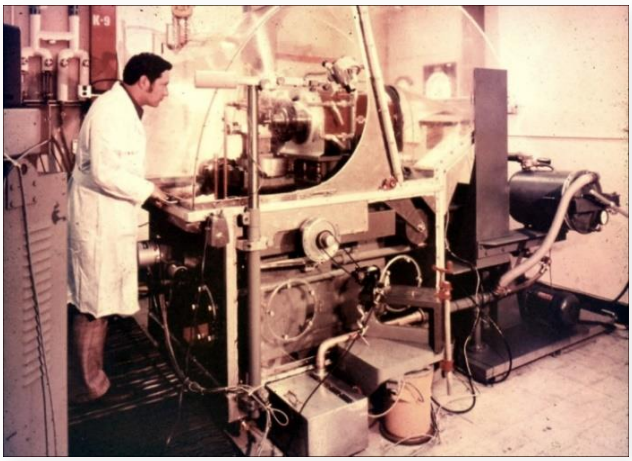

FIGURE 8. Oil shower on LLNL DTM1 in 1971 [8].

SUMMARY

Temperature effects are generally the largest single source of non-repeatability in machines and instruments. Precision requirements continue to become more difficult, however, materials used to build systems do not change. Therefore, the importance of temperature effects continues to increase with time.

Minimizing thermal effects through design is important. Controlling temperatures in and around precision systems has been the most cost-effective way to manage thermal effects. It directly addresses the root cause of the problem.

The choice of fluid for control of thermal stability should be based on the requirements. Air is the most practical fluid but has some limitations. Liquid should be considered when thermal variations need to be less than ±0.02°C.

It has been shown, with the successful installation of many systems, that controlling temperatures is not that difficult and can often be done at a fraction of the total system cost. The repeatability of a machine or instrument can often be improved by a factor of 4 or 5 with just a reasonable (±0.1°C) thermal environment around the equipment.

FUTURE WORK

Thermal compensation of machine tools based on many temperature measurements has been done but had limited practical value in precision machines [4-6]. However, this is an area that could be investigated using available software (e.g., TensorFlow) and constructing an appropriate neural network.

A large number of thermistors (perhaps 100 or more) could be mounted in and around a machine. This could be done at a cost of about $30/thermistor using purpose built, multi-channel signal conditioning electronics.

These measurements could be inputs to some type of neural network (Deep, Convolutional, Recurrent, …). Based on a geometric model of the machine (HTMs) [3], and with proper training in a programmable thermal environment, the network could potentially compensate the system at all positions within its working envelope.

The primary hardware cost for each machine would be the sensors and signal conditioning. The overall cost could be relatively low, as much as an order of magnitude below the cost of a typical air shower.

REFERENCES

[1] Horst Kunzmann, from PTB, Germany. Comment made at 6th Annual ASPE meeting, Santa Fe, NM, 1991.

[2] E.G. Loewen, “Metrology Problems In General Engineering: A Comparison with Precision Engineering”, CIRP Annals, vol. 29/2, 1980, pp. 451-453.

[3] Domnez, M.A. Some Guidelines for Implementing Error Compensation on Machine Tools. NIST IR 5236, 1993.

[4] Mize, C, Zeigert, J. Neural Network Thermal Error Compensation of a Machining Center. Precision Engineering, 2000; 24: 338-346.

[5] Abdulshahed, A, Longstaff, A., Fletcher, S, Potdar, A. Thermal Error Modelling of a Gantry-Type 5-Axis Machine Tool Using a Grey Neural Network Model. Journal of Manufacturing Systems. 2016; 41: 130-142.

[6] Mayr, J, Blaser, P, Ryser, A, Hernandez-Becerro, P. An Adaptive Self-Learning Compensation Approach for Thermal Errors on 5-Axis Machine Tools Handling and Arbitrary Set of sample Rates. CIRP Annals – Manufacturing Technology. 2018; 67: 551-554.

[7] Youden, D. Good Things Come in Small Packages: A Table Top CMM With Sub-Micron Capability. Proceedings ASPE Annual Meeting, 2001.

[8] Bryan, J, Donaldson, E, McClure, R, Clouser, R. A Practical Solution to the Thermal Stability Problem in Machine Tools. UCRL-73577, LLNL, 1971.

[9] Wood, S, Mangum, B, Filliben, J, Tillett, S. An Investigation of the Stability of Thermistors. NBS Journal of Research, 1978; 83: 247-263.

[10] Advanced Nanometric Coordinate Measurement Machine (ANCMM) concept test platform. An Opti-Pro Systems & UNCC design project sponsored by NASA Goddard Space Flight Center Phase II SBIR 80NSSC20C0171.

DEVELOPMENT AND EVALUATION OF DEVICE FOR SUPPRESSING SPINDLE HEAD VIBRATION CAUSED BY BEARING CAGE

Shotaro Tanaka, Ryoji Kondo and Hayato Koyama
R&D Department
YASDA PRECISION TOOL K.K.
1160 Hamanaka, Satosho, Okayama, Japan

INTRODUCTION

The demand for micromachining centers that can machine large workpieces with high precision and high quality surface grows up, due to the needs from the optical mold components such as automobile head lights. These demands require machining centers with spindles that can rotate at high speed with high accuracy. However, it is known that rolling bearings, which are widely used in machine tool spindles, generate vibration as typified by the orbital motion of rolling elements[1][2], and this vibration can be a problem when attempting to realize mirror surface finishing. Generally, the rigidity of the spindle head is lower than that of the other part of whole machining center, and the vibration is amplified at the frequency where it resonates with the vibration of the bearing caused by the spindle rotation. As a result, the quality of the machined surface deteriorates.

This study aims to develop a device which reduces the spindle head vibration caused by the vibration from the rolling bearings used in high-precision machining center spindles, and to demonstrate the effectiveness of the device.

EXPERIMENTAL PROCEDURES

The 3-axis vertical type machining center (YMC650, YASDA) is used for the experiment. *FIGURE 1* shows the structure of the machine. The spindle head of this machine has a spindle unit that is driven by rotation and protrudes from the support of the Z-axis guide. This structure is suitable for the accessibility to the workpiece and reducing the weight of the moving unit. Ball bearings are equipped in the spindle, and the machine can be used for a wide range of applications, from heavy-duty machining to micro-milling.

In the experiment, acceleration sensors were installed in the X-, Y-, and Z-directions on the spindle head to measure the vibration caused by spindle rotation. The experimental setup is shown in *FIGURE 2*. Furthermore, the hammering test were conducted using the same setup to investigate the characteristic frequency of the spindle head.

EFFECTS OF BEARING VIBRATION

Firstly, we measured the vibration amplitude while the spindle rotates at 35,000 min^{-1}, which is the maximum speed of the machine. The results are shown in *FIGURE 3*. The vibration frequency of 263 Hz was the largest in all axes, followed by 583 Hz. The vibration at 583 Hz corresponded to the rotation frequency of the spindle. On the other hand, the vibration at 263 Hz was considered to be the orbital frequency of the rolling element,

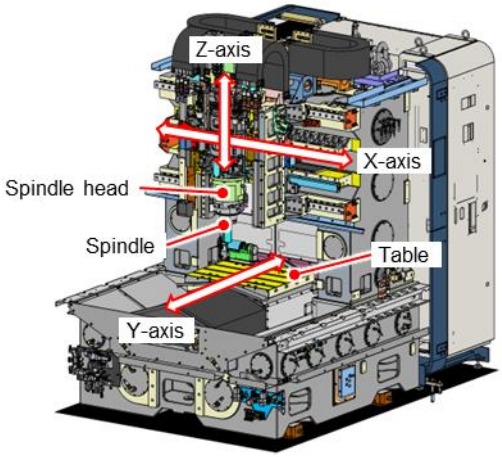

FIGURE 1. Machine structure.

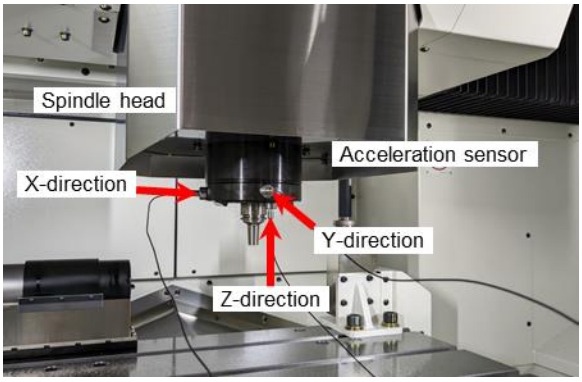

FIGURE 2. Experimental setup.

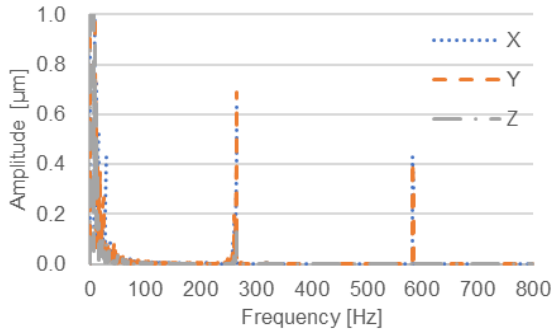

FIGURE 3. Vibration amplitude of spindle head at 35000min^{-1}.

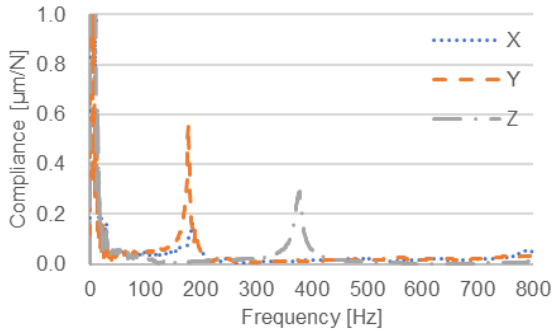

FIGURE 4. Spindle head compliance.

that is, the rotation frequency of the bearing cage. The vibration frequency caused by the bearing cage, fc, is calculated below:

$$f_c = \frac{1}{2} \cdot \frac{n_i}{60}\left(1 - \frac{D_a \cdot \cos\alpha}{d_m}\right) \quad (1)$$

In the equation above, n_i is the spindle speed [min^{-1}], D_a is the rolling element diameter [mm], d_m is the PCD of the rolling element [mm], and α is the contact angle of the rolling element [°]. From the above equation, it is calculated that the vibration frequency caused by the bearing cage used in this study is 0.45 times of the spindle rotation frequency. The calculated frequency corresponds to the former measurement results, 263Hz. The vibration caused by the spindle rotation itself can be reduced by adjusting the balance of the spindle rotor. For these reason, in this study, we focused on the vibration caused by the bearing cage.

Secondly, we conducted the hammering test when the spindle was stopped in order to investigate the resonance frequency of the machine. Among the results, the displacement of frequency response is shown in *FIGURE 4*. The characteristic frequency in the XY-direction was approximately 180 Hz, and that in the Z-direction was approximately 380 Hz. Therefore, the spindle

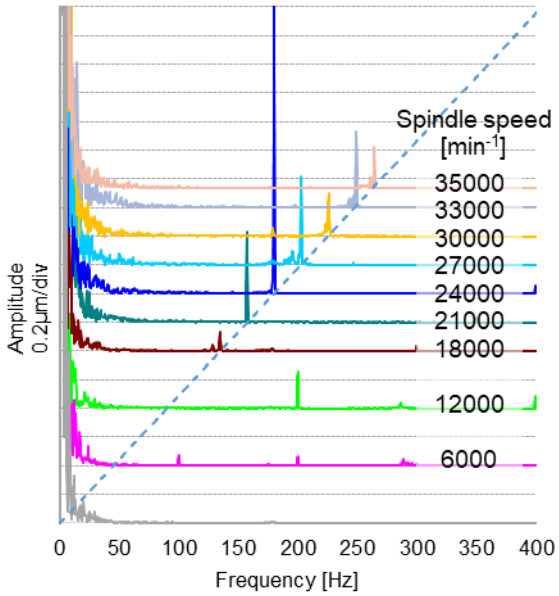

FIGURE 5. Comparison of vibration amplitudes caused by bearing cage at each spindle speed.

speed at which the vibration caused by the bearing cage resonates with the machine elements is 24000 min^{-1} in the XY-direction and 50666 min^{-1} in the Z-direction. Compared with the Y-direction, the X-direction has the same vibration characteristics although a smaller peak, and the Z-direction resonates at a higher RPM than the maximum speed according to the machine specifications. For these reason, we focused on vibrations in the Y-direction.

Finally, we measured the vibration of the spindle head during spindle rotation, every 3000 min^{-1} up to 35000 min^{-1}, to evaluate the velocity dependence of the vibration. The results are shown in *FIGURE 5*. This graph is shown with the vertical axis offset for each RPM, and the peaks on the dashed line are the vibration frequency of the bearing cage at each RPM. The dashed line represents the spindle rotation frequency multiplied by 0.45. The vibration amplitude at 24000 min^{-1} is especially large, which corresponds to the results of the hammering test. From this result, it has been confirmed that the vibration caused by the bearing cage resonated with the machine at a specific spindle speed.

EXAMINATION OF VIBRATION REDUCTION METHODS

The characteristic frequency in the XY-direction measured by the hammering test was confirmed

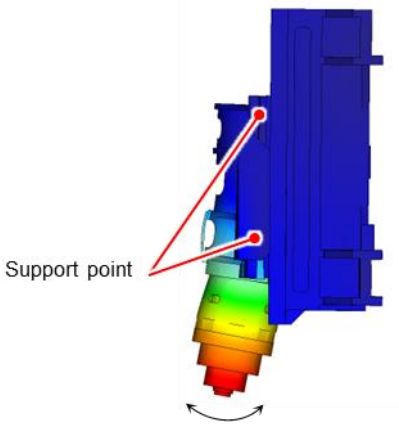

FIGURE 6. Vibration mode of spindle head.

with Finite Element Method (FEM) to be a characteristic vibration mode in which the spindle tip swung, as shown in *FIGURE6*. Therefore, we examined ways to reduce this vibration mode. Generally, damping devices are mounted near the point of vibration to improve the damping performance and reduce vibration. There are several possible ways to increase damping. In this study, we attempted to use frictional forces to absorb vibration energy.

A schematic of the developed vibration damping device (hereinafter referred to as “Damper”) is shown in *FIGURE 7*. In this Damper, laminated steel plates were mounted on metal plate fixed to the spindle head, and the laminated steel plates have movable gaps. When vibration occurs, it is damped by the sliding friction in between the steel plate.

We conducted a hammering test to investigate the performance of Damper. The results are shown in *FIGURE 8*. "Developed" is the data with the Damper, and "Conventional" is the data without the Damper. For more accurate evaluation, during the measurement of "Conventional", a dummy weight which is the same weight as the Damper itself has been mounted on the spindle head. This is because the difference in weight affects to the vibration characteristics. It was demonstrated that the compliance at the characteristic frequency was reduced to approximately 0.2 μm/N with Damper and that the compliance was approximately 60 % smaller than that of the conventional. From the results, it was confirmed that the developed Damper can improve the vibration level of the spindle head.

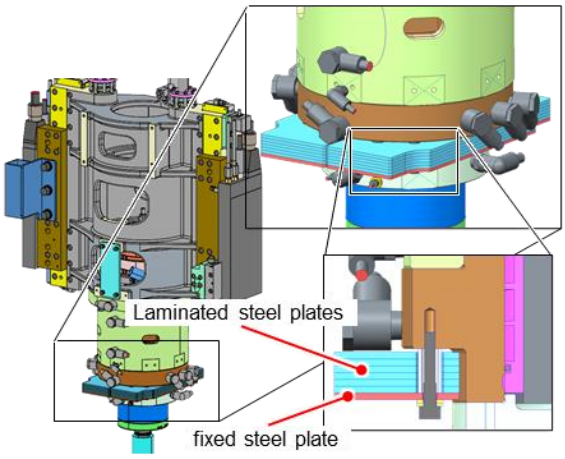

FIGURE 7. Schematic of Damper.

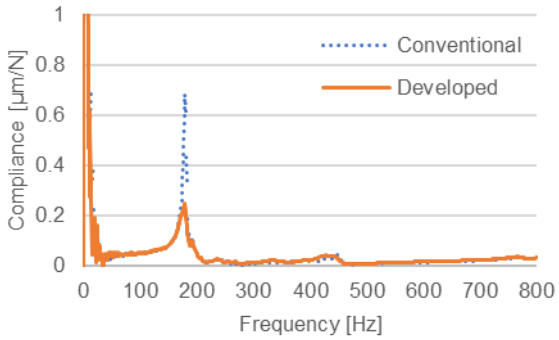

FIGURE 8. Comparison of spindle head compliance with and without Damper.

CASE STUDY

We machined the sample with finishing conditions used in actual micro-milling to demonstrate the effectiveness of the developed method. The machining conditions as follows; workpiece was a square pyramid with 45 ° tilted planes, cutting direction was X-direction to relatively increase the influence of Y-direction vibrations, the spindle speed was 35,000 min^{-1} and the feed rate was 1000 mm/min. The machined workpiece was measured in the tool feed direction with an autofocus probe 3D measuring instrument. The results are shown in *FIGURE 9*. The surface roughness of the workpiece with Damper was Ra 0.039 μm, which was approximately 50 % better the conventional condition.

In addition, the contour line of the workpiece surface was performed by Fast Fourier Transform (FFT) to investigate the factors that improved surface roughness. The results are shown in *FIGURE 10*. Even though the peak at 263 Hz (red circle) had appeared on both FFT spectrum, the

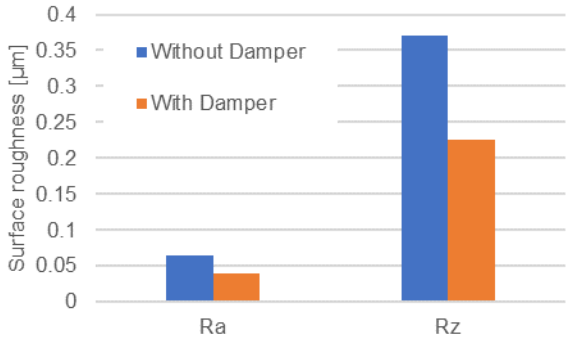

FIGURE 9. Comparison of surface roughness.

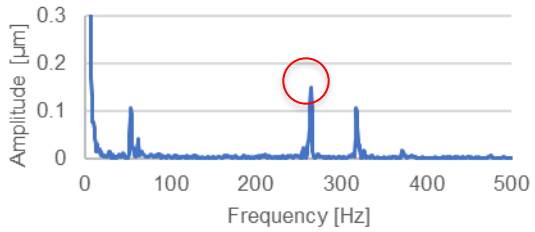

(a) Without Damper.

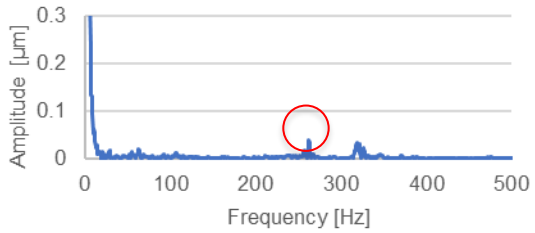

(b) With Damper.

FIGURE 10. Frequency analysis of finished machined surface.

level is much less in “with” Damper, compared to “without” Damper. From these results, it was confirmed that Damper using frictional force could reduce the vibration caused by bearing cage rotation and improve the surface roughness of the machined surface.

CONCLUSION

The damping device using frictional force has been developed to reduce the resonant vibration of the spindle head caused by bearing cage. The effectiveness of Damper was verified by the actual cutting test.

The conclusions obtained in this study are as follows:

1. Compliance at characteristic frequency has been reduced by 60% with the developed Damper. Damper has laminated steel plates with movable gaps, and the sliding friction in this structure helps to reduce the vibration caused by the bearing cage rotation.
2. The surface roughness of the workpiece was measured after actual cutting, and the arithmetic mean roughness improved by 50%. The results demonstrated the effectiveness of the proposed method.

REFERENCES

[1] Hiroyuki O. Sound and Vibration Research of Rolling Bearings in Japan. Journal of System Design and Dynamics. 2013; 7(2): 95-110.

[2] Shoji N., Yuta S., Takashi N., Tohru K. Influence of Inclination Error on Non Repetitive Run-Out of the Single Ball Bearing. Japan Society of Mechanical Engineers. 2012; 78(785): 272-281.

USING X AXIS ERROR TO BALANCE A PART ON A SPINDLE

Lauren Micklow[1] and Stephen Furst[1]

[1]Smart Material Solutions, Inc.

Raleigh, North Carolina, USA.

INTRODUCTION

Balancing workpieces on a spindle is a critical step to any diamond turning operation [1]–[3]. High end diamond turning machines come with integrated software to facilitate spindle balancing, but custom-made or older machines do not. Manually balancing is often a time-intensive, iterative process performed using accelerometers that are costly and may lack the necessary sensitivity. However, most machines are already measuring a signal that can be used for balancing: the X axis error motions that are excited by an imbalanced spindle. This work presents a procedure to correlate X axis error motion with the location and magnitude of spindle imbalances enabling a user to directly place balancing masses to compensate.

MODEL

The first step in compensating for an imbalanced workpiece is to determine the magnitude and position of the imbalanced mass. We can take advantage of the motion induced in the X axis by the spinning imbalance to determine these unknowns. The diamond turning machine (DTM) consists of a set of orthogonal axes and a spindle that are mounted to a granite slab that has an air isolation system beneath it (FIGURE 1 & FIGURE 2). During turning operations, a tool post rests on the axes, modeled as a payload in FIGURE 2.

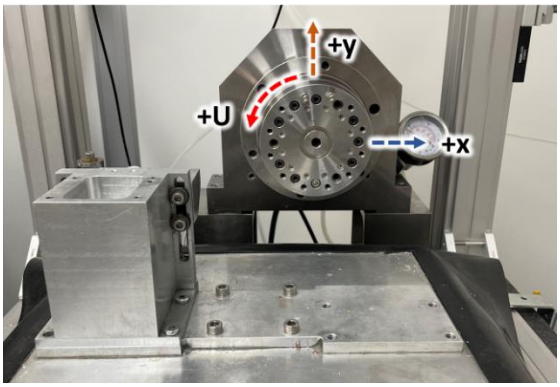

FIGURE 1. *DTM and its axes*.

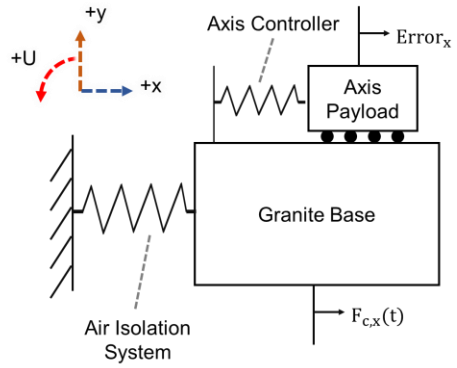

FIGURE 2. *Diagram of DTM.*

To begin analyzing the system, a simple model of the motion is derived without the impact of the controller gains. As the spindle rotates, the centrifugal force will act outwards from the center of the part, pointing towards the center of the imbalance. When the imbalance approaches 3 o'clock and 9 o'clock, the centrifugal forces align with the X axis and generate the peak forces in the positive and negative directions. The rotating mass will generate an oscillating force in the X direction, given by equation 1. The forces acting in the Y direction will be shifted by 90 degrees (equation 2). The commanded spindle position is plotted in red and wraps between 0 and 2π (equation 3). For equations 1 and 2, the U offset of the imbalance is denoted by θ_0, which is defined as the position of the U axis when the imbalance is at 12 o'clock.

Equations 1-3 are plotted in FIGURE 3, where the amplitude B is a function of the mass of the imbalance, the radius of the imbalance and the spindle speed.

$$F_{c,x} = -B\sin(2\pi ft - \theta_0) \quad (1)$$

$$F_{c,y} = -B\sin(2\pi ft - \theta_0 - \frac{\pi}{2}) \quad (2)$$

$$U_{command} = mod(2\pi ft, 2\pi) \quad (3)$$

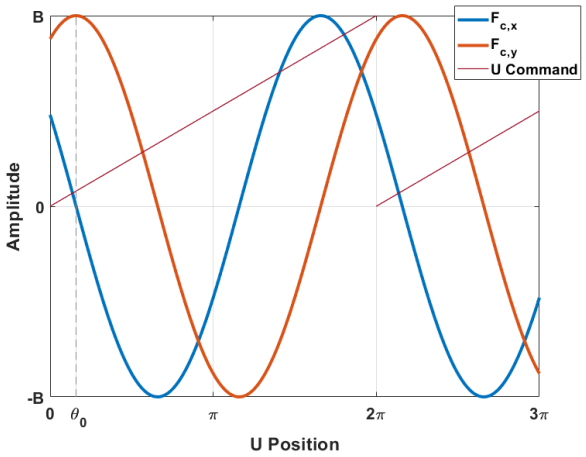

FIGURE 3. *Centrifugal forces in the x and y directions as an imbalanced part rotates.*

In practice, the peak X errors lag the peak X centrifugal force, and the lag is influenced by controller stiffness; note that Y forces are henceforth ignored (FIGURE 4). This phase delay must be added to compensate, signified by θ_d in equation 4. The magnitude (A) and phase delay in the X axis error is influenced by the mass on the axes, controller stiffness, spindle speed and mass of the imbalance.

$$\boldsymbol{X_{err} = -Asin\,(2\pi ft - \theta_0 - \theta_d)} \qquad (4)$$

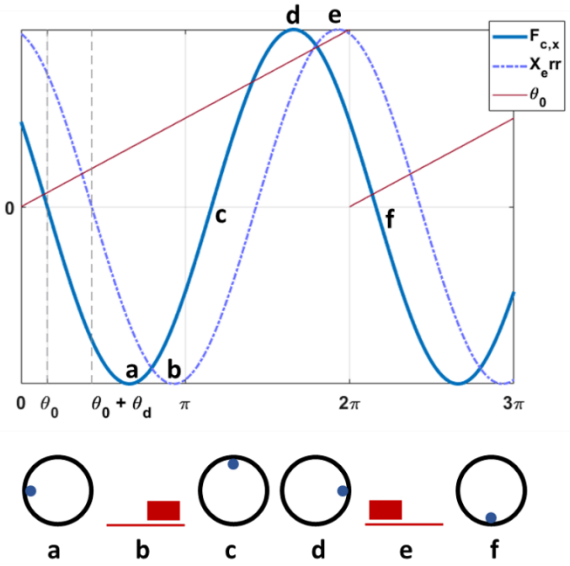

FIGURE 4. *The centrifugal forces align with the X axis at **a** and **d** but controller dynamics cause a following error. The peak X errors occur at **b** and **e.***

METHOD

Due to the complexity of the system and the growing number of unknown variables, a practical method can be generated to determine the imbalance compensation factors:

2) Center an unknown part by its OD, and spin it while measuring x-axis following error.
3) Calculate the estimated magnitude and location of the imbalance based on 1.
4) Place a balance mass and repeat until the magnitude of the x error is sufficiently reduced.

To characterize the X axis following error (step 1 above), the induced x axis following error is measured for different spindle speeds and known imbalance magnitudes. For these characterization tests, the axis payload and controller gains were held constant.

The first test determined the impact of spindle speed on following error. A mass of 14.1 grams was placed at a radius of 68.3 mm with a U offset ($\boldsymbol{\theta_0}$) of 90 degrees. Then the spindle was spun at speeds from 400 RPM to 1200 RPM and data was collected for each trial. Next the raw data for 18 revolutions was filtered with a moving average filter and the magnitude and phase lag of the X error peaks were determined. An example of this is shown in FIGURE 5, where the black dots represent the averaged peaks of the filtered data.

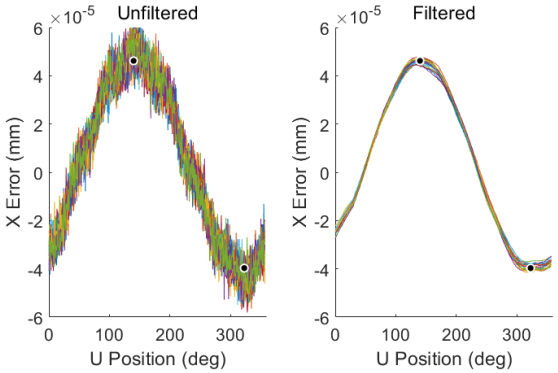

FIGURE 5. *Spindle position versus the X axis error, when spun at 400 rpm.*

Next the induced X error motions for each speed were compared. FIGURE 6 shows the X error for

a single revolution at each speed and shows the magnitudes of the X error plotted against spindle speed.

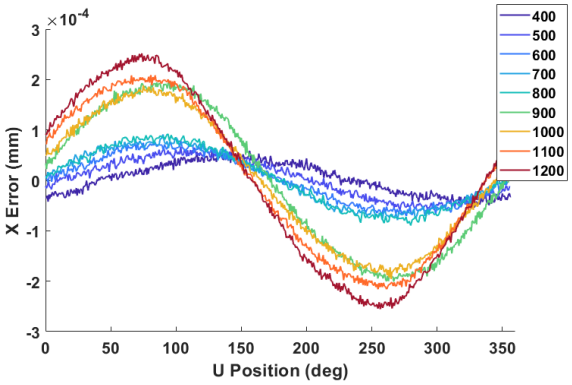

FIGURE 6. *Spindle position vs X Error of a single revolution for 400 to 1200 rpm.*

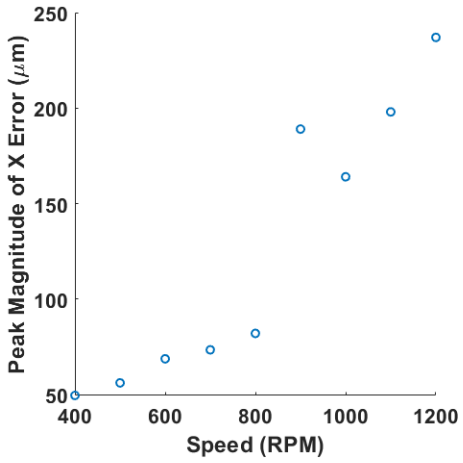

FIGURE 7. *Speed vs Peak Magnitude of X Error.*

FIGURE 8 plots the phase lag of the following error relative to the centrifugal force ($\boldsymbol{\theta_d}$ in equation 4), taken as the U position of the positive X error peak minus 90 degrees (the known $\boldsymbol{\theta_0}$ value).

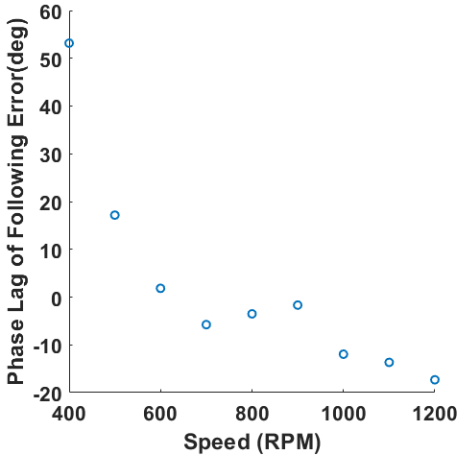

FIGURE 8. *Speed vs the axis lag of the induced X error.*

As spindle speed increases, the X error magnitude increases and the phase lag decreases. Both experience an increase around 900 RPM; this is likely caused by the spindle speed nearing the natural frequency of the vibration isolation system.

Next the imbalance magnitude was varied. The spindle was spun at 500 RPM to remain below the natural frequency of vibration isolation system. Three masses were chosen and placed at a known radius, giving imbalances of: 477.2 g-mm, 960.5 g-mm & 1446.4 g-mm. The X error magnitudes and axis lags were plotted against imbalance magnitude for each trial (FIGURE 9 & FIGURE 10).

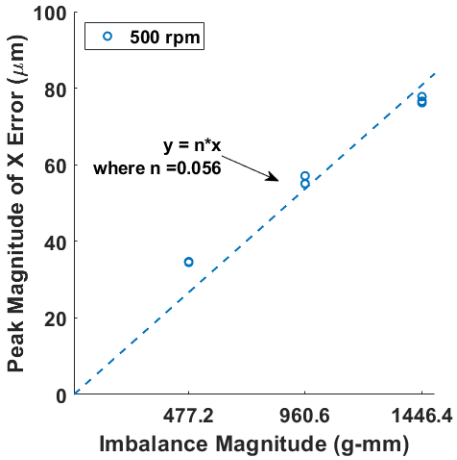

FIGURE 9. *Magnitude of the imbalance vs the peak magnitude of the induced X error.*

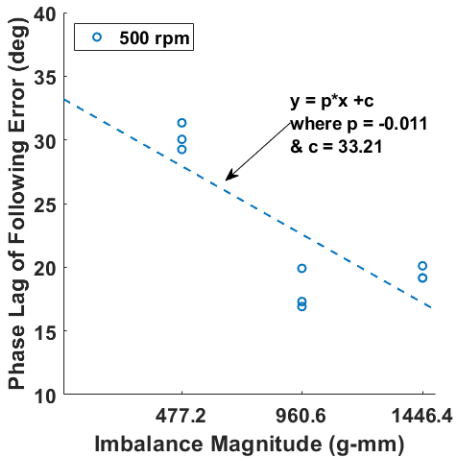

Now, linear trendlines fit to the data in FIGURE 9 and FIGURE 10 can be used to determine the magnitude and U position of the imbalance.

$$mass = \frac{Peak\ Magnitude\ of\ X_{err}}{n * radius} \quad (5)$$

$$\theta_d = p * mass * radius + c \quad (6)$$

DEMONSTRATION

For the second step, an unbalanced part was centered on the spindle using a dial indicator on the outer diameter (FIGURE 11). Then the spindle was spun at 500 RPM, and the X axis motion was recorded (FIGURE 12).

During the third step, the motion is analyzed to characterize the imbalance. The peak X_{err} occurred at 245 degrees and had an amplitude of 50.6µm. Using the amplitude and equations 5 & 6, the correction mass was determined to be 13g to be placed on the ID of the workpiece, which has a radius of 69.85mm, and axis lag was estimated as 23.2 degrees.

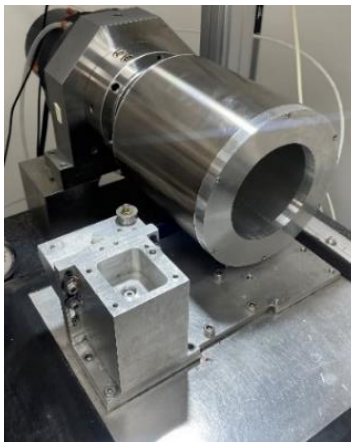

FIGURE 11. *Unbalanced workpiece on DT lathe.*

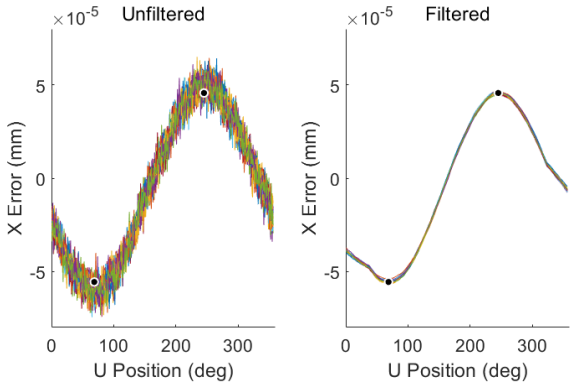

FIGURE 12. *Baseline measurement of the unbalanced workpiece.*

The spindle was rotated to 222 degrees and a mass of 13 grams was placed at '3 o'clock' (step 4). This process was repeated until the error amplitude was less than 50nm (FIGURE 13 & FIGURE 14). The compiled measurements and calculated corrections are found in TABLE 1 and revolutions from each trial are plotted in FIGURE 13.

TABLE 1. Measured errors (green) and calculated correction factors (blue).

	θ_{min} (degrees)	θ_{max} (degrees)	X_{err} min (µm)	X_{err} max (µm)	X_{err} amplitude (µm)	correction mass (g)	θ_d (degrees)
Baseline	68.8	245.0	-55.6	45.7	50.6	13.0	23.2
Correction 1	181.8	345.3	-23.3	20.9	22.1	5.7	28.8
Correction 2	140.6	341.8	-12.9	3.95	8.42	2.2	31.5
Correction 3	129.4	312.0	-10.3	0.739	5.53	1.4	32.1
Correction 4	70.9	261.5	-7.91	-1.49	3.21	0.8	32.6

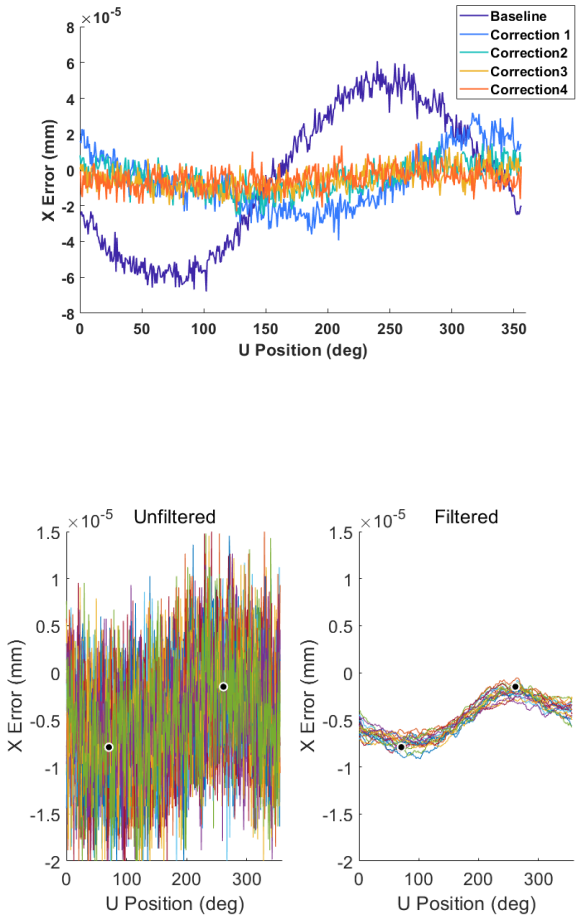

FIGURE 14. *Final measurement of the balanced workpiece.*

CONCLUSION

The presented procedure for correlating X axis error motion with spindle imbalances offers a practical and efficient solution to the critical step of balancing workpieces for diamond turning operations.

The procedure can be easily applied to custom-made or older machines that lack integrated software for spindle balancing as it makes use of signals that most machines are already recording. Unless axis dynamics or axis payloads change, the imbalance compensation factors should remain consistent, allowing for rapid balancing as iteration time is less than five minutes and the error typically converges in 3 to 4 steps.

The procedure also has potential to improve over time. With advancements in machine models or the application of AI analysis to previous calibrations, the accuracy and efficiency of the balancing process could be further refined.

REFERENCES

[1] Z. Dong, S. Zhang, Z. Xiong, and X. Rao, “A generalized dynamic model for spindle vibration influencing surface topography in different ultra-precision machining processes,” *International Journal of Advanced Manufacturing Technology*, vol. 96, no. 5–8, pp. 2471–2478, May 2018, doi: 10.1007/s00170-018-1814-3.

[2] K. Manjunath, S. Tewary, N. Khatri, and K. Cheng, “Monitoring and predicting the surface generation and surface roughness in ultraprecision machining: A critical review,” *Machines*, vol. 9, no. 12. MDPI, Dec. 01, 2021. doi: 10.3390/machines9120369.

[3] P. Huang, W. B. Lee, and C. Y. Chan, “Investigation of the effects of spindle unbalance induced error motion on machining accuracy in ultra-precision diamond turning,” *Int J Mach Tools Manuf*, vol. 94, pp. 48–56, Jul. 2015, doi: 10.1016/j.ijmachtools.2015.04.007.

DISPLACEMENT-DRIVEN BALANCING OF A MACHINE FLYCUTTER

Stephen T. Hayes
National Ignition Facility
Lawrence Livermore National Laboratory
Livermore, California, USA

INTRODUCTION

The National Ignition Facility (NIF) is the world's largest and highest-energy laser system, concentrating 192 beams into a cubic millimeter [1]. The Integrated Optics Modules (IOMs) house the final optics in the laser beampath prior to target interaction. Within each of the 192 IOMs are two Potassium di-Hydrogen Phosphate (KDP) optics which enable frequency conversion from the incoming 1ω light (1053-nm), stepped next to 2ω (527-nm) visible green light, then finally to 3ω (351-nm) ultraviolet radiation. The Optics and Materials Science & Technology (OMST) organization oversees the fabrication of these 420 x 420 mm KDP optics [1]. Originating from large-growth, single grain KDP crystal, these optics are fabricated using an iterative process of diamond turning a surface and measuring the crystallographic axis to optimize frequency conversion for each optic type. The diamond turning Semi-Finishing Machine (SFM) and Moore Finishing Machine are used in the iterative crystal fabrication process.

PRECISION BALANCING

To achieve the world-class surface finish, the alignment of the flycutter assembly's center of mass to the axis of rotation is imperative as an off-balanced assembly may result in machine vibration, cutting tool error motion relative to the workpiece, and spindle failure. A one-dimensional dynamic balancing operation for the flycutter assembly is crucial to the performance of the precision machines. This operation is performed anytime the configuration of the spindle, or its tooling, is modified such that an unbalanced condition may occur.

DISPLACMENT-DRIVEN BALANCING

At Lawrence Livermore National Laboratory (LLNL), we have nearly 40 years of history using displacement sensors, such as capacitance gauges. The process of dynamic balancing a rigid machine rotor at LLNL using eddy-current displacement sensors was first presented at the 8th CUBE Symposium in Albuquerque on November 18th, 1998, by Blaedel, Davis, and Hansen. This newly presented method was stated as "being required for ductile grinding which takes place at small depths of cut (e.g., 0.2 µm)" [2].

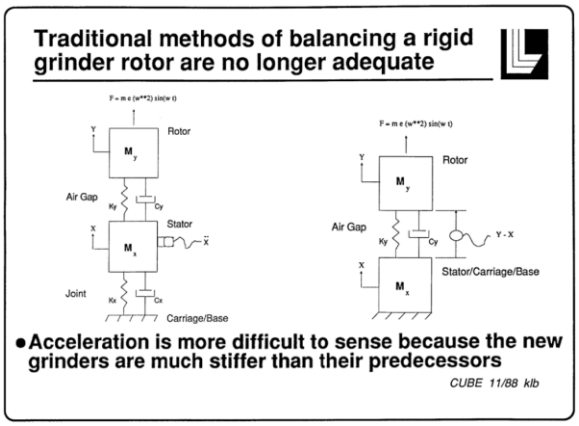

FIGURE 1. Blaedel, Davis, and Hansen, 8th CUBE Symposium view graph.

This method was first adopted upon the assertion that accelerometer-based methods were characterized as being less optimal for stiffer grinding machine structures as the off-balance accelerations were more difficult to sense.

The process of balancing a precision machine spindle mounted flycutter assembly using displacement sensors is presented in the context of two work examples, one on each style of diamond turning machine the NIF uses for KDP optics fabrication. These one-dimensional balancing efforts were performed after installing the diamond turning machine's 0.76-meter diameter flycutter assembly to the Professional Instruments Company 10R blockhead spindle which is part of the tool rotation axis. It is notable that the SFM uses a motorized 10R block head spindle while the Moore Finishing Machine uses a flexure coupled motorized 4R block head. See Figure 2 for an example of a displacement sensor applied to a diamond turning machine flycutter.

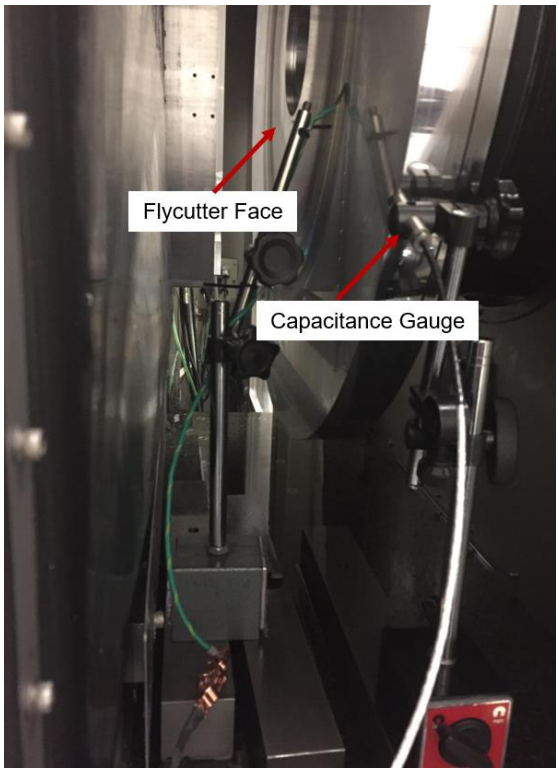

FIGURE 2. Moore Finishing Machine flycutter with capacitance sensor and ground wire applied.

Balancing Process

The process of balancing has been enhanced over the years as advances have been made in software, data acquisition systems, tooling, and instrumentation. A custom software program was developed at LLNL for displacement driven balancing in the context of these diamond turning machines. Prior to dynamic balancing of the system's flycutter a static balanced state of the flycutter must be established. This prerequisite mitigates the risk of spindle damage at the onset of the dynamic balancing process.

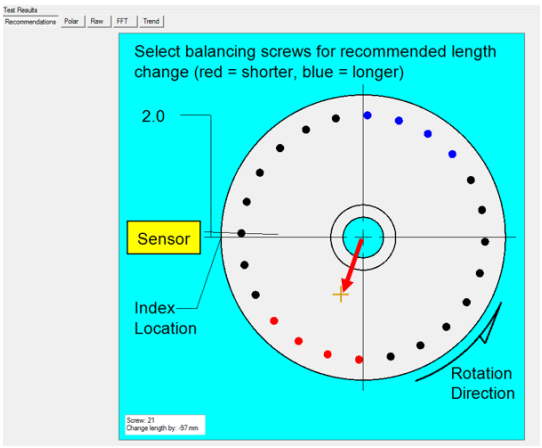

FIGURE 3. Custom Balancing Program.

The user input to the software is a calculated acceptance criteria for balancing as well as the derived machine stiffness value. These values paired with displacement sensor feedback and a once-per-revolution trigger signal inform the prescribed corrective action provided to the user by the software as shown in Figure 3. These corrective actions are made at increasing rotational velocities until the operational velocity is reached.

The software presents feedback to the user in the form of raw sensor voltage signal, a polar representation of the voltage, a FFT for RMS displacement, and the prescribed flycutter mass reconfiguration warranted. Manipulation of the center of mass is achieved by altering the length of a balancing-specific fastener(s) arrayed around the flycutter perimeter.

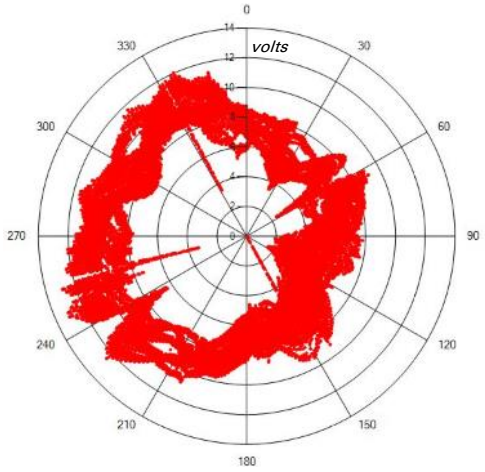

FIGURE 4. Polar plot of the capacitance sensor balancing voltage feedback.

Equipped with this software, the user can converge on a balanced system up to the operating rotational speed in a systematic manner. The software, at a high level, was designed to record two data sets simultaneously: (1) a voltage signal related to unbalance, and (2) voltage pulses of a once-per-revolution index marker. Both data sets are recorded as a function of time. The software then executes postprocessing of the data and provides the user with an unbalance figure of merit, or imbalance performance, and then provides a recommendation of where and how much mass to add or subtract from the system to improve the balance.

This software requires the operating technician to input parameters for expected flycutter

revolutions per data set captured, bearing stiffness, and acceptable displacement. Bearing stiffness is solved for by introducing a known mass (i.e., varying an M5 balancing-screw length) to the system and measuring the system's response, which is a shift in displacement of the actual and calculated center of gravity. For reference, the bearing stiffness derived using this process in 2018 for the Moore Finishing Machine was ($ksys_radial$ = 600 N/mm). The Acceptance Criteria (AC) acts as the "go/no-go" logic gate during the balancing sequence were the measured total indicator reading (TIR) ≤ (AC).

The revolutions per data set specifies the number of flycutter rotations to be achieved, at a known speed, to constitute a complete displacement data set. This user-defined value dictates the test sample population to be used for the least-squares circle fit calculation that the software uses to approximate the flycutter phase position as well as the relative center of gravity location.

Balancing Setup

The displacement driven balancing setup used on the Moore and Semi-Finishing Machine's was composed of a Lion Precision Capacitance gauge, grounding wire, amplifier, and mount. A DG535 Stanford Research Systems digital delay/pulse generator was used to receive and elongate the motorized air bearing spindle's trigger signal. This signal, in addition to the displacement sensor output, was passed to a National Instruments computerized data acquisition system, NI cDAQ-9134. Diamond tools and fixturing were also used to diamond turn the flycutter diameter to provide a valid measurement surface.

This setup differs from documented legacy LLNL displacement-driven balancing method due to the use of a high-resolution capacitance gauge and the once-per-revolution motor encoder signal. The capacitance gauge takes the place of the previously used eddy-current displacement sensor. The primary reason a capacitance sensor is optimal for our application is that eddy-current sensors inherently possess electrical runout where capacitance sensors do not when properly grounded. Secondary considerations were the generally clean environment and that the measurement range required is relatively small. Lastly, where an optical switch paired with a flag attached to the flycutter once provided the trigger signal the spindle motor encoder now provides that input.

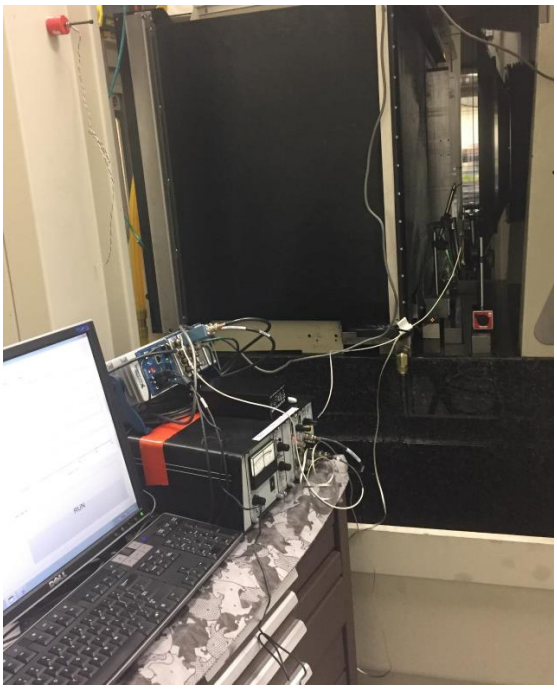

FIGURE 5. Balancing equipment setup.

BALANCING QUALITY REQUIREMENT

The property which governs the degree to which a system is to be balanced can be driven by either bearing force requirements, vibration limitations, experimental evaluation, or use of established general balanced quality grades. Balance quality of the Moore and Semi-Finishing diamond turning machines were found to be governed by allowable bearing force requirements.

Both diamond turning machines have the flycutter assembly mated to a Professional Instruments (PI) 10R precision air bearing. This is a high load capacity and high stiffness spindle with nanometer-level error motion, making it ideal for precision machining, specifically diamond turning and grinding. By nature of being an air bearing, where the rotor and stator are separated by a thin, high pressure, layer of air. The load capacity and stiffness are approximately linear with the air pressure supplied. Bearing force requirements are made relevant in the consideration of permitted system imbalance as an ultimate load capacity exists such that the bearing air gap is compromised, that is rotor and stator contact is made. This is a catastrophic state for any precision air bearing and thus warranted consideration.

Both vibration limitations and established general balanced quality grades were assessed and found to not be the governing balance quality

demand. The ISO standard 1940-1:2003(E) provides a relevant balancing standard as it covers systems where the outermost bearing rotor/stator (A & B) planes are identified as the critical bearing tolerance planes. This was specific to an outboard rotor with mass center in an overhung position, see ISO standard's figure below [3]. This directly replicates the Moore Finishing Machine bearing system which consist of a motorized air bearing spindle coupled to a larger air bearing which holds the cantilevered flycutter.

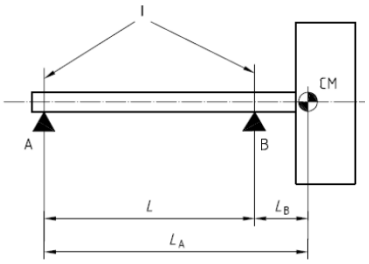

Key
1 tolerance planes (= bearing planes)
CM is the centre of mass.

FIGURE 6. Outboard rotor with mass center in an overhung position; ISO standard 1940-1:2003(E), Figure 4.

This figure, while depicted in what is easily interpreted as a horizontal rotation axis state, also applies to a vertically configured system as the mass center continues to be outboard. As mentioned, this aligns naturally with our Moore and Semi-Finishing Machines as the flycutter undergoing dynamic balancing is cantilevered off one face of the PI 10R blockhead air bearing. The rotor configuration presented is also similar to the SFM with the exception that the spindle-flycutter pair are oriented horizontally. This deviates from the above figure as gravity, for this system, is no longer acting normal to the rotation axis.

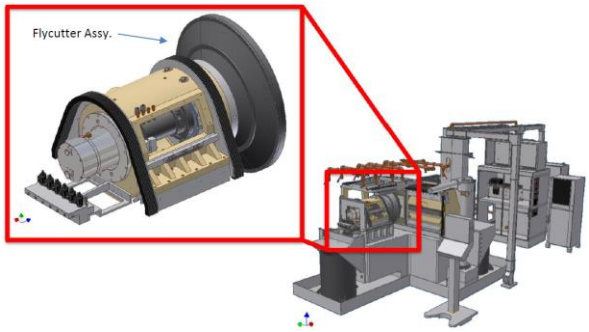

FIGURE 7. Moore Finishing Machine Spindle and Flycutter orientations.

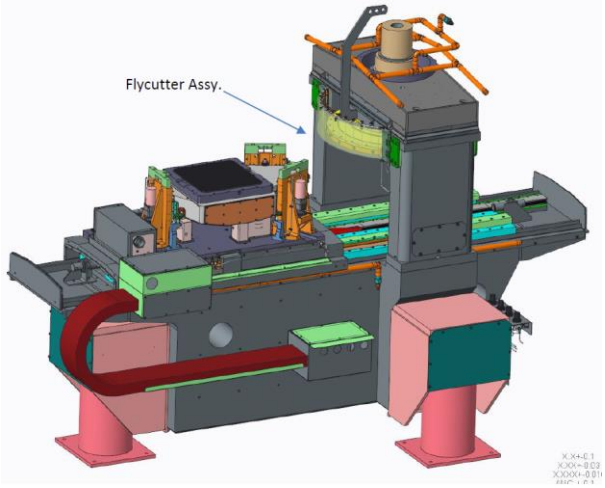

FIGURE 8. SFM Spindle and Flycutter orientations.

The ISO 1940-1:2003(E) standard derived permissible unbalance, at 1,000 rotations-per-minute (rpm), was found to be 4.0 µm. This is greater than the adjusted bearing flying height, h = 1.65 µm, which was assumed to govern the permissible imbalance. While the ISO standard is insufficient for direct radial bearing gap permissible unbalance, it does closely align with the full system displacement criteria or permissible unbalance, especially for the less stiff Moore Machine. It is notable that the SFM's stiffer machine structural loop, demanded a tighter displacement criterion to be imposed. Overall, these system values reveal that the spindle bearing force requirement is the more stringent aspect and should drive the balancing quality requirement. This requirement can be measured and balanced to, using the flycutter as the rotor reference, after the above system stiffness transformation calculation has been made and the displacement criteria derived.

Balance Achieved

The new balancing equipment and software were first used in 2018 on the Moore Finishing Machine following exchange of the 10R Blockhead spindle; it was subsequently used in 2020 on the SFM for transport back to and rebuild at LLNL. Both efforts resulted in a successfully dynamically balanced flycutter less than 100 micro-g or a total indicator reading (TIR) of 1.6 µm up to 1,000 rpm.

Two balancing efforts were performed using this modernized dynamic balancing approach and software. First, in 2018 following the exchange of the Moore Finishing Machine's PI 10R air bearing spindle which required removal and reinstallation

of the flycutter. The second effort was the 2020 build of a Semi-Finishing Machine onsite at LLNL. The final balance of the Moore Finishing Machine flycutter was below 1.621 µm with the Z-stage floating on its hydrostatic linear bearing axis. This is optimal for balancing as the added system compliance permits ease of sensing system imbalance. The Moore's subsequent measured imbalance in the machines operational cutting position, with the Z-stage hydrostatics disabled, allowing a stiffer system to be obtained, was 1.093 µm. Both results surpassed the derived balancing acceptance criteria for the machine at roughly 3.0 µm. The 2020 SFM balancing effort required a modified balancing setup from what was applied to the Moore. See Figure 9 below. The use of an aligned single ball artifact was applied at the flycutter center for reference. This was used in place of the flycutter outside diameter as it offered a more stable structural loop.

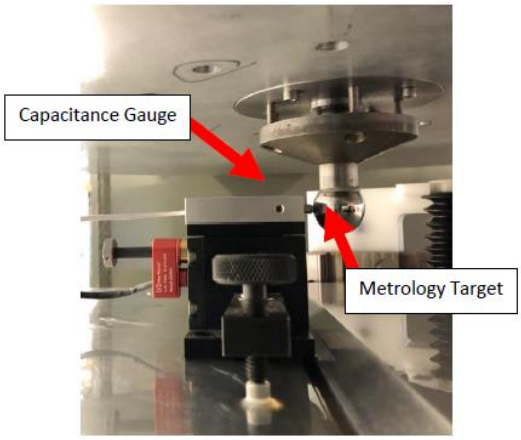

FIGURE 9. Flycutter Balancing Setup on the relatively stiffer SFM.

The SFM final dynamic balance achieved was 0.167 µm. This surpassed the calculated balancing requirement of ~0.2 µm for this overall stiffer system, hence the order-of-magnitude more stringent balancing requirement compared to the Moore machines. It was anticipated that the spindle's vertical orientation would influence the acceptance balancing criteria in a manner that increased the permissible unbalance. This was due to the larger SFM critical gap or flying height because of the absence of the rotor's gravity sag. The SFM's larger flying height resulted in a 3-times greater force required to compromise the air gap. The influence of this, however, is dwarfed when compared to the influence of the system stiffness. It was found that the SFM's system stiffness was nearly 6-times greater than that of the Moore. Another perspective is to convert the stiffness to compliance and compare: 0.083 µm per Newton force for the Moore compared to 0.014 µm per Newton of force for the SFM. This heightened SFM structural stiffness required a balancing criterion an order-of-magnitude more stringent at roughly 0.2 µm rather than the Moore's 3.0 µm.

FUTURE WORK

The displacement-driven balancing method can be susceptible to both measurement surface runout error, shifting rotor position at differing speeds [2], and phase shifts within the data sets. Revisions to the process and software were found to be warranted following these efforts. Chiefly, incorporating a system stiffness and phase shift detection step into the software's initialization routine.

CONCLUSIONS

This dynamic balancing work gave a new perspective to the traditional technique developed at LLNL for balancing stiff machine rotors up to and at working rotational speed. The displacement-driven balancing method provides a unique way to achieve a balanced machine tool rotation axis. This balancing approach informs system balancing correction based only on the measured coherent imbalance contributor.

ACKNOWLEDGMENTS

Paul Geraghty, crystal finishing SME, developed the custom balancing software used for this work on the NIF diamond turning machines. Sam Thompson, senior metrologist, developed the equipment and techniques instrumental to the success of both this work as well as the KDP crystal production facility for the NIF. Prepared by LLNL under Contract DE-AC52-07NA27344.

REFERENCES

[1] P. A. Baisden, L. J. (JANUARY/FEBRUARY 2016). Large Optics for the National Ignition Facility. FUSION SCIENCE AND TECHNOLOGY · VOLUME 69, 295–35.

[2] Blaedel, K. L., Davis, P. J., & Hansen, H. J. (7/13/1988). BALANCING A ROTOR WITH DISPLACEMENT SENSORS. 8th CUBE Symposium. Albuquerque.

[3] 1940-1:2003(E), I. (2003-08-03). Mechanical vibration — Balance quality requirements for rotors in a constant (rigid) state — Part 1: Specification and verification of balance tolerances (2nd ed.). INTERNATIONAL STANDARD.

Magnetic Preloaded Air Bearings for Precision Applications

Andrew D. Devitt[1], Jeremy W. Rainey[1]
[1]Reseach and Development
New Way Air Bearings

Methods for Preloading Air Bearings

Air Bearings have a wide range of applications which all require specific needs. In the precision motion industry, stability and stiffness are paramount to control motion as accurately as possible. When lightly loaded, air bearings can have a tendency to have low stiffness within the air gap as dynamic forces are imparted to the system. To counter this, it is usually advised to heavily preload the bearings, therefore increasing the stiffness of the bearing system significantly. There are a few ways to achieve the require preload. Adding mass to the stage to approach the load capacity of the bearing will increase the stiffness significantly. Preload is commonly achieved with a bearing directly opposing the load carrying bearing. When space does not allow for opposing bearings, a vacuum preloaded (VPL) bearing can be used. A VPL has a vacuum feature within the bearing that pulls vacuum on the guide surface to create the necessary preload. Both of the latter options require additional structures and air supply needs. Another option is utilizing magnetic preload. A standard flat air bearing can be used in conjunction with a magnet and magnetic metal guideway. The magnetic attraction creates the required preload for the bearing system while simplifying the overall structure.

Magnetic Preload for Air Bearing stages

Magnetic Preloaded bearings have many advantages over other preloading types which makes them an ideal solution for many precision applications. There is no need for additional structures as found in opposed bearing setups. This reduces the overall size requirement and mass of the stage or carriage. It also reduces the amount of bearings needed in the system. A typical box way slide may have upwards of 12 air bearings. With a magnetic preloaded system, only 6 air bearing and magnet pairs are needed. It also reduces the amount of precision ground faces required to manufacture the guideway for these stages. Such an example is of the stages donated to the ASPE Student Challenge in 2021. These precision stages have a lightweight Aluminum slide with 4 top bearings and 2 side plane bearings which rides on a nickel plated steel guideway. The bearings and magnets are bonded to the slide with Moglice at predetermined gaps to create the necessary preload. This is a very simple setup which optimizes performance, size, and cost.

REVOLUTIONIZING PRECISION: INNOVATIVE APPLICATIONS OF AIR BEARINGS IN HIGH-PERFORMANCE SPINDLES

Murat Erturk

OAV Air Bearings
Princeton, New Jersey, 08540, USA

INTRODUCTION

This study offers a comprehensive overview of the transformative potential of air bearings for high-performance spindles, particularly in contexts that demand precise motion control, such as high-end manufacturing, precision instrument assembly, and advanced micro-fabrication.

And should be used as a guide for readers interested in the innovative applications of air bearings in high-performance spindles. Readers are encouraged to refer to the detailed support from OAV or an in-depth understanding of the principles changes, designs, implementation strategies, and future challenges.

Air bearings have historically demonstrated immense value in industries reliant on high-precision operations and spindles, given their virtually frictionless performance and high-speed capabilities. However, traditional spindle designs have struggled with limitations in thermal stability and stiffness, which can compromise performance and accuracy. Addressing these challenges in this study presents novel designs equipped with pre-loaded air bearings, designed to enhance their functionality in high-performance spindles.

The study initially outlines the fundamental principles of air bearings and their application in spindle technology, highlighting both the merits and the limitations of existing approaches. The subsequent sections present a detailed examination of novel design modifications and integration strategies for air bearings in spindle systems. In particular, we introduce OAV's Roller Air Bearing, Thrust Air Bearing and Tapered Air Bearing design, which combine aerostatic and aerodynamic principles to enhance precision, load capacity and maintain high rotational speeds with improved thermal stability while implementing easy installation. This innovative design significantly mitigates performance degradation often seen in high-speed spindle operations.

Furthermore, we present an adaptive feedback control system designed to optimize air gap uniformity, providing better stiffness and further reducing thermal expansion issues. By continuously monitoring and adjusting the air gap in real-time, the system ensures consistently high performance across a range of operating conditions.

The research also elucidates the implementation of the above advancements in diverse application contexts, demonstrating how these improvements can revolutionize the precision and performance of spindle-driven operations. From micro-scale component manufacturing to sophisticated scientific instruments, the implications of these findings are far-reaching.

Finally, we also discuss potential challenges in the large-scale adoption of these innovations, such as cost factors and the need for specialized maintenance and training. We propose possible solutions to these issues, fostering a roadmap for the future integration of air bearings into high-performance spindle applications.

Through this study, we unveil the future of spindle technologies, where the amalgamation of innovative air bearing design, intelligent control systems, and comprehensive implementation strategies promises to redefine the benchmarks of precision and performance.

I. Fundamental Principles and Applications of Air Bearings in Spindle Technology

Air bearings leverage a thin film of pressurized air to support a load, where no contact between the surface reduces friction and enables high-speed, high-precision operations. This design allows spindle applications to operate with higher rotational speeds and less vibration, compared to traditional mechanical contact bearings.

1.1 Merits of Air Bearings in Spindle Systems:

Air bearings in spindle systems have several merits that can significantly improve system

performance, particularly in applications that demand high precision, speed, and longevity. The key advantages of air bearings include:

Nearly No Friction: As there is no physical contact in air bearings, they generate virtually no friction. This dramatically reduces heat production and enables high-speed operation without compromising the bearing's dimensional stability or precision.

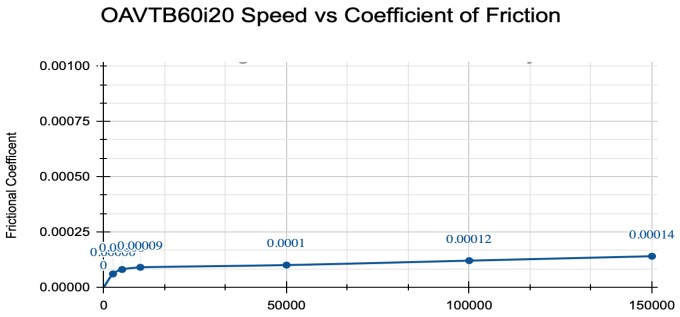

(1)

Reduced Wear and Tear: The lack of contact in air bearings eliminates wear and tear, extending the system's lifespan. This significantly reduces the need for maintenance and replacement, lowering the total cost of ownership.

Low Noise and Vibration: Air bearings produce less noise and vibration compared to contact bearings because there are no mechanical components in contact. This leads to a smoother operation, benefiting precision-demanding applications.

Ultra High Speed Capabilities: Air bearings can support higher rotational speeds as there are no mechanical constraints or friction-induced heat that can limit operational speeds.

Zero Lubrication: Air bearings do not require any lubrication, eliminating maintenance associated with lubrication schedules and the potential for contamination. This makes them suitable for cleanroom environments such as those found in semiconductor manufacturing.

Ultra High Precision: The surface averaging effect in air bearings leads to low error motions, offering superior accuracy and precision. This is crucial in applications such as metrology, micro-manufacturing, and high-precision machining.

Enhanced Stiffness: Some air bearing designs, like the OAV Roller Air Bearing, offer exceptional stiffness, enabling them to resist deformation under load. This translates to greater load capacities and improved operational stability.

Low Error Motions: In air bearings, microscopic surface irregularities get averaged out due to the cushion of air between the bearing surfaces. The air film, with its finite thickness, creates a smoothing or averaging effect over the surface imperfections, meaning that small-scale surface deviations have a lesser impact on the system's overall motion. This significantly reduces error motions such as runout, pitch, and yaw, contributing to the superior precision and accuracy offered by air bearings. This surface averaging effect in air bearings enables them to deliver high precision even when the surfaces are not perfectly smooth or when the bearing experiences dynamic loads. Consequently, air bearings are exceptionally well-suited for applications where precision is critical, such as semiconductor manufacturing, optical systems, high-speed machining, and metrology, among others.

1.2 Limitations of Traditional Bearing in Spindle Systems:

Contact bearings have long been utilized in spindle systems, with their design and function largely remaining consistent. However, despite their widespread use, contact bearings face several limitations, especially when high precision, high speed, and long lifespan are required. These limitations include:

Friction: Contact bearings have internal moving parts that are in physical contact, which leads to friction. This friction generates heat, which can cause thermal expansion and alter the bearing's dimensional stability, reducing its precision.

Thermal Stability: High rotational speeds can cause heat generation, which can lead to thermal expansion, affecting the accuracy of the spindle.

Wear and Tear: Over time, the continuous physical contact within the bearing can lead to wear and tear, impacting its performance and lifespan. This necessitates regular maintenance and replacements, increasing the total cost of ownership.

Noise and Vibration: Due to the physical contact within the bearing, mechanical noise and vibration can occur. These factors can negatively impact the accuracy and precision of spindle operations, particularly in delicate or micro-precision applications.

Speed Limitations: Friction not only generates heat but also limits the maximum rotational speed of the spindle. High-speed operations can exacerbate wear, noise, and vibration issues, and can also lead to premature bearing failure.

Error Motions: In contact bearings, minute surface irregularities can lead to substantial errors in motion, as the direct contact can translate these imperfections into the motion of the assembly.
Lubrication Needs: Contact bearings require regular lubrication to reduce friction and cool the system. This introduces additional maintenance needs and potential sources of contamination, especially problematic in cleanroom environments such as those found in semiconductor manufacturing.
Stiffness: Contact bearings might not provide sufficient stiffness for certain applications, particularly those requiring high load capacities.

II. Novel Design Modifications and Integration Strategies for Air Bearings in Spindle Systems

To address these limitations, this study introduces the innovative OAV product which includes OAV's Roller air bearing, Thrust Air Bearing, Tapered Air Bearing design and Foil Air Bearings promises to revolutionize spindle technology. Each of these air bearings brings unique advantages and characteristics that could substantially improve spindle performance in various applications.
A key aspect of these innovative products is their ease of integration into existing systems. These clever design solutions ensure straightforward installation, minimizing setup times and the need for specialized expertise. This feature makes the transition to these advanced air bearing solutions more feasible and less disruptive to current operations.

2.1 OAV Roller Air Bearing:

OAV Roller Air Bearings are indeed an innovative solution, offering high stiffness and excellent geometric performance. The underlying design principle hinges on the preloading of both horizontal and vertical surfaces with opposing thin film pressures. This mechanism aids in maintaining an optimal gap, ensuring the highest degree of precision. It is designed for easy installation and enhances thermal stability.
Indeed, Roller Air Bearing sizes are similar to the design of traditional roller contact bearings, but, crucially, it operates without physical contact between surfaces.

(2)
The virtual elimination of friction means there is negligible wear, extending the operational life of the bearings and reducing maintenance needs.
"By replacing the traditional roller bearing at the fulcrum of the dual rigid pendulum test assembly with the OAV Air Roller Bearing, Jorge was able to overcome the hurdle presented by traditional bearings in collecting quality test data. "friction has a large effect on energy measurement at these scales (micro-joules) and the amount of energy measured using the OAV air bearings is at least six times greater than when we used traditional ball bearings." (3)
Another pivotal feature of Roller Air Bearings is their ease of installation. Traditional contact bearings often require complex procedures for installation and alignment to avoid premature failure and maintain precision. In contrast, Roller Air Bearings are designed for straightforward installation, thus reducing setup times and the need for specialized expertise.
The high stiffness of OAV Roller Air Bearings is predominantly attributed to their unique surface design. The design enables equal distribution of air and preload forces over the entire bearing surface. This results in not just increased stiffness, which is crucial for resisting deformation under load, but also improved bearing stability and load capacity.
Moreover, the balanced distribution of thin film pressure minimizes variations in the air gap, preserving the bearing's geometric integrity.
The strategic preload application on both vertical and horizontal surfaces effectively counters any external or asymmetrical forces. It also negates any tilting or wobbling that could impair the bearing's precision. The technology's inherent capability to uniformly distribute air and preload across the bearing surface culminates in unparalleled stiffness and maximized performance, redefining the benchmarks of precision bearing in spindle applications.

2.2 OAV Thrust Air Bearing:

The Thrust Air Bearing indeed marks a significant milestone in the realm of air bearings in spindle technology. Its unique feature lies in its integrated design that allows for frictionless operation on a three-way active surface. This innovative capability not only enhances its versatility but also broadens the range of its potential applications.

The OAV Thrust Air Bearing's design allows it to be mounted on standard-sized shafts and face collars, simplifying its integration into various mechanical systems. It delivers fixed spindle motion along the shaft, offering high precision in applications where speed, precision, cleanness is critical. By supporting frictionless three-way motion—rotational and linear—on standard-sized shafting, it offers an unprecedented level of precision and versatility, all while at ultra high speed , minimizing friction and enhancing precision and durability. This advancement holds the promise to revolutionize diverse applications across industries.

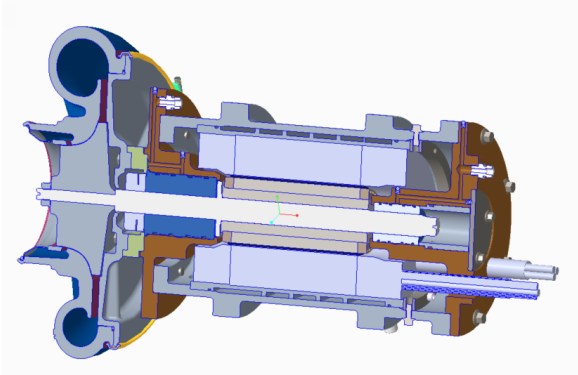

(4)

2.3 OAV Tapered Air Bearing:

The Tapered Air Bearing combines the principles of aerostatics and aerodynamics, ensuring a high load capacity while maintaining high rotational speeds and improved thermal stability. Its innovative design allows for easy installation, reducing the complexity often associated with traditional air bearings. These innovations collectively offer a significant breakthrough in spindle technology, reducing performance degradation often observed in high-speed operations due to heat generation. This marks a considerable leap forward in the field of precision engineering and high-performance applications.

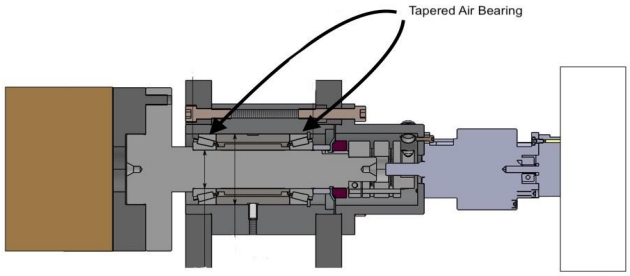

(5)

Tapered Air Bearing shares many of the design principles with a conventional tapered roller bearing but leverages the advantages of being an air bearing, including the absence of physical contact between surfaces.

Conventional tapered roller bearings have a design that allows them to handle both radial and axial loads. This is achieved by incorporating conical rollers that align with a matching, taper-shaped inner ring. However, even with perfect manufacturing and alignment, these contact-based systems can generate significant friction, particularly at high speeds, resulting in wear and heat generation.

On the other hand, Tapered Air Bearings function on the same principle of providing excellent radial and axial load handling but do so without physical contact. Instead, they maintain a thin film of air between the bearing and the load. This principle eliminates virtually all friction, which is a fundamental requirement for high-speed operations.

Tapered Air Bearings, with their combination of high-speed performance, and improved thermal stability, offer an ideal solution for replacing conventional bearings in applications that demand precision and efficiency.

2.3 Aerodynamic Foil Air Bearing:

Aerodynamic Foil Air Bearings represent a significant leap in bearing technology, and their unique design brings a host of benefits for various high-speed applications: OAV Foil Air Bearings use a flexible, compliant foil element to create an air cushion that can support rotating elements with very low friction. They are particularly beneficial in high-speed, high-load, or high-temperature applications where traditional bearing solutions struggle.

Self-Acting Design: Foil air bearings are self-acting, meaning they generate their own pressurized air film as the shaft's rotational speed increases. This eliminates the need for an external pressurization system, simplifying the

overall system design and reducing energy consumption.

High-Speed Operation: Given their self-acting nature, foil air bearings are especially well-suited to high-speed applications. They can operate at speeds that far exceed the capabilities of traditional bearings, making them an excellent choice for high-speed turbines, compressors, and spindles.

Excellent Durability: Foil air bearings are incredibly robust and can endure harsh operating conditions, including high temperatures and heavy loads. The absence of contact between the bearing surfaces reduces wear and tear, significantly extending the bearing's lifespan.

No Lubrication Required: Since there's no direct contact between the moving parts, foil air bearings do not require lubrication. This makes them maintenance-free, reduces the risk of contamination, and makes them suitable for applications where lubrication is undesirable or impractical.

High Load Capacity: Foil air bearings can support high radial loads, thanks to the flexible nature of the foil that conforms to the shaft's surface. This adaptability allows the bearings to distribute the load over a larger surface area, increasing their load-carrying capacity.

Tolerant of Surface Imperfections: Foil air bearings can tolerate some degree of surface imperfections and misalignment, thanks to the compliant nature of the foil. This makes them less sensitive to installation errors or operational conditions that might cause misalignment.

Low Noise and Vibration: Foil air bearings operate with minimal noise and vibration due to the lack of mechanical contact and rolling elements. This makes them ideal for precision applications where noise and vibration could affect the system's performance. The advanced design of aerodynamic foil air bearings offers significant advantages in terms of speed, durability, load capacity, and operational efficiency. These benefits make them an attractive option for many high-performance applications, promising to drive innovation in various fields.

III. Adaptive feedback control system: To further enhance the performance of air bearings in spindle systems, this study introduces an adaptive feedback control system specifically designed to optimize air gap uniformity.

The air gap, the small space filled with pressurized air between the bearing and the shaft, is one of the most critical factors affecting the performance of an air bearing. The stability and precision of the system are highly dependent on maintaining a consistent and uniform air gap.

However, maintaining a consistent air gap can be challenging due to variations in load, speed, and external disturbances. This is where the adaptive feedback control system comes into play.

The adaptive feedback control system constantly monitors the air gap in real-time using non-contact displacement sensors. These sensors can precisely measure the distance between the bearing and the shaft and feed this information back to a control unit.

The control unit uses this information to adjust the pressure of the air supply in real-time. If the sensors detect a deviation from the desired air gap, the control system will either increase or decrease the air pressure to correct the gap accordingly.

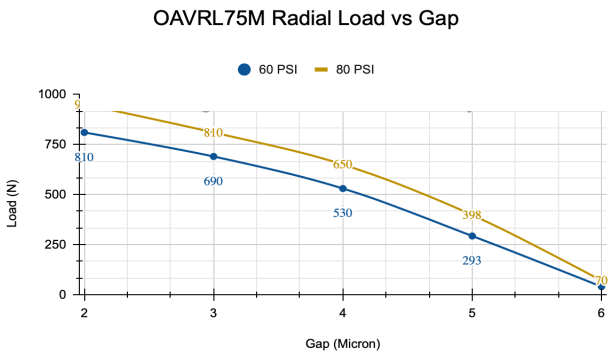

6)

To ensure optimal performance, the control system uses an adaptive algorithm that can learn from the system's behavior. The algorithm can adjust the system's responses based on past performance, ensuring the system quickly and accurately corrects any deviations from the desired air gap.

This approach ensures the air gap remains uniform, even under varying operating conditions. It helps to reduce error motions, enhances system stability and allows the air bearing to maintain its high precision, irrespective of changes in load or speed.

In conclusion, the adaptive feedback control system represents a significant innovation in air bearing technology. By continuously monitoring and adjusting the air gap, it ensures consistent, high-precision performance of air bearings in spindle systems under all operational conditions.

IV. Potential challenges: Despite the clear benefits and advancements that air bearings bring to high-performance spindle systems, several potential challenges might hinder their large-scale adoption. These include cost factors, specialized maintenance requirements, and the need for comprehensive training. However, these hurdles can be effectively addressed with well-planned strategies.

Cost Factors: Initially, the acquisition cost of air bearings can be higher than conventional bearings due to the advanced technology involved. But it's crucial to consider the total cost of ownership, which includes maintenance, replacement, and downtime costs over the system's life. Air bearings' extended lifespan, reduced maintenance, and lower downtime can lead to cost savings in the long run.

Specialized Maintenance and Training : While air bearings require less maintenance compared to contact bearings, they may require specialized procedures when maintenance is necessary. This can be addressed by developing standardized maintenance protocols and ensuring that these protocols are easily accessible and understandable. Adopting air bearing technology may require training for engineers, operators, and maintenance personnel to understand the new systems' workings. To facilitate this, manufacturers should provide comprehensive training materials.

Integration Challenges: The integration of air bearings into existing systems may present design and compatibility challenges. To overcome this, manufacturers should provide detailed integration guides, and if possible, customizable design solutions that can be adapted to fit various applications.

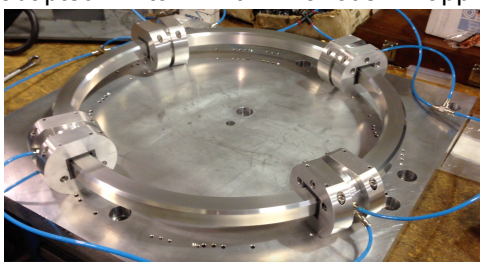

(7)

By addressing these potential challenges, we can foster a roadmap for the successful integration of air bearing technology into high-performance spindle applications. With ongoing advancements and a well-planned approach to adoption, air bearings stand poised to redefine the future of precision in spindle technology.

ACKNOWLEDGEMENTS:

We wish to express our sincere gratitude to the entire team at OAV Air Bearings for their invaluable support and technical insights throughout this study. Their expertise and commitment to advancing air bearing technology have been instrumental in shaping this research.

We are also profoundly grateful to our academic and industry peers for their constructive feedback, which has significantly enriched our understanding and approach.

Lastly, we would like to acknowledge all the researchers and pioneers in the field of spindle technology and air bearings whose work has laid the foundation for our study.

Please note that any errors or omissions in this study are solely the responsibility of the authors.

(1) Coefficient Friction Data for OAVTB60i20 Thrust air Bearing

(2)Image of an Externally Spinning Roller Bearing Denoted as OAVRL13MX

(3)Jorge, J. F., Bergbreiter, S. and Patek, S. N. (2021). Pendulum-based measurements reveal impact dynamics at the scale of a trap-jaw ant. J Exp Biol jeb.232157.

(4)Example setup for a Thrust Bearing Spindle, denoted as OAVTB60i25

(5)Illustrative Configuration for an Oppositely Pre-loaded Taper Air Bearing

(6) Detail analysis of radial gap versus the load applied, denoted as OAVRL75M.

(7)Example Configuration for a Large Diameter Spindle.

LEVCUBE: A SIX-DEGREE-OF-FREEDOM MAGNETICALLY LEVITATED NANOPOSITIONING STAGE WITH CENTIMETER-RANGE XYZ MOTION

Ian Heyman, Lei Zhou
Walker Department of Mechanical Engineering
The University of Texas at Austin, TX, USA

INTRODUCTION

Precision motion stages are a critical component in a wide range of manufacturing equipment and scientific instruments, including photolithography scanners [1], micro-scale additive manufacturing and machine tools [2, 3], and microscopes [4]. Precision positioning stages can be categorized by their bearing mechanisms into four groups: mechanical bearing stages, air bearing stages, flexure-based stages, and magnetically levitated stages. Mechanical bearing stages are the most widely-used type due to their advantages of high stiffness, low cost, and ruggedness [5]; however, the highly nonlinear pre-sliding friction from the bearings can impair the stage's accuracy and dynamic performance [6, 7]. The other three stage types can all provide non-contact motion and thus eliminate bearing friction. However, flexure stages are not suitable for long-stroke motions, and air bearings can not be used in vacuum environments which limits their applicability for long-stroke and in-vacuum motion tasks.

Among various types of precision motion stages, magnetically levitated stages, where the moving stage is supported by magnetic forces and without mechanical contact, provide the advantages of frictionless motion, vacuum compatibility, and contamination-free motion. In addition, in magnetically levitated precision stages, the same actuator units can be used for levitation and thrust force generation, and the positioning accuracy of the system is entirely determined by the sensing units, which offer excellent potential to provide parasitic-free motion and compact system designs. These advantages of magnetically levitated precision stages offer excellent positioning capabilities and make these stages highly desirable for various precision machines and instruments. However, most prior magnetically levitated stage designs primarily focus on short-stroke (i.e. < 3 mm) motion in all axes [8–13] or only offer long-stroke motion in linear or planar DOFs [14–21], as illustrated in Fig. 1 and summarized in [22]. These designs are not suitable for applications that require large-stroke (i.e., greater than 5 mm) micro/nano-positioning in all translational DOFs, such as X-ray microscopic scanning for large-size samples [4] and micro-scale machining and additive manufacturing [23]. Recently, several commercial magnetically levitated motion solutions including XBox$^{\mathrm{TM}}$ from Planar Motors [24] and ctrlX FLOW$^{6\mathrm{D}}$ from Bosch Rexroth [25] have been released, which offer unlimited planar motion stroke and up to 20 mm stroke in height and are highly valuable for future flexible automation applications. However, in these designs based on [14] and [16], the levitation force in the vertical direction strongly depends on the vertical displacement of the stage,

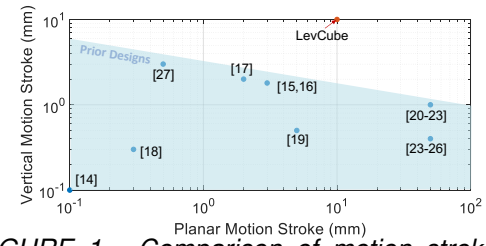

FIGURE 1. Comparison of motion stroke between prior magnetically levitated precision stage publications and this work, the LevCube.

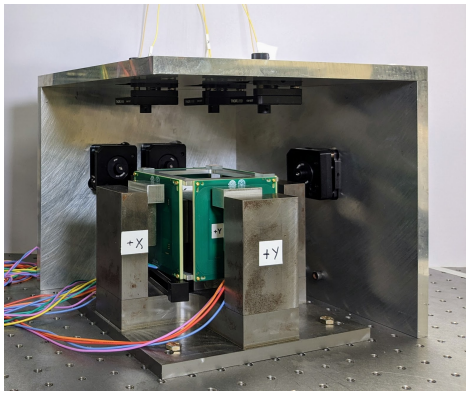

FIGURE 2. Photograph of LevCube: a magnetically levitated nanopositioning stage with long-stroke translation in XYZ DOFs.

which can create control challenges when high-precision scanning motion is required in the vertical direction. There is a critical need to create novel magnetically levitated precision stage designs with a large motion range in all translational DOFs and with low position-dependency in force generations to provide the required positioning capability for these target applications.

Aiming to address this challenge, this paper presents the design, modeling, prototyping, and preliminary experimental evaluations for a new type of magnetically levitated precision stage, which we call LevCube, that can offer a motion stroke of up to 10 mm in all translational DOFs, as is shown in Fig. 2. The LevCube system presents a novel magnetic design with a stator generating uniform homopolar magnetic fields across large air gaps of approximately 20 mm, and actuator coils arranged on the motion stage to allow for active control of the stage's levitation and motion via Lorentz forces. Such a magnetic design enables largely uniform force generation on the stage over 10 mm motion stroke. The maximum force of the LevCube stage is 25.5 N under 3.5 A current amplitude, which can generate a stage acceleration of 2.5 g, i.e., 2.5 times the gravitational acceleration. The prototype stage was successfully levitated with a control bandwidth of 100 Hz in the translational DOFs and 70 Hz in the rotational DOFs. These results show promise for the proposed design to achieve excellent positioning performance over a 10 mm motion stroke in all translational DOFs.

This abstract presents the design and prototyping for a novel long-stroke, high-speed XYZ maglev precision positioning stage shown in Fig. 2. Our proposed stage presents a magnetic design with a stator which generates uniform magnetic field in a large air gap of around 10 mm, and uses Lorentz force for active control of magnetic levitation and motion. Such a magnetic design can provide uniform force generation over long-stroke displacement, which simplifies the controller design needed to achieve high motion performance. We have constructed a prototype maglev stage according to the design. Finite element (FE) simulation results validate the proposed stage design.

STAGE OPERATING PRINCIPLE AND DESIGN

Figure 3 illustrates the magnetic design of the LevCube system, where Fig. 3a shows a diagram of the stage's magnetic structure, and Fig. 3b shows a cross-section diagram of the stage with

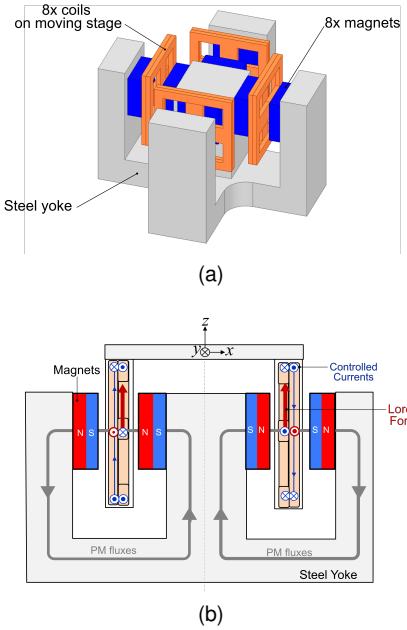

FIGURE 3. Operating principle of the proposed LevCube stage. (a) Concept diagram. (b) Cross-section diagram of magnetic design.

magnetic fluxes and forces indicated. As is shown in Fig. 3, the stator assembly consists of a steel yoke with eight permanent magnets (PMs) attached, where the magnets are all magnetized in the radial direction outward from the center of the stator yoke. With such a magnetic design, the stator creates a largely uniform magnetic field in the four air gaps, as shown in Fig. 3b. The moving stage contains eight coils excited by independently-controlled currents, with two coils arranged perpendicularly in each side surface of the moving stage. Each coil consists of a central wire branch and two loops of wire for returning current. This coil design enables Lorentz forces to be generated only on the central wire branch, as the two loops of wire for returning current are located outside of the magnetic air gap. When the coils are energized with currents (blue lines in Fig. 3b), Lorentz forces (red arrows in Fig. 3b) can be generated to the stage to actively stabilize the stage's suspension and precision positioning in all six DOFs.

We have constructed a prototype for the LevCube design as shown in Fig. 2b. The stage prototype comprises a stator assembly, a moving stage, a metrology frame, and a feedback control system.

EXPERIMENTAL EVALUATIONS

To evaluate the effectiveness of the decoupling between different DOFs, the frequency re-

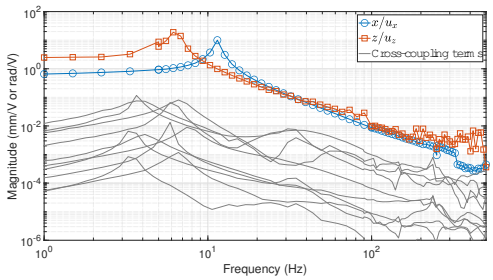

FIGURE 4. Experimentally measured plant frequency responses of the decoupled DOFs and the cross-coupling terms. x/u_x: plant dynamics in x-direction. z/u_z: plant dynamics in the z-direction. Grey: cross-coupling terms.

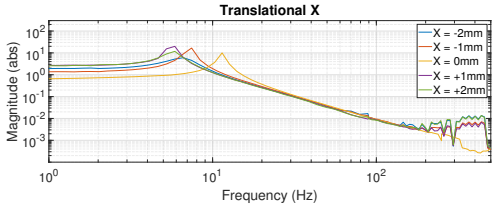

(a)

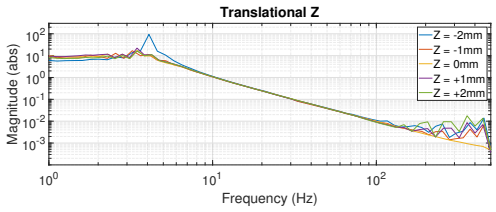

(b)

FIGURE 5. Experiemntally measured plant frequency responses of the stage under varying displacements. (a) x-axis plant dynamics under x-directional displacement. (b) z-axis plant dynamics under varying z-directional displacement.

sponses of the stage's plant dynamics are measured between various input and output signals. Fig. 4 shows the measured frequency response in the decoupled x- and z-directions as well as their cross-coupling terms, with the current command signals being the input, and measured stage displacement being the output. The stage's dynamics in the y-direction are similar to that in the x-direction due to symmetry and are not presented. Here the cross-coupling terms include both translational and rotational DOFs, such as θ_z/u_x, θ_y/u_x, y/u_x, and z/u_x. Note that these measurements must be conducted with the control loops closed, as the magnetic levitation system is unstable in the open-loop condition. During the frequency response measurement, controllers with lower bandwidth (approximately 40 Hz) are used to achieve a larger signal-to-noise ratio. It can be observed that the frequency response data of x/u_x and z/u_z in Fig. 4 show a slope of -2 (or -40 db/dec) in the high-frequency range, which agrees with the force-to-displacement relationship of the stage. This observation indicates that the control effort signals u_x and u_z are proportional to the force generated to the stage in the corresponding directions. In the low-frequency range (i.e., below 10 Hz), the system's dynamics behave like a stiffness. This is due to the stiffness of the cables connecting to the coils on the moving stage. Comparing the frequency response signals in the x- and z-directions to those in the cross-coupling terms, it can be seen that the signals of the decoupled terms are 1-2 orders of magnitude larger than that of the cross-coupling terms in the frequency range below 100 Hz, demonstrating that the stage's dynamics in various DOFs are well decoupled. In addition, it can be observed that several cross-coupling frequency response data demonstrate resonances and anti-resonances around 30-40 Hz. To our understanding, this is due to the closed-loop dynamics of the rotational DOFs being added to the measured dynamics. With the actuation forces and measurements not aligned with the center of stiffness of the stage, rotational motion can be excited when the stage accelerates in the translational DOFs. Further design optimization for sensor locations will be conducted in our future work to optimize the stage's motion performance.

To evaluate the position dependency of the stage's dynamics, the system's plant frequency responses in the x- and z-directions at different positions are measured, as shown in Fig. 5. It can be seen that the system's dynamics in the frequency range above 10 Hz do not have strong position dependency, but the dynamics in the low-frequency range can change when the stage displaces in the x direction. To our understanding, this is due to the fact that the cable's stiffness may vary as the stage displaces in the lateral directions. In addition, the measured frequency response data in Fig. 5 are noisy above 200 Hz. This is due to the low signal-to-noise ratio in the frequency response measurement at the high-frequency range.

After establishing the plant response and validating the actuator performance, the loop-shaping technique is used to design the controller parameters for the stage's levitation in the decou-

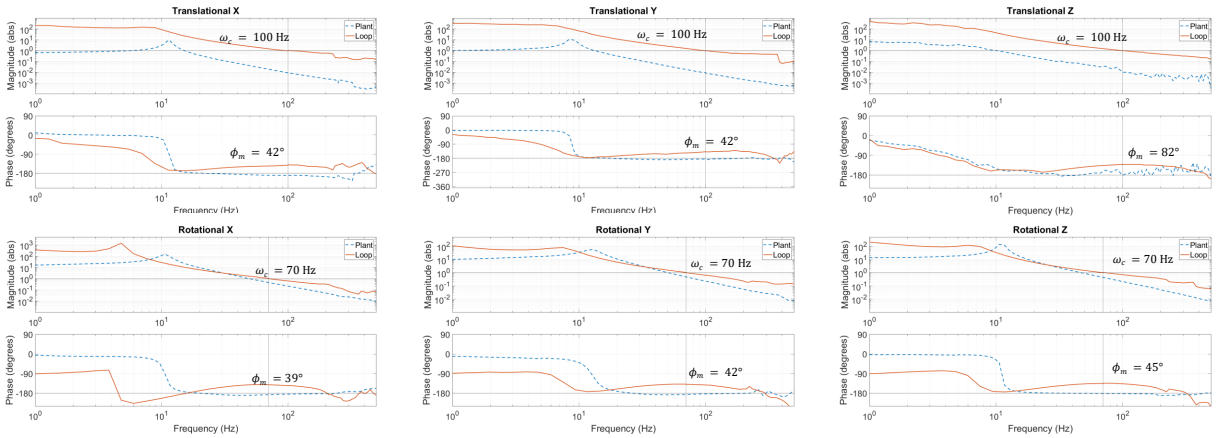

FIGURE 6. Experimentally measured plant and loop frequency response of the LevCube system in the decoupled DOFs.

pled DOFs. Figure 6 shows the experimentally-measured plant and loop frequency responses of the stage in all controlled DOFs, where the blue dotted line represents the plant response, and the orange solid line represents the loop gain. Data show that the stage's position control loop in each DOF was successfully tuned to achieve a bandwidth of 100 Hz in the translational axes and 70 Hz in the rotational axes, and a phase margin of approximately 40 degrees is achieved in all DOFs. These performance satisfy our design target. Note that the cross-over frequency of the rotational DOFs is selected to be lower than that of the translational DOFs to avoid motion error due to the amplification of the cross-coupling terms, as the rotational closed-loop dynamics can be added to the cross-coupling terms.

To evaluate the dynamic positioning error of the stage prototype, position sensor data were taken over a five-minute period while the stage was levitated at the neutral position, and Fig. 7 shows the position error histogram and spectrum. Data show that the standard deviation of the positioning error is approximately 30 nm. With the sensor resolution being 10 nm, the achieved dynamic error is sufficiently small which demonstrates the control system's performance. The spectrum data in Fig. 7 show that the frequencies of the maximum error are at 20 Hz and 80-100 Hz. To our understanding, the low-frequency component is due to the floor vibration transmitted to the stage via cables, and the high-frequency peaks are due to the stage's control bandwidth.

Fig. 8 shows the trajectory tracking test of the LevCube prototype. In these tests, second-order

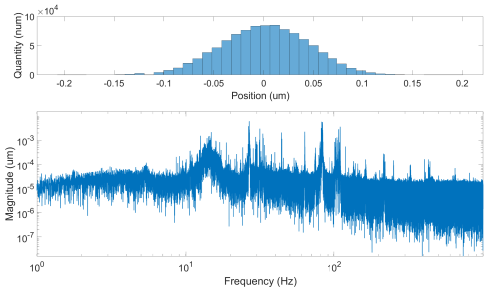

FIGURE 7. Stage position error histogram and spectrum.

polynomial trajectory profiles with different velocities are used, and the acceleration being used is 2 g. In these tests, the feedforward controllers were not active since they were not highly effective in reducing the error in the acceleration phases. To our understanding, it is because the cable's dynamics (stiffness and friction) are not included in the feedforward controllers. It can be observed that the stage's tracking error during the constant-velocity motion is below 1 μmfor 1 mm/s motion and below 10 μm for 7 mm/s motion, and a relatively large tracking error can be seen during the stage's acceleration/deceleration phases. To our understanding, this error is primarily due to the drag force induced by the cables and the quantization of the sensor signals (after being amplified by the lever arms). In our future work, we will improve the stage's design to reduce the cable's impact to the system dynamics, and will improve the feedforward controllers to reduce the stage's tracking error.

CONCLUSIONS AND FUTURE WORK

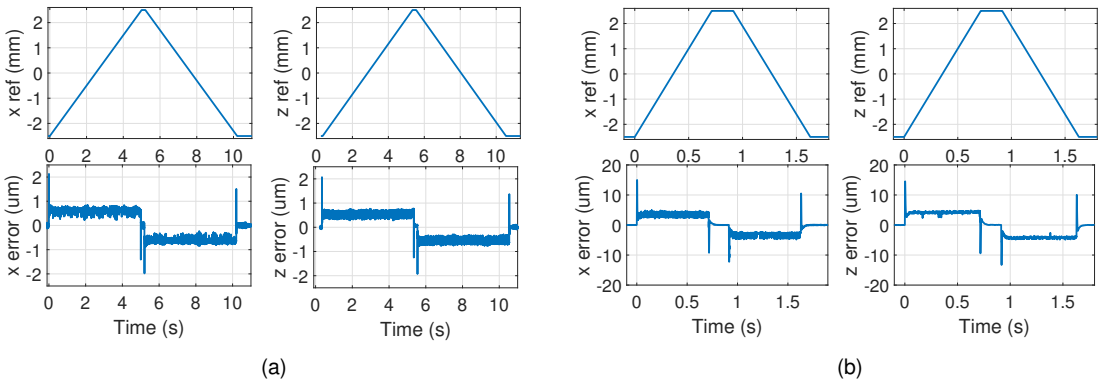

FIGURE 8. x and z-directional trajectory tracking performance of the LevCube prototype. (a) Trajectory with $1\ \mathrm{mm/s}$ speed and 2 g acceleration. (b) Trajectory with $7\ \mathrm{mm/s}$ speed and 2 g acceleration.

In this paper, the design of a new type of magnetically levitated positioning stage is presented. The stage design uses Lorentz actuators with large air gaps in the stator assembly, and the uniformity of the magnetic field strength in the gap is validated by both FE simulations and experimental measurements. Laser interferometers are used for feedback to provide high-resolution positioning performance. With a sensor resolution of 10 nm, the positioning error of the stage has a standard deviation of 30 nm. The stage also demonstrates a tracking error of below 1 um under the target motion trajectory. These results show that the LevCube prototype is able to successfully levitate the moving stage with sufficient bandwidth and positioning capabilities.

REFERENCES

[1] van Schoot J, Troost K, Bornebroek F, van Ballegoij R, Lok S, Krabbendam P, et al. High-NA EUV lithography enabling Moore's law in the next decade. In: International Conference on Extreme Ultraviolet Lithography 2017. vol. 10450. SPIE; 2017. p. 109–128.

[2] Masuzawa T. State of the art of micromachining. CIRP Annals. 2000;49(2):473–488.

[3] Roy NK, Behera D, Dibua OG, Foong CS, Cullinan MA. A novel microscale selective laser sintering (μ-SLS) process for the fabrication of microelectronic parts. Microsystems & Nanoengineering. 2019;5(1):1–14.

[4] Deng J, Preissner C, Klug JA, Mashrafi S, Roehrig C, Jiang Y, et al. The Velociprobe: An ultrafast hard X-ray nanoprobe for high-resolution ptychographic imaging. Review of Scientific Instruments. 2019;90(8):083701.

[5] Altintas Y, Verl A, Brecher C, Uriarte L, Pritschow G. Machine tool feed drives. CIRP Annals. 2011;60(2):779–796.

[6] Dong X, Yoon D, Okwudire CE. A novel approach for mitigating the effects of pre-rolling/pre-sliding friction on the settling time of rolling bearing nanopositioning stages using high frequency vibration. Precision Engineering. 2017;47:375–388.

[7] Yoon JY, Trumper DL. Friction modeling, identification, and compensation based on friction hysteresis and Dahl resonance. Mechatronics. 2014;24(6):734–741.

[8] Holmes M, Trumper D. Magnetic/fluid-bearing stage for atomic-scale motion control (the angstrom stage). Precision Engineering. 1996;18(1):38–49.

[9] Shan X, Kuo SK, Zhang J, Menq CH. Ultra precision motion control of a multiple degrees of freedom magnetic suspension stage. IEEE/ASME Transactions on Mechatronics. 2002;7(1):67–78.

[10] Kuo SK, Shan X, Menq CH. Large travel ultra precision $x - y - \theta$ motion control of a magnetic-suspension stage. IEEE/ASME Transactions on Mechatronics. 2003;8(3):334–341.

[11] Zhang Z, Menq CH. Six-axis magnetic levitation and motion control. IEEE Transactions on Robotics. 2007;23(2):196–205.

[12] Verma S, Kim Wj, Shakir H. Multi-axis maglev nanopositioner for precision manufacturing and manipulation applications. IEEE Transactions on Industry Applications. 2005;41(5):1159–1167.

[13] Kim Wj, Verma S, Shakir H. Design and precision construction of novel magnetic-levitation-based multi-axis nanoscale positioning systems. Precision Engineering. 2007;31(4):337–350.

[14] Kim Wj. High-precision planar magnetic levitation. Ph D Thesis. 1997;p. 6730.

[15] Jansen J, Van Lierop C, Lomonova EA, Vandenput AJ. Magnetically levitated planar actuator with moving magnets. IEEE Transactions on Industry Applications. 2008;44(4):1108–1115.

[16] Lu X, et al. 6D direct-drive technology for planar motion stages. CIRP Annals. 2012;61(1):359–362.

[17] de Klerk AC, Angelis GZ, van Eijk J. Design of a next generation 6 DoF stage for scanning application in vacuum with nanometer accuracy and mGauss magnetic stray field. In: Proceedings of the 19th ASPE Annual Meeting. Citeseer; 2004. p. 60–63.

[18] Zhou L, Trumper DL. Magnetically Levitated Linear Stage With Linear Bearingless Slice Hysteresis Motors. IEEE/ASME Transactions on Mechatronics. 2020;26(2):1084–1094.

[19] Takahashi M, Ogawa H, Kato T. Compact maglev stage system for nanometer-scale positioning. Precision Engineering. 2020;66:519–530.

[20] Schaeffel C, Katzschmann M, Mohr HU, Gloess R, Rudolf C, Mock C, et al. 6D planar magnetic levitation system-PIMag 6D. Mechanical Engineering Journal. 2016;3(1):15–00111.

[21] Anthis A, Trumper D, Hamer T. Design and Verification of a Planar, Flux-Steering Magnetic Actuator. In: Proceedings of the 36th ASPE Annual Meeting; 2021. .

[22] Zhou L, Wu J. Magnetic Levitation Technology for Precision Motion Systems: A Review and Future Perspectives. International Journal of Automation Technology. 2022;16(4):386–402.

[23] Saha SK, Wang D, Nguyen VH, Chang Y, Oakdale JS, Chen SC. Scalable submicrometer additive manufacturing. Science. 2019;366(6461):105–109.

[24] Planar Motor Inc.;. Accessed: March 2023. https://www.planarmotor.com/index.html.

[25] ctrlX FLOW: Everything in the flow: Intralogistics solutions for the smart factory;. Accessed: March 2023. https://apps.boschrexroth.com/microsites/ctrlx-automation/en/portfolio/ctrlx-flow/.

A NEW FULL-FIELD IMAGING PROJECTION MICROSCOPE FOR THE APS UPGRADE AT 32-ID

Alberto Mittone[1], Viktor V. Nikitin[1], Sunil Bean[1], Vincent De Andrade[2], Alex Deriy[1], Kamel Fezzaa[1], Curt Preissner[1], Deming Shu[1] and Francesco De Carlo[1]

[1]Advanced Photon Source
Argonne National Laboratory
Lemont, IL, USA
[2]KLA Corporation
Hayward, CA, USA

INTRODUCTION

The Advanced Photon Source is currently in the midst of a machine upgrade (APS-U). As a part of the beamline enhancement program, a nano-computed tomography projection microscope (n-CT) is being developed for the 32-ID beamline sector [1]. By combining the new n-CT together with the future APS-U source new imaging capabilities will be available at 32-ID. Specifically, this new instrument, will fill the resolution gap in between the existing 32-ID Transmission X-ray microscope (TXM) and the micro-tomography stations located at 2-BM and 7-BM, which all part of the imaging group at APS. The proposed instrument will provide a good compromise between high spatial resolution, fast measurements and high dose efficiency.
The instrument makes use of a Kirkpatrick-Baez (KB) optics for the nano-focusing [2,3].
To satisfy the necessary imaging requirements, a sub 10 nanometers thermal and vibrational drift stability between the sample and optics within a 10-minute time range is desired. This selected time range stability is to minimize the need of complicated post-processing image registration procedures.
To achieve a broad range of spatial resolutions, a variable length projection zoom, up to 450 mm, is required. Simultaneously satisfying motions and stability requirements represent a significant engineering challenge due to the constraints of conventional motion mechanics. To address these challenges, the proposed n-CT design incorporates features initially used in the Velociprobe [4], such as the concept of granite air bearings. Many designs at APS [5] and at other synchrotron facilities [6] have incorporated these types of granite stages. By utilizing the granite air bearing concept, along with other design aspects of the instrument, the requirements become reachable. In addition to the granite air bearing concept, the n-CT design also introduces a unique multi-degree of freedom wedge configuration to overcome the constraints imposed by space limitations.

32-ID PROJECTION MICROSCOPE DESIGN

The optical layout and working principle of 32-ID nCT are reported in FIGURE 1.

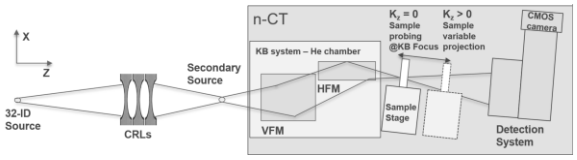

FIGURE 1. Optical layout and working principle of the projection microscope currently under design at the 32-ID sector.

X-rays are generated by mean of an insertion device, and focused by Compound Refractive Lenses (CRLs). A secondary source is achieved upstream the nCT KB optics, while the latter is used for nano-focusing the beam. The sample stage is at a variable distance with respect to the KB system. Multiple degrees of freedom are required at the sample stage level, for a precise positioning of the object under investigation along the three axes and to allow advanced scanning protocols. An air bearing based, high speed, low errors rotary stage, is required to enable performing tomographic measurements at nano-metric resolution. Downstream the sample stage, the beam will reach out the detection system, consisting in a selectable multi-magnification indirect optics (Optique Peter, Lentilly, France), coupled with a dual camera system (Kinetix, Teledyne, Oryx, Flir). A 3D rendering of the entire instrument is reported in FIGURE 2. In this system the x-rays are converted into visible light

by a scintillator screen. The system will allow to remotely choose the most appropriate set of optical lenses and detection camera according to users needs.

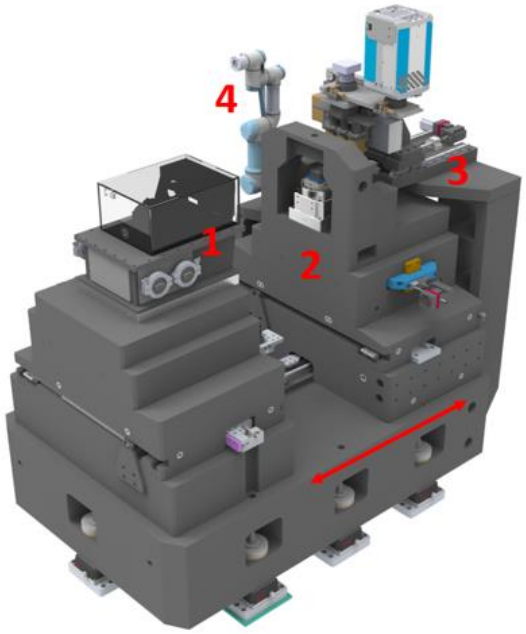

FIGURE 2. Projection microscope design. 1) KB mirrors system, under Helium atmosphere – (X, Y); 2) Sample air bearing positioning stage – (K_x, Y, K_z, K_{Yaw}); 3) Triple magnification dual camera indirect detection system – (K_x, K_y, K_{Yaw}, K_{Pitch}). 4) Support for a robotic arm for automatic sample exchange. The red arrow depicts the motion of the sample positioning assembly.

An overview of the characteristic parameters of the n-CT instrument is reported in TABLE 1:

Parameter	Value	Unit
Imaging techniques		
Target imaging resolution	15	nm
Selectable scan axis	X, Y, θ_y	
Total range of Projection Zoom (K_z)	450	mm
Rotation Scan Range	>360	deg
Rotational step MIM	150	µrad
K_y scan range	≥ 50	µm
K_x' scan range	≥ 100	µm
Planar scan MIM	≤ 2	µm
Relative sample to optics positioning resolution	≤ 10	nm
Relative sample to optics stability	≤ 10, in 10 min	nm
Beam energy	25	keV
Largest volume of interest	80x80x80	µm

*TABLE 1: Parameters of interests of the n-CT instrument. * X-ray holotomography nano-CT; ** X-ray fluorescence nano-CT.*

Details on the KB optics are reported in TABLE 2. The system is composed by a vertically focusing mirror (VFM) and a horizontally focusing mirror (HFM). An overview of the KB assembly is shown in FIGURE 3.

Parameters	VFM	HFM	Unit
Substrate material	Silicon		
Mirror shape	Elliptic		
Clean length	60	40	mm
Clean width	3	3	mm
Mirror length	65	45	mm
Roughness (at 50x)	0.2	0.2	nm (rms)
Tangential slope error	0.1	0.1	µrad (rms)
Tangential figure error (PV)	1	1	nm
Incidence angle*	20	20	mrad
Object distance*	33	33.057	m
Image distance*	0.1395	0.0825	m
Gap between mirrors	2		mm
Optical KB focal spot size	20		Nm
Optical Working distance	60		mm
Coating**	None		

*TABLE 2: KB mirrors specification table. *At mirror center. ** Multilayer coating will be deposited in-house.*

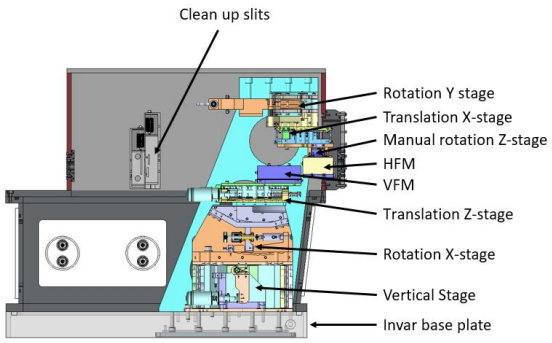

FIGURE 3: n-CT KB assembly.

Mirrors have been provided by the JTEC Corporation, Japan, and their quality characterized as reported in FIGURE 4.

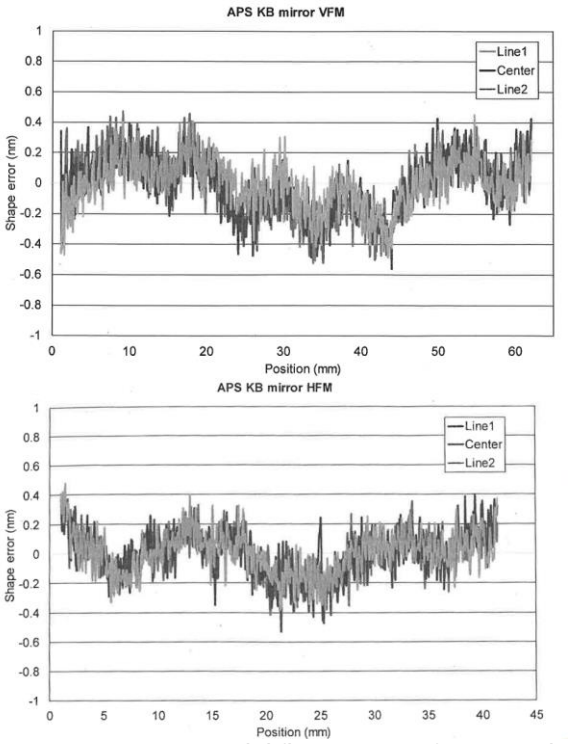

FIGURE 4: Tangential figure error of VFM and HFM mirrors measured at APS.

During the design phase, the following critical requirements have been taken into account:

- KB environment: stable and helium isolated is required to achieve nano-focusing and extend the system lifetime.
- Relative optics to sample thermal and vibrational stability.
- Long range variable projection zoom axis of 450 mm without compromising the stability.
- Possibility to accommodate different sample environments while keeping >360-degree rotational freedom. This includes the integration of voltage biasing and fluid feedthroughs.
- Possibility of implementing multi-modal measurements, as for example x-ray fluorescence.

MOTION DESIGN AND GRANITE SUPPORT

The basic idea of the granite air bearings is to position dynamically pieces of granite by temporarily floating them with air pressure. Once the granite pieces are in place the air is turned off, thus restoring a monolithic structure. The design of the n-CT includes 6 granite pieces, resulting in 2 degrees of freedom for the KB system and 4 for the sample stack. The configuration is reported in FIGURE 5. The KB motions are expected to be used only initially during the commissioning, while the sample motions will be used routinely during users' measurements. In order to cope with the limited space available, a wedge design has been incorporated (2, 3 of FIGURE 3).

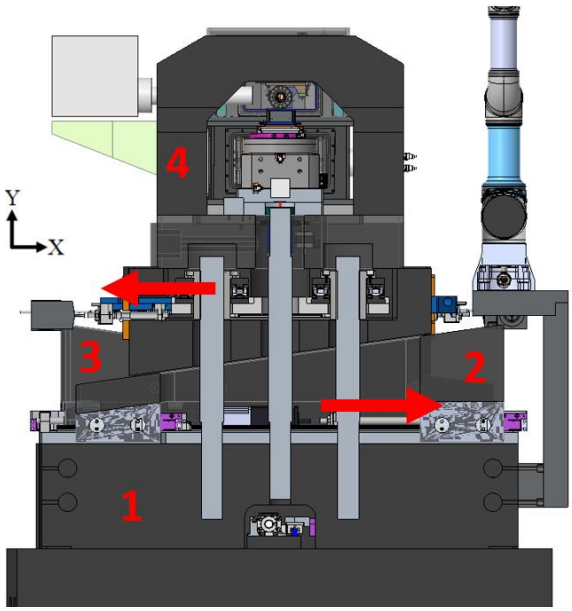

FIGURE 5. n-CT Granite stage stack. 1) Z motion; 2) X driving wedge that creates Y follower motion; 3) Two degree of freedom Y follower wedge with X motion; 4) Z motion gantry for sample environments and detector mounting (XRF). The KB support system has nearly identical blocks 1,2,3.

The sample stack has been designed in order to guarantee a compact continuous rotation. Rotary unions and slip rings are buried in the granite plate. In order to increase user flexibility, the possibility of choosing piezo scanning (with a limited load) or a kinematical mounting interface has been incorporated.
Rotational detuning of sample rotation axis about the X direction of the kicked KB beam (K_x) represents the worst parasitic error for the instrument. Considering the working distance and expected pixel size, it is desired to keep this value below 1000 µrad. Granite guiding mechanics and form for positional repeatability will contribute to parasitic errors. The worst-case scenario has

been considered and resulting detuning error estimated being 173 µrad.

MODAL ANALYSIS AND THERMAL CONSIDERATIONS

In order to determine if the natural frequency of the both the instrument support and staging is above the 30 Hz noise floor of APS a modal analysis has been performed [8]. The pre-loaded n-CT jack stiffness used to define the 8 floor interfaces is reported in TABLE 3. Granite stages and supporting structure are sufficiently stiff to avoid amplifications of the vibrations. The first mode is a KB frame motion (~158 Hz). In the probing and farthest projection positions the second natural frequencies are ~179 Hz and ~172 Hz respectively.

K_{xx} (N/m)	1.14E9
K_{yy} (N/m)	2.31E9
K_{zz} (N/m)	1.15E9
$K_{\theta X}$ (N/m)	2.32E6
$K_{\theta Y}$ (N/m)	4.79E6
$K_{\theta Z}$ (N/m)	5.42E6

TABLE 3: n-CT jack stiffness. The load (N) is 60000. Empirical tested values obtained at APS.

Both the sample stack and KB optics are mounted on nearly identical stage platforms, leading to the same response to environmental changes. While the KB system is enclosed in a He environment, the sample stage is in air. The major contribution of thermal drift is expected to occur relatively between these two systems. From simplified lumped thermal simulations, in which no spatial dependence has been considered, given a 0.2 ºC change it has been estimated that the thermal response time to 10 nm of the sample stack is ~6 minutes. By installing additional protections from convectional motions (Lexan panel) it is expected that the system will not respond more than 10 nm over a 10-minutes time range.

IMAGE CONTRAST, DATA PROCESSING AND APPLICATIONS

Thanks to its design, users will be able to work at different spatial resolutions, ranging continuously from 50 to 500 nm at the beginning of the operations, aiming at reaching 15 nm as highest resolution in future, by moving the sample along the direction of beam propagation. The instrument's design includes the potential to incorporate a fluorescence detector and to integrate various sample environments for multi-technique measurements and in-situ/in-operando studies. In addition to the traditional single-distance n-CT, users will have the opportunity to employ the holotomography phase-contrast imaging technique. This technique is known for its high sensitivity to low-absorbing materials and superior dose efficiency. For a quantitative retrieval of the refraction properties of the examined sample, images acquired at multiple sample-to-detector distances will be combined, therefore having high stability and repeatability of the system is mandatory. Samples, like those typically found in life sciences, will significantly benefit by this image modality. The relatively high energy used, 25 keV, will ensure sufficient penetration power, even for thicker samples, while mitigating radiation damage. Users will have access to various acquisition protocols, including fly scan, interlaced scan, and tiled tomography.

Data will be reconstructed in near real-time, thanks to the use of highly optimized reconstruction codes. Additional processing tools will include data alignment, motion artifact correction, and 3D visualization and rendering. The instrument is poised to serve multiple user communities, spanning energy science, material science, earth science, and life science.

ACKNOWLEDGEMENTS

This research used resources of the Advanced Photon Source, a U.S. Department of Energy (DOE) Office of Science user facility at Argonne National Laboratory and is based on research supported by the U.S. DOE Office of Science-Basic Energy Sciences, under Contract No. DE-AC02-06CH11357.

REFERENCES

[1] S. Bean et al., “a new ultra-stable variable projection microscope for the aps upgrade of 32-ID”. Mech. Eng. Design of Synchrotron Radiat. Equip. and Instrum. MEDSI2020, Chicago, IL, USA.

[2] D. Shu et al., “Modular nanopositioning flexure stages development for APS upgrade K-B mirror nanofocusing optics,” Mech. Eng. Design of Synchrotron Radiat. Equip. and Instrum. MEDSI2020, Chicago, IL, USA.

[3] D. Shu et al., “Mechanical design of a flexural nanopositioning stage system for hard x-ray nanofocusing at the Advanced

Photon Source 32-ID-C station," Proc. SPIE 11112, X-Ray Nanoimaging: Instruments and Methods IV, p. 111120N, September 2019.
[4] C. A. Preissner et al., "Earth, Wind, and Fire: The New Fast Scanning Velociprobe", in Proc. 9th Mechanical Engineering Design of Synchrotron Radiation Equipment and Instrumentation Int. Conf. (MEDSI'16), Barcelona, Spain, Sep. 2016, pp. 112-115.
[5] C. A. Preissner et al., "A Family of High-Stability Granite Stages for Synchrotron Applications", Mech. Eng. Design of Synchrotron Radiat. Equip. and Instrum. MEDSI2020, Chicago, IL, USA.
[6] R. R. Geraldes et al., "Granite Benches for Sirius X-ray Optical Systems", in Proc. 10th Mechanical Engineering Design of Synchrotron Radiation Equipment and Instrumentation Int. Conf. (MEDSI'18), Paris, France, Jun. 2018, pp. 361-364.
[7] P. Cloetens et al., "Holotomography: Quantitative phase tomography with micrometer resolution using hard synchrotron radiation x rays". Applied Physics Letter, Volume 75, issue 19, 1999.
[8] ANSYS Engineering simulations and 3D design software (2018), www.ansys.com.

DEVELOPMENT OF THE TRANSMISSION X-RAY MICROSCOPE FOR SUB-10 NM RESOLUTION IMAGING

Viktor V. Nikitin[1], Alberto Mittone[1], Vincent De Andrade[2], Alex Deriy[1], Sunil Bean, Michael Wojcik[1], Kamel Fezza[1] and Francesco De Carlo[1]
[1]Advanced Photon Source
Argonne National Laboratory
Lemont, IL, USA
[2]KLA Corporation
Hayward, CA, USA

INTRODUCTION

Transmission X-ray Microscope (TXM) is a full-field X-ray imaging instrument suitable for conducting nano-computed-tomography (nano-CT) experiments. TXMs have been widely used at many synchrotrons for applications in a variety of fields, including energy, geology, biology, and material science. They have demonstrated spatial resolutions of less than 100 nm and respective fields of view of about 20-100 µm. In these instruments, tunable monochromatic x-rays illuminate the condenser, e.g. an ellipsoidal glass mono-capillary, and a Fresnel zone plate (FZP) is used as the objective lens to magnify the images or radiographs (Figure 1). Zernike phase contrast imaging for scanning low-absorbing samples can be obtained by adding a phase ring downstream of the FZP.

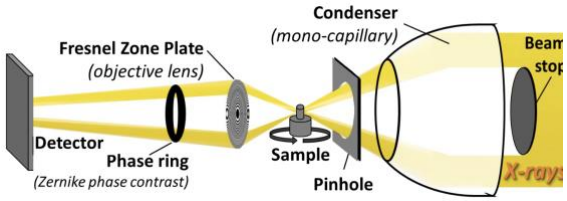

FIGURE 1. Scheme of a typical Transmission X-ray Microscope instrument.

In a nano-CT experiment, the sample is continuously rotated, and magnified projection data are recorded by a detector. Then these projections are structured and used for reconstructing a 3D structure of the sample. The highest resolution in 3D nano-imaging can be achieved only when the rotary stage and TXM optical elements are precisely aligned and have minimal vibration levels.

Here, we will discuss the main parts of the TXM at sector 32-ID of the Advanced Photon Source, demonstrate resolution tests, and explore a couple of applications that showcase high-resolution results.

TXM DESIGN AT SECTOR 32-ID OF APS

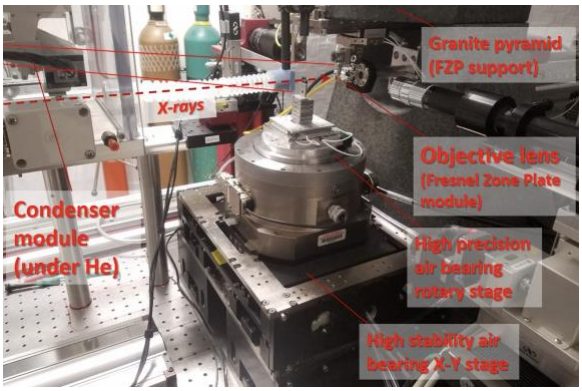

FIGURE 2. TXM at sector 32-ID of the Advanced Photon Source [1].

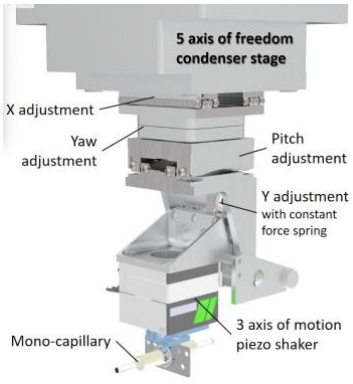

FIGURE 3. The mono-capillary condenser module allowing 5-axis motion.

The TXM at 32-ID demonstrating sub-10 nm resolution [1] has been developed during more than 10 years (Figure 2). The condenser module has 5-axis of motion implemented with SmarAct high-precision motors (Figure 3). The illumination

size at the sample location is controlled with a 3-axis piezo stage moving the condenser with a defined trajectory at high frequency. FZPs are carried on a 200 mm long stroke stick and slip piezo SmarAct stages enabling the positioning of lenses with low to very high NA. The whole FZP holder and stages are mounted on a granite block to minimize vibrations. To achieve the highest spatial resolution in 3D, a stiff sample stack was built in-house (Figure 4). The vertical sample positioning and the axis of rotation alignment with respect to the beam were ensured by a robust 2-axis granite air-bearing stage. When positions are achieved, the air is turned off and the stage behaved like a stiff monolithic block. The system has wobble of <0.1 µrad, radial error 33 nm @ 102 mm, and axial error 14 nm @ 102 mm. If no drift occurs, the stiff and high-precision air-bearing rotary stage from Professional Instruments Company simplifies the projection alignment step for tomographic reconstruction. The microscope is also surrounded by a sound-insulated enclosure with a closed loop system assuring temperature stability of ±0.1 °C.

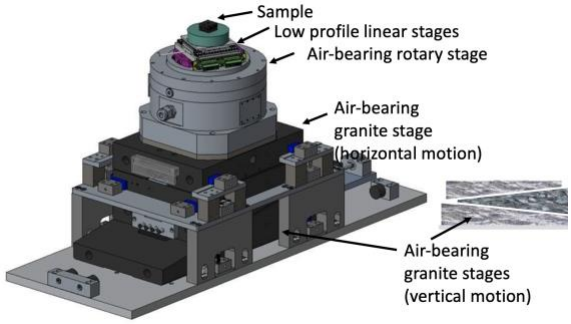

FIGURE 4. The air-bearing rotary stage mounted on the X-Y air-bearing granite stages for horizontal and vertical motion.

2D RESOLUTION TESTS

The optical performance of the TXM is first assessed using 2D X-ray absorption images of a Siemens star test pattern (Figure 5). Figure 5a illustrates the 2D radiograph of the Siemens star covering 12×10 µm^2 field of view for imaging.

The Siemens star comprises spokes that converge radially toward the center, and within the central region, the TXM and SEM control images (Figure 5b,c) effectively resolve separations between the spokes smaller than 20 nm. Although some spokes may appear fused together, the consistent visibility of these features in both the TXM and SEM images confirms their reality and rules out insufficient resolution as the cause.

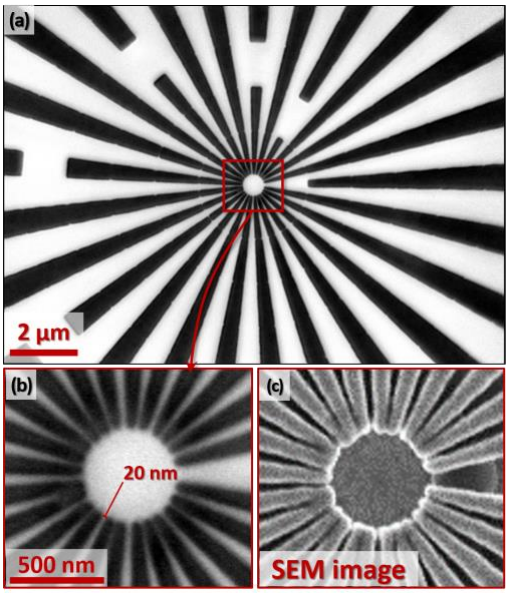

FIGURE 5. Resolution assessment of the TXM instrument by using a Siemens star test object: a) 2D radiograph of the whole object, b) zoomed-in region with the smallest features, c) SEM image of the region with the smallest features.

Then, we assessed the optical by analyzing 2D radiographs of a novel high aspect ratio FZP created through metal-assisted chemical etching (MACE) [3]. The FZP features platinum ALD metalized zones with a thickness of 16 nm (Figure 6). Besides functioning as nanofocusing optics (of the TXM in particular), these FZPs can also serve as test objects due to their precisely controlled wall thickness and known geometry.

The radiographs of the FZP, utilized as a test object, clearly depict the 16 nm thick platinum walls grown through atomic layer deposition (ALD), as illustrated in Figure 6 a,b and the intensity profile c. Subtle variations in the apparent wall thickness and absorption can be attributed to slight local warping of the walls in the third dimension, as later demonstrated in the 3D analysis of this optic. These direct observations provide conclusive evidence that the microscope's resolving power is at least 16 nm.

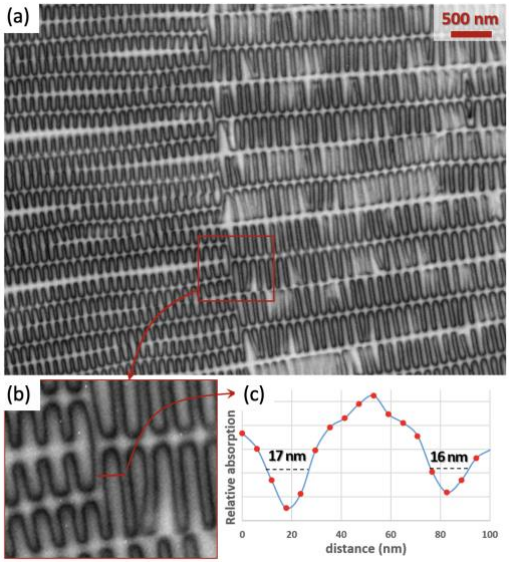

FIGURE 6. Resolution assessment of the TXM instrument by measuring a Fresnel zone plate as a test object: a) 2D radiograph of the outer zone of the FZP, b) zoomed-in region with small features, c) line profile through the smallest features.

To estimate the resolution limit, the Fourier ring correlation (FRC) method [4] is employed, analyzing pairs of radiographs of the FZP acquired with exposure times ranging from 1 to 30 seconds and utilizing a 5.2 nm pixel size. The FRC analysis, utilizing a half-bit criterion, reveals a remarkable spatial resolution of 9.4 nm, see Figure 7a. This finding aligns with the theoretical resolution range of 0.6 to 0.8 times the outer zone width of the FZP (16 nm) under partially coherent illumination [3]. The relationship between spatial resolution and exposure time is depicted in Figure 7b. For instance, a 1-second exposure only provides a spatial resolution of 17 nm, while 11 seconds are necessary to achieve 10 nm. The optimum resolution of 9.4 nm is attained after 20 seconds.

In contrast to 2D radiography, 3D tomographic imaging involves acquiring multiple projection images from different angles around the object. This necessitates sophisticated scanning setups, precise positioning, and careful coordination between the object and the imaging system to capture a comprehensive set of data for reconstruction. Therefore, achieving high-resolution results in tomography also requires the development of new reconstruction techniques that compensate for sample drifts and vibrations.

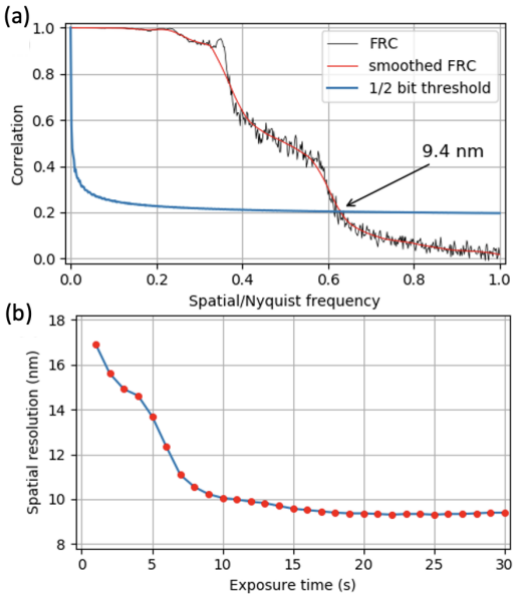

FIGURE 7. Resolution estimation with the FRC method for the Siemens star test object: a) FRC curves intersecting the 1/2-bit threshold and showing 9.4 nm resolution, b) dependence of the resolution on the exposure time.

3D DATA RECONSTRUCTION

To push the TXM resolution for reconstructing 3D objects even further we developed a new package TomoAlign that corrects for sample nano-drifts occurring during the scans [2]. With this approach, object x is recovered from projection data d by minimizing the following data fidelity term, $\min_{\{x,s\}} ||D_s Rx - d||_2^2$, where R is the tomographic projection operator, and D is the motion emulation operator that maps functions to new coordinates according to two-dimensional shifts s. Correct estimation of variable s leads to compensating sample drifts and/or deformation for each projection, that in turn results in higher resolution levels of the object reconstruction. The method works especially well for the interlaced angular scanning protocol, in which a full tomographic scan is acquired with multiple sample rotations where projection angles are mod 2π different and uniformly cover interval [0,2π]. With this protocol, a significant time gap between acquisition of two nearby angles, which gives similar data in a static case, allows for more accurate shifts' estimation. This method has demonstrated significant resolution improvement

for imaging mouse brain samples, integrated circuits, nano-lithography samples, etc.

APPLICATIONS

1. 3D Imaging of FZPs.

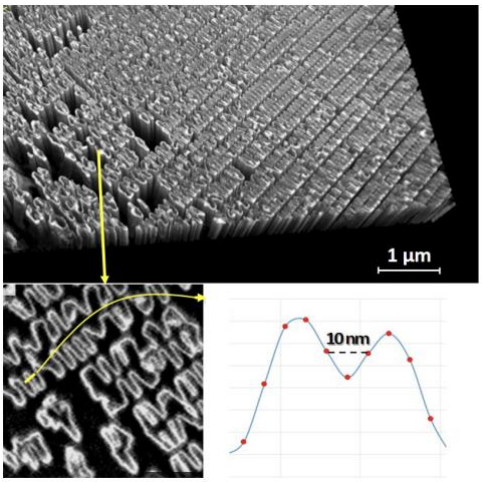

FIGURE 7. Using the TXM as a diagnostic tool to seek defects in FZPs.

To demonstrate resolution levels, the TXM instrument at sector 32-ID has been used with nano-lithography applications to seek for potential defects that can occur in the etching process for producing FZPs [3]. The nano-CT results unravel 3D structures that cannot be seen with SEM images without destroying the FZPs by cross-sectioning or cleaving process. The principal highlight of this high-resolution 3D characterization is the localized defect of the FZP walls generated from meandering etching paths. Figure 5 shows a reconstructed 3D image of an FZP with 10 nm distinguishable. Scanning of such an object took approximately 1 h, pixel size is 5 nm. For 3D object reconstruction, we used the iterative scheme compensating nano-drifts described in the previous section.

2. 3D imaging of integrated circuits.

As our second application, we demonstrate the usage of TXM for imaging integrated circuits. The utilized samples consist of multiple identical chips manufactured using 16 nm fin field-effect transistor technology, specifically designed for general-purpose logic. These chips feature transistors located on a single-crystal silicon substrate and interconnected electrically through over a dozen metal interconnect layers, which are embedded within SiO_2 dielectric material.

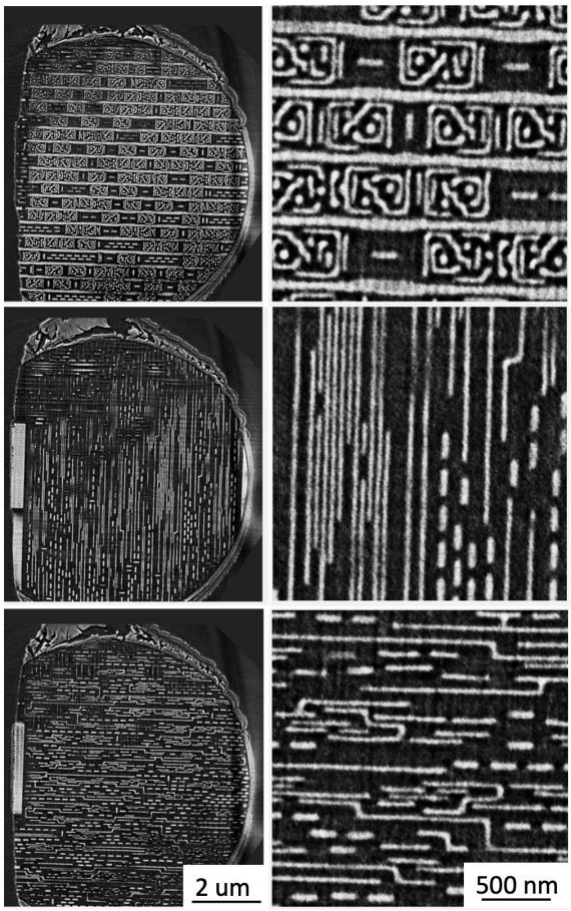

FIGURE 8. Reconstructed slices through a 3D integrated circuit measured with the TXM.

Figure 8 demonstrates examples of slices through the reconstructed integrated circuit volume. The total scan time of the integrated circuit was about 2 h, pixel size is 5 nm. For reconstruction, we used the iterative scheme with deformation compensation. No additional filters or regularization such as the Total Variation was used to remove noise and deblur images. One can see that most features (interconnections) are resolvable and after simple post-processing procedures can be segmented with regular thresholding. These TXM imaging results for integrated circuits are comparable to the ones achieved by the 3D ptychography technique and laminography geometry [5] which are theoretically more optimal for measuring these kinds of samples.

ACKNOWLEDGMENTS

This research used resources of the Advanced Photon Source, a U.S. Department of Energy (DOE) Office of Science user facility at Argonne

National Laboratory and is based on research supported by the U.S. DOE Office of Science-Basic Energy Sciences, under Contract No. DE-AC02-06CH11357.

REFERENCES

[1] De Andrade V, et al., Fast X-ray Nanotomography with Sub-10 nm Resolution as a Powerful Imaging Tool for Nanotechnology and Energy Storage Applications. Advanced Materials. 2021; 33.21: 2008653.

[2] Nikitin V, et al. Distributed optimization for nonrigid nano-tomography. IEEE Transactions on Computational Imaging. *2021;* 7: 272-287.

[3] Li, K., et al. Fabrication of hard x-ray zone plates with high aspect ratio using metal-assisted chemical etching. Journal of Vacuum Science & Technology B, Nanotechnology and Microelectronics: Materials, Processing, Measurement, and Phenomena. 2017; 35.6: 06G901.

[4] Marin V., et al. Fourier shell correlation threshold criteria, Journal of structural biology. 2005; 151.3: 250-262.

[5] Holler M, et al. Three-dimensional imaging of integrated circuits with macro-to-nanoscale zoom. Nature Electronics. *2019;* 2.10: 464-470.

MACHINE SPINDLE THERMAL ERROR MEASUREMENT USING A PHOTO MICROSENSOR ARRAY

Vinu J. Pannackal, Thomas Furness, Simon Fletcher and Andrew P. Longstaff
Centre for Precision Technologies
University of Huddersfield, Queensgate, Huddersfield
HD13DH, UK

INTRODUCTION

Precision machinery such as machine tools consist of robust structural components and systems for high quality manufacturing. However, the presence of external forces and thermal influences can lead to significant errors. With respect to thermal errors, according to *Bryan* [1] there are six major thermal error sources: temperature from the machine, effect of cutting process, effect of heating or cooling systems, influence of the environment, retaining thermal characteristics from prior environment and effect of operators. The thermal deformation of the machine tool spindle plays a crucial role in dictating the accuracy of precision components in a manufacturing process. The measurement of this deformation is important to quantify the magnitude of thermal error and ISO standards already exist to guide such evaluations [2].
Authors have defined different methods to measure and compensate the effect of thermal errors. *Liu et al*. [3] have used a commercial system called lion precision spindle analyzer to measure the radial thermal error. One drawback of this system is that sampling is permitted at a maximum rate of 0.5 Hz. Other research methods for assessing thermal drift include the API spindle analyzer [4], Renishaw's non-contact tool setup system [5] , and an array of capacitive sensors [6].

A typical disadvantage of all these systems is their high price, which makes them unaffordable for many small to medium enterprises. The systems can be easily damaged resulting in significant downtime for replacement parts. This gives a motivation to investigate a solution utilizing low-cost displacement sensors. *Potdar et al.* [7] proposed a novel displacement sensor design that makes use of widely available photomicrosensors and simple analogue circuitry to provide a high resolution measurement. Building upon this concept, this research examines the application of a slotted photomicrosensor (SPM) array to measure the thermal errors of a machine tool spindle.

SPM SENSOR DESIGN

The main advantage of the SPM sensor is that it is inexpensive and availability as an off-the-shelf solution. A typical SPM sensor (Omron EESX1096) costs roughly 4 GBP at the time of this research. An example is shown in Figure 1 with the internal electrical diagram of the sensor package.

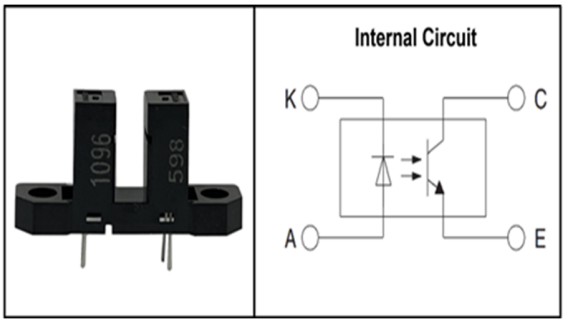

FIGURE 1. Omron Slotted photomicrosensor.

A photomicrosensor is a miniature photoelectronic sensor with an integrated amplifier that is typically used to detect passing objects or in positioning applications to trigger automation systems. The sensor package consists of a light emitting diode (K-A) and photo detector (C-E). When 100% of the light beams strike (fully open) the detector, the output will be ideally equal to the supply voltage. Similarly, when the light is completely cut off (fully closed), the output voltage will be zero. Moreover, when we shift the shutter from 100% to 0%, the output voltage varies with respect to the shutter position.

Figure 2 depicts the relationship between light current and slit width distance. The EESX1096 SPM sensors have horizontal slits to have increased sensitivity in the slot direction. The sensors used in this research are calibrated using a Renishaw XM60 laser interferometer as the

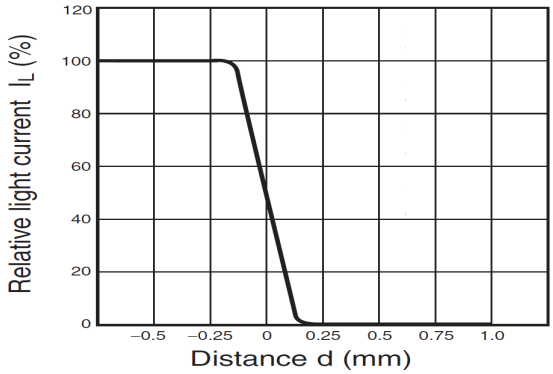

FIGURE 2. Sensing Position Characteristics.[8]

traceable reference, giving this sensor package 0.35µm repeatability and 0.11 V/µm sensitivity .

THERMAL ERROR TEST KIT

In this research, a novel thermal error measurement system was devised, employing two SPM sensors to quantify the error or deviation experienced along the Y-axis of a machine tool spindle (C-frame machine with no symmetry in the Y direction). The SPM array setup for the measurement is illustrated in Figure 3. The previous research [7] showed instability with these photomicrosensors but the use of differential measurement removed most common drift error therefore opposing the sensors enables the same difference to be used.

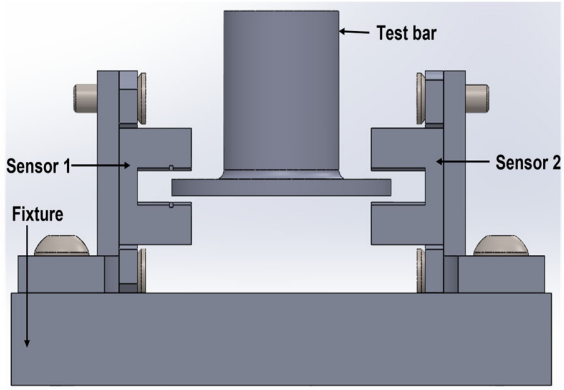

FIGURE 3. Slotted photomicrosensor array.

The setup consists of two sensor holders (and sensors), a solid base fixture and a test bar mounted in the spindle. The base and the sensor holders are 3D printed. The test bar is made of aluminum and has been precision turned for this application. For measurement, the test bar was positioned inside the slots of the photo microsensor. Data capturing and processing were accomplished using the NI DAQ (NI 9215) and LabVIEW software. Before proceeding to the thermal error measurement, it is necessary to evaluate the stability of the proposed solution for long term application associated with machine thermal testing.

SENSOR STABILITY

The long-term stability of the sensor plays a vital role in ensuring the accuracy and reliability of measurement results. However, it is important to note that variations in the displacement output of a sensor can occur even when these conditions remain reasonably stable. The individual sensor has sources of uncertainties from the internal electrical systems, the effects of ambient temperature, fluctuations in the power supply, electro-magnetic interferences, light interference. With differential measurement many of these errors should be reduced.

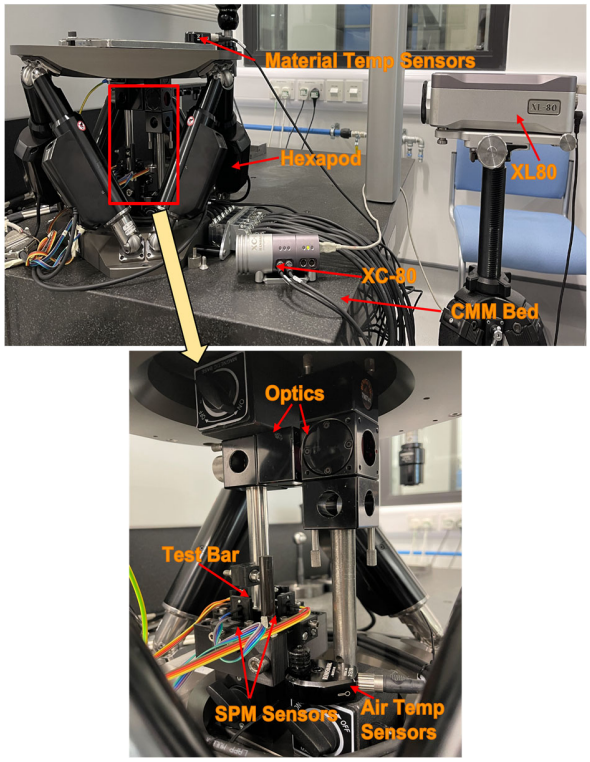

FIGURE 4. Stability test setup.

The test setup for the stability test is shown in Figure 4. Here, the stability of the individual sensors was measured over a period of 4 hours. The test was conducted in an environment-controlled room with a temperature of 20±1 °C. The CMM bed provided a rigid and thermally stable platform for the test. The test bar was carefully aligned within the SPM slit using Newport HXP200-MECA 6-Axis Hexapod. The

test results were validated using the Renishaw XL80 laser interferometer as a reference.

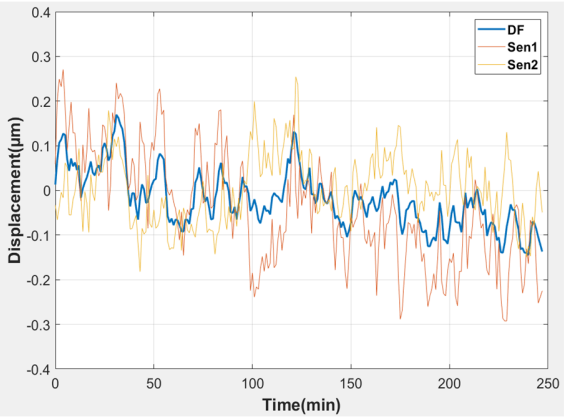

FIGURE 5. Sensor stability Sensor vs Differential.

Figure 5 illustrates the displacement data obtained from sensor 1 (S1) and sensor 2 (S3), along with their differential displacement (DF). It can be observed that, the effect of the electrical interference of each sensor has been reduced by the differential measurement. The standard deviation of the differential result exhibited a 36% reduction in comparison to the noise present in both sensors.

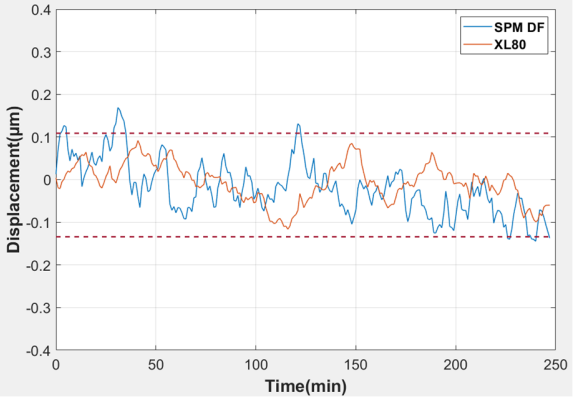

FIGURE 6. Sensor stability XL80 vs Differential.

The differential displacement of the SPM sensor stability is plotted against XL80 deviation in Figure 6. The variation in the environment temperature was under 0.4°C. The deviation between differential displacement of the SPM and XL80 remained within ±0.2 µm. During this time span, the SPM head output varies by 0.31 µm, whilst the XL-80 reading varies by 0.2 µm. The result indicates that in this stable temperature condition, the deviation between the differential output and the reference system is less than the individual uncertainties. It is acknowledged that industrial environments are often less stable so future work may be required to determine if local temperature measurement and calibration is required in highly variable environments.

EXPERIMENT SETUP

To verify the sensor function on a machine, the thermal error of a Hurco VMX30Ui CNC machine was measured. The system was mounted on the CNC bed as shown in Figure 7.

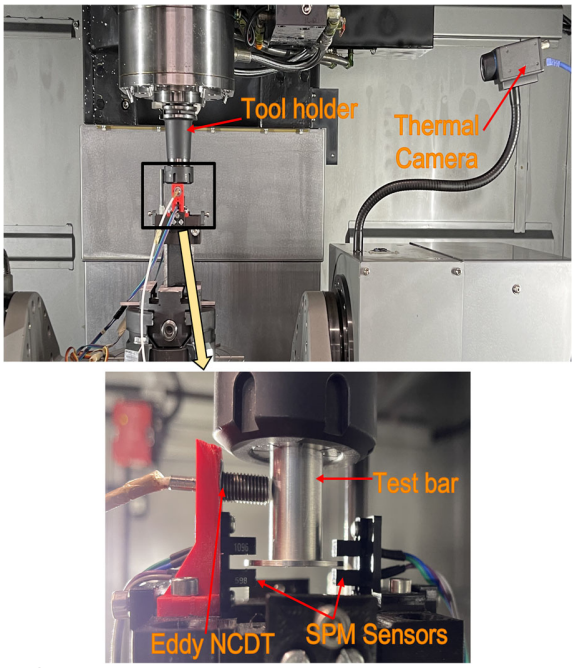

FIGURE 7. Thermal error measurement setup.

To validate the thermal error measured by the SPM sensor system, a Micro Epsilon non-contact eddy current transducer (NCDT) was employed as a reference. The CNC's standard warmup cycle was performed before starting the experiment to avoid damage to the spindle. The spindle was rotated at 12000 RPM for 45 minutes in a no-load condition followed by an idle condition for 1 hour. The test setup and measurement method can be traced back to BS ISO 230-3:2020 (Test Code For Machine Tools Determination Of Thermal Effects) [2]. The temperature of the spindle assembly was observed using a FLIR A35 Thermal Imaging Camera. The shiny surface of the spindle housing was covered using masking tape to ensure the surface had a known consistent high emissivity (0.95), and the camera was positioned perpendicularly to minimize direct reflections of light. The absolute accuracy of thermal imaging is still low ≈ ±2 °C but is only used here to be

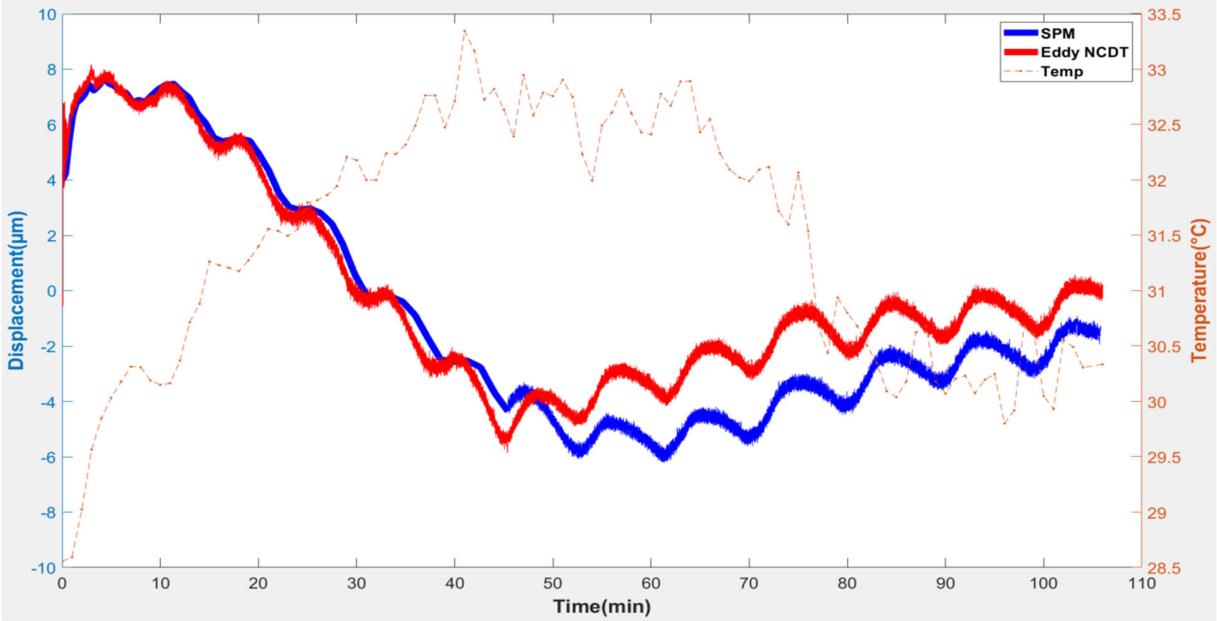

FIGURE 8.Thermal drift error profile in y axis.

indicative of significant change in spindle temperature.

MEASUREMENT RESULTS

The results shown in figure 8 represent the thermal error profile from the experiment. The temperature of the spindle housing was measured and shown with dotted line in the figure along with the differential output of SPM sensors (blue) and NCDT displacement (red).

The temperature rose 4.8 °C in 45 minutes while the spindle was held at 12000 RPM. During the heating cycle, the SPM sensor showed a runout error at the maximum spindle speed. However, this issue was successfully addressed by utilizing an envelope function. Figure 8 depicts the thermal error detected by the SPM sensor system and the NCDT system.

The radial thermal drift error along the y-axis exhibits a cyclic pattern in both sensor systems. This behavior can be attributed to the cooling effect of the chiller on the spindle rotor, causing temperature variations and subsequent drift. Future studies need to be carried out on CNC machines without the chiller switched off, so that thermal drift and spindle temperature can be observed on a greater scale. When the spindle came to rest, the thermal error movement is reversed towards the spindle's axis average line. For the heating cycle the thermal gradient of both SPM and NCDT sensors steeper than the gradient of the cooling cycle. The gradients were closer to each other, showing that the sensors values were in close agreement with an impressive 80% correlation, accompanied by a 2 µm deviation. It can be observed that the deviation between both sensor systems increases during the heating cycle while decreasing towards the end of the cooling cycle. The observed slight variations could be attributed to two potential factors: the positioning of both sensors (at the tip and stem of the test bar) and the variation in the expansion of the test bar. The positional variance between both systems may be influenced by the tilt error motion of the spindle. However, this discrepancy can be mitigated through the implementation of appropriate compensation techniques.

At 12000 RPM, the maximum radial thermal error measured by the SPM sensor kit and NCDT sensor was 12 µm and 10 µm, respectively. However, the overall trend of the temperature versus the spindle's radial thermal drift error indicates excellent possibilities for the SPM based thermal error measurement system.

FUTURE WORKS

Future research will involve extensive testing to identify and compensate the deviation from the reference system. Future measurements will need to be performed at higher sampling rate to obtain true differential results. Once the desired performance is achieved, the sensor system may

be used investigate the radial, axial and tilt error motions of the machine tool spindle.

CONCLUSION

This paper describes a new spindle thermal error measurement device that employs an array of low cost slotted photomicrosensors in conjuction with a spindle mounted test bar. An initial stability test indicated a stable output for SPM sensor array in comparison to laser interferometer with a ±0.2 µm deviation. The thermal error measured by the traditional NCDT Eddy current sensor and SPM sensor were comparable, and the measured value had a 2 µm deviation. But considering the cost perspective of both sensors, the new SPM sensor array proposed in this research seems highly promising. The future work will emphasise reducing the effect of this deviation.

ACKNOWLEDGEMENTS

The authors gratefully acknowledge the UK's Engineering and Physical Sciences Research Council (EPSRC) funding of the Future Metrology Hub (Grant Ref: EP/P006930/1) and UKRI-funded Advanced Machinery and Productivity Initiative (84646).

REFERENCES

[1] J. Bryan, "International Status of Thermal Error Research (1990)," *CIRP Annals,* vol. 39, no. 2, pp. 645-656, 1990/01/01/ 1990, doi: https://doi.org/10.1016/S0007-8506(07)63001-7.

[2] "BS ISO 230-3:2020: Test code for machine tools: Determination of thermal effects," ed: British Standards Institute, 2020.

[3] K. Liu, M. Sun, T. Zhu, Y. Wu, and Y. Liu, "Modeling and compensation for spindle's radial thermal drift error on a vertical machining center," *International Journal of Machine Tools and Manufacture,* vol. 105, pp. 58-67, 2016/06/01/ 2016, doi: https://doi.org/10.1016/j.ijmachtools.2016.03.006.

[4] Y. Zhao, Y. Xu, L. Tao, and Y. Zhao, "Experiment and Analysis of Thermal Error of Boring-Milling Center Spindle," *IOP Conference Series: Earth and Environmental Science,* vol. 514, p. 042018, 07/03 2020, doi: 10.1088/1755-1315/514/4/042018.

[5] Y. Li, W. Zhao, W. Wu, B. Lu, and Y. Chen, "Thermal error modeling of the spindle based on multiple variables for the precision machine tool," *The International Journal of Advanced Manufacturing Technology,* vol. 72, no. 9, pp. 1415-1427, 2014/06/01 2014, doi: 10.1007/s00170-014-5744-4.

[6] F. Tan, M. Yin, L. Wang, and G. Yin, "Spindle thermal error robust modeling using LASSO and LS-SVM," *The International Journal of Advanced Manufacturing Technology,* vol. 94, no. 5, pp. 2861-2874, 2018/02/01 2018, doi: 10.1007/s00170-017-1096-1.

[7] A. A. Potdar, S. Fletcher, and A. P. Longstaff, "Performance characterisation of a new photo-microsensor based sensing head for displacement measurement," (in English), *Sensors and actuators.A.Physical.,* vol. 238, pp. 60-70, 2016, doi: 10.1016/j.sna.2015.12.007.

[8] *Micro Sensing Device Data Book "Photomicrosensor (Transmissive) EE-SX1096-W11 Datasheet"*, Omron, 2015, pp. 146-147. [Online]. Available: https://omronfs.omron.com/en_US/ecb/products/pdf/en-scec-001d-1.pdf.

Author Index

Badrawy, Sinan J. 16
Bean, Sunil 95
Browning, Nicholas A. 8
Chao, Leon 39
Comden, Zane 39
De Andrade, Vincent 90, 95
DeCarlo, Francesco 90, 95
Deriy, Alex 95
Devitt, Andrew D. 51, 77
Donmez, Alkan 23
Draganov, John 39
Dupont, Ralf 24
Erturk, Murat 78
Evans, Christopher J. 43
Fang, Chenggang 52
Fezza, Kamel 90, 95
Fletcher, Simon 100
Furness, Thomas 100
Furst, Stephen J. 67
Guertin, Christian F. 32
Hayes, Stephen T. 72
Heyman, Ian 84
Hopper, Laura E. 43
Huo, Dehong 52
Ishii, Nobuyuki 34
Kondo, Ryoji 63
Koyama, Hayato 63
Lloyd, Cyrus M. 8
Longstaff, Andrew P. 100
Luttrell, Dan E. 58
Matus, Janusz 90
Micklow, Lauren 67
Miller, Jimmie A. 43
Mittone, Alberto 95
Newell, David 39
Nikitin, Viktor V. 95
Noste, Todd 3, 43
Pannackal, Vinu J. 100
Preissner, Curt A. 90
Rainey, Jeremy W. 51, 77
Roblee, Jeffrey W. 1
Schlamminger, Stephan 39
Seifert, Frank 39
Shu, Deming 90
Stocker, Mark A. 49
Tanaka, Shotaro 63
Wojcik, Michael 95
Zhou, Lei 84

Volume 80

ISBN 978-1-887706-58-2